

A 1.48–2.48 μm $R=28\,000$ spectroscopic atlas of the L7.5 and T0.5 components of the nearest pair of brown dwarfs: Luhman 16AB

Hiroiyuki Tako Ishikawa^{1*} , Stanimir Metchev^{1,2†} , Megan E. Tannock^{1,3} , Gregory N. Mace⁴ ,
Callie E. Hood⁵ , Jonathan J. Fortney⁵ , Sagnick Mukherjee⁵ , Paulo Miles-Páez⁶ ,
Radostin Kurtev⁷ 

¹Department of Physics and Astronomy, The University of Western Ontario, 1151 Richmond St, London, Ontario, N6A 3K7, Canada

²Institute for Earth and Space Exploration, The University of Western Ontario, 1151 Richmond St, London, Ontario, N6A 3K7, Canada

³Cosmographic Software, New Haven, CT 06513, USA

⁴Department of Astronomy, The University of Texas at Austin, 2515 Speedway, Austin, TX 78712, USA

⁵Department of Astronomy & Astrophysics, University of California, Santa Cruz, CA 95064, USA

⁶Centro de Astrobiología, CSIC-INTA, Camino Bajo del Castillo s/n, 28692 Villanueva de la Cañada, Madrid, Spain

⁷Departamento de Física y Astronomía, Facultad de Ciencias, Universidad de Valparaíso, Av. Gran Bretaña 1111, Casilla 5030, Valparaíso, Chile

Accepted XXX. Received YYY; in original form ZZZ

ABSTRACT

We present a high signal-to-noise (SNR ~ 450), high-dispersion ($R \equiv \lambda/\Delta\lambda \sim 28\,000$) H - and K -band spectroscopic atlas of the L7.5 and T0.5 components of the Luhman 16AB binary (WISE J104915.57–531906.1AB): the closest pair of brown dwarfs, and one of the best substellar benchmarks. The spectra were combined from a 70-day spectroscopic monitoring campaign of the binary with IGRINS on Gemini South. We fit model photospheres to the combined high-quality spectra to estimate atmospheric parameters. The model is based on the Sonora model atmosphere further incorporating the effects of clouds and disequilibrium. We detect ammonia (NH_3) lines in both binary components, making Luhman 16A the warmest object where individual NH_3 lines were identified. We discover hydrogen (H_2), hydrogen sulfide (H_2S), and hydrogen fluoride (HF) lines in both components, following recent reports of these species in either cooler (H_2 , H_2S in a T6 dwarf) or warmer (HF in young late-M or mid-L dwarfs) objects. Methane (CH_4) shows a small contribution, with lines sensitive to the slight temperature difference spanning the L/T transition. Against model expectations, we do not detect FeH lines, implying more efficient iron rainout than incorporated in the models. We find various unidentified features in water-dominated regions, likely the result of residual inaccuracies in the water line lists. We searched for planetary-mass companions by periodogram analysis of radial velocities over 70 days but detected no significant signal. The upper limits of projected planetary mass are $M \sin i = 0.2 M_{\text{J}}$ and $0.3 M_{\text{J}}$ at $P \sim 1$ day, and $0.4 M_{\text{J}}$ and $0.7 M_{\text{J}}$ at $P \sim 10$ days for Luhman 16A and B, respectively.

Key words: (stars:) brown dwarfs – (stars:) binaries: visual – infrared: stars – techniques: spectroscopic – stars: atmospheres – line: identification

1 INTRODUCTION

Reliable atmospheric characterisation of substellar objects depends on the accuracy of the spectral modelling and thus, on the correct understanding of spectral lines. Recent updates in molecular line lists have offered significant improvements in accuracy, particularly for water and methane in the near-infrared spectra (e.g., Tennyson et al. 2020; Gharib-Nezhad et al. 2021; Gordon et al. 2022; Hood et al. 2023). The near-infrared is well suited to spectroscopic characterisation at high dispersion because it spans the emission peak of brown dwarfs. However, there are still only a handful of high-SNR high-dispersion spectroscopic studies with broad wavelength near-infrared coverage of brown dwarfs. Tannock et al. (2022) performed a detailed

analysis of $R \sim 28\,000$ H - and K -band spectra of a T6 brown dwarf, 2MASS J08173001–6155158, assessing the accuracy of the latest line lists of H_2O , CH_4 , and NH_3 . They also reported the first detection of H_2 and H_2S molecular lines in an atmosphere outside the Solar System. We extend the identification and assessment of these spectral lines to warmer objects near the L/T transition by presenting a comparable high-dispersion analysis on the nearest brown dwarf binary system, Luhman 16AB (Luhman 2013; also known as WISE J104915.57–531906.1AB or WISE 1049–5319).

At a distance of only 1.9960 ± 0.0002 pc (Bedin et al. 2024), Luhman 16 is the third nearest stellar or substellar system, after α Cen and Barnard’s star, and the nearest star or brown dwarf to be discovered in almost a century. Luhman 16AB consists of an L7.5 and a T0.5 dwarf (Burgasser et al. 2013b) and has been extensively studied since its discovery, with measurements of the photometric amplitudes and periods of the two components (Gillon et al. 2013; Burgasser

* E-mail: hishikaw@uwo.ca

† E-mail: smetchev@uwo.ca

et al. 2013a; Biller et al. 2013; Apai et al. 2021; Fuda et al. 2024), Doppler imaging to map their surface inhomogeneities (Crossfield et al. 2014; Chen et al. 2024), spectroscopic monitoring of the cloud distributions on both objects (Buenzli et al. 2015; Karalidi et al. 2016; Kellogg et al. 2017; Heinze et al. 2021), and Bayesian inference of the temperature and C/O ratio of the primary (Kawahara et al. 2022). The proximity of the binary has also enabled precise astrometric monitoring of the system, resulting in the accurate determination of the binary orbit and the individual component masses. Bedin et al. (2024) constrained an orbital period of 26.55 ± 0.08 years and masses of 35.4 ± 0.2 Jupiter masses (M_J) and $29.4 \pm 0.2 M_J$ for components A and B, respectively.

Its proximity and apparent brightness enable high-SNR high-dispersion spectroscopy despite the intrinsic faintness of this type of objects. With two coeval components that span the L/T transition, the Luhman 16AB binary can also elucidate the role of CO/CH₄ disequilibrium chemistry that characterizes this transition. In addition, the wealth of astrometric monitoring and dynamic mass estimates help narrow down the search for additional components in the system.

The potential presence of planets in this neighbouring system is also of interest because the low masses of the binary components could reveal some of the lowest-mass planets through direct imaging, astrometry, or radial velocity monitoring. Melso et al. (2015) and Bedin et al. (2017, 2024) excluded the presence of widely separated massive planets ($\geq 26 M_\oplus$ with orbital periods of 400–5000 days or $\geq 50 M_\oplus$ with 2–5000-day periods) through direct imaging and astrometry, respectively. Such planets are not necessarily expected given the 3.52 ± 0.006 au binary semi-major axis (Bedin et al. 2024) and the substellar masses of the components. Low-mass stars tend to have lower-mass planets on narrower orbits (e.g., Batalha 2014, and references therein), and brown dwarf hosts could be expected to follow that trend.

Transits or radial velocity monitoring are more sensitive to close-in planets. The long-duration TESS monitoring of Luhman 16AB by Apai et al. (2021); Fuda et al. (2024) does not reveal any transit signatures. While this excludes transiting orbital geometries, close-in planets on inclined orbits have yet to be surveyed with radial velocities around either binary component. Being spatially resolved at about $1''$ and having components of similarly high apparent brightness ($K_{s,A} = 9.6$ mag and $K_{s,B} = 9.8$ mag; Kniazev et al. 2013), the Luhman 16AB binary potentially offers an opportunity for precise radial velocity (RV) monitoring even without a stabilized RV spectrograph: by using one binary component as an RV reference for the other. We used our Immersion GRating Infrared Spectrometer (IGRINS; Yuk et al. 2010; Park et al. 2014; Mace et al. 2016, 2018) series of observations with Gemini South to search for close-in giant planets.

2 OBSERVATIONS AND DATA REDUCTION

We observed the Luhman 16AB system with IGRINS on Gemini South under Gemini program ID GS-2018A-Q-114 (PI: S. Metchev). IGRINS is a cross-dispersed spectrograph that simultaneously covers the *H* and *K* bands from 1.45 to 2.48 μm with a spectral resolution of $R \sim 28\,000$.

2.1 Observation

We observed the two components of the binary system simultaneously, with both objects on the IGRINS spectrograph slit. Observa-

tions took place on 33 nights over a 70-night span between 21 April 2018 and 29 June 2018, and are summarized in Table A1.

Each observation was composed of an AB dither pair with exposure times of 300s. One or two sets of AB pairs were obtained on each night. Low-quality data due to poor seeing and bad weather was excluded, and we used 93 exposures for our final analysis. All 93 spectra were combined into a single spectrum for atlas creation, parameter estimation (Section 3, and atmospheric analysis (Section 4). However, the spectrum at each epoch was treated as a separate data point for the periodic analysis of RVs (Section 5).

We tabulate the correspondence between the diffraction order (m) and the wavelength range in Table 1.

2.2 Data Reduction

2.2.1 Spectroscopic Extraction and Telluric Correction

Since the Luhman 16AB system was observed with both objects on the slit, a custom reduction in addition to the standard procedures with IGRINS Pipeline Package (PLP; Lee et al. 2017) was required.

The data were first reduced using the PLP. The PLP performed bad pixel correction, pattern noise removal, and sky background subtraction. Each order was rectified onto a rectangular grid and the wavelength solution was derived from sky OH emission and telluric absorption features. Post-processing the two-dimensional IGRINS PLP output was required to separate the simultaneously observed components of Luhman 16. The custom post-processing IDL software first reduced the background by subtracting the median from each column (spatial direction) of the two-dimensional spectrum. Each spectral order was then extracted and collapsed along the spectral direction so the median spatial profile was determined. The A and B spectra were optimally extracted by fitting each column's peak flux to the normalized spatial profile and then taking the sum under the profile. We masked some parts of spectra that were affected by two-dimensional patterns of bad pixels too large to be corrected in the reduction process.

The same extraction was performed on the A0V standard star observed for the telluric correction (Vacca et al. 2003). Uncertainties for each order were derived from the same extraction of two-dimensional variance spectra from the PLP. The telluric standard spectra were divided by a Vega model to pre-reduce the effect of A0V intrinsic features. The target spectrum and the Vega-corrected telluric standard were then cross-correlated to align the telluric features in the target frame. The target spectrum was divided by the telluric standard and the barycentric velocity correction was applied to the wavelength solution. The telluric-corrected output files were one-dimensional spectra of the flux, variance, and signal-to-noise for both the A and B components for each observation.

Some strong telluric features still left residuals, which may impact the model-fitting analyses. To identify and mask the regions with prominent telluric features, we simulated transmission spectra for the Earth's atmosphere using the Planetary Spectrum Generator (PSG; Villanueva et al. 2018) for the longitude, latitude, and altitude of the Gemini South Observatory. We masked regions where telluric absorption reduces atmospheric transmission to $<35\%$ and regions with OH emission lines (Rousselot et al. 2000). We slightly increased the transmission threshold to 40% for the four orders ($m = 86\text{--}89$) where strong CO₂ telluric lines also left non-negligible residuals. The PSG spectra and the transmission thresholds are displayed in the spectral atlas of Appendix B.

We obtain a final high signal-to-noise (SNR) spectrum for each component in each order by combining all spectra of individual ex-

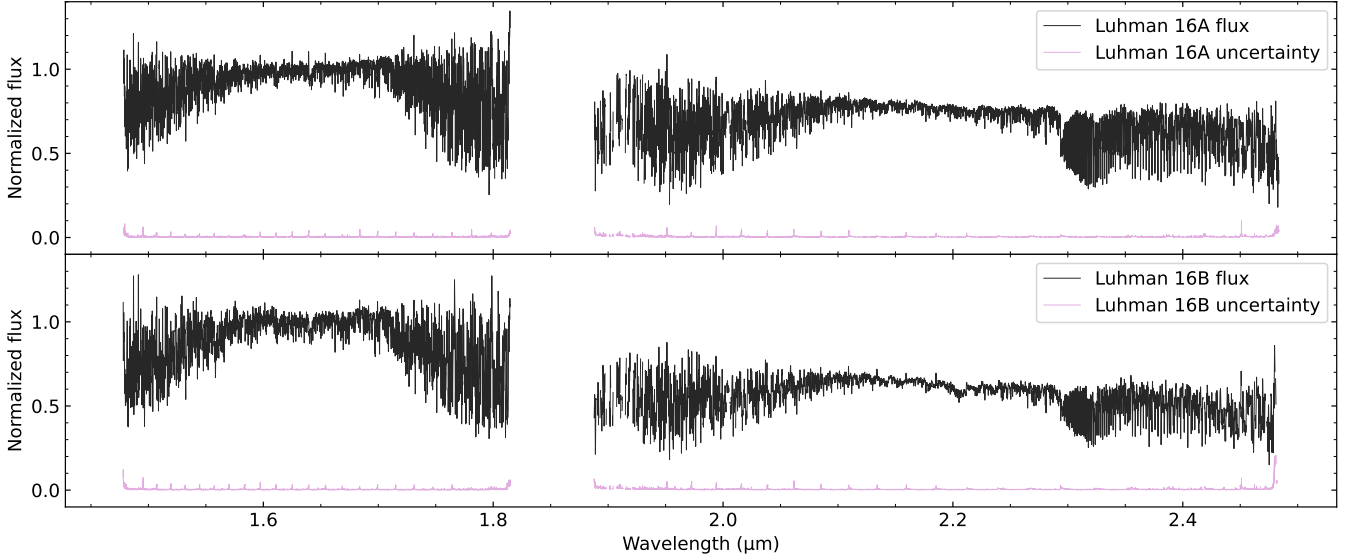


Figure 1. The full *H*- and *K*-band IGRINS spectra of Luhman 16A (upper panel) and Luhman 16B (lower panel) with all 93 epochs combined, and all 46 orders stitched together. The relative fluxes between orders are calibrated based on medium-dispersion spectra from Kellogg et al. (2017). The entire spectra are normalized by the pseudo-continuum over 1.6–1.7 μm at the *H*-band peak for each object. These data look noisy but actually have $\text{SNR} \approx 600$ at the peak of the *H*-band spectra with average SNRs of ~ 250 over both bands for both objects. Most of the conspicuous downward spikes are real absorption features. They can be seen in detail in the order-by-order spectral atlas in Appendix B.

Table 1. The wavelengths of the IGRINS diffraction orders (from Stahl et al. 2021) and the known molecular absorbers in each order.

Band	Order <i>m</i>	Wavelength Coverage (μm)	Molecular Line Absorbers	Band	Order <i>m</i>	Wavelength Coverage (μm)	Molecular Line Absorbers
<i>H</i>	121	1.482–1.494	H ₂ O	<i>K</i>	94	1.894–1.910	H ₂ O, H ₂ S
<i>H</i>	120	1.493–1.506	H ₂ O	<i>K</i>	93	1.909–1.930	H ₂ O
<i>H</i>	119	1.504–1.519	H ₂ O	<i>K</i>	92	1.929–1.950	H ₂ O
<i>H</i>	118	1.517–1.531	H ₂ O	<i>K</i>	91	1.949–1.972	H ₂ O
<i>H</i>	117	1.529–1.543	H ₂ O	<i>K</i>	90	1.971–1.993	H ₂ O, H ₂ S
<i>H</i>	116	1.541–1.556	H ₂ O	<i>K</i>	89	1.992–2.015	H ₂ O, H ₂ S, NH ₃
<i>H</i>	115	1.554–1.569	H ₂ O, CO	<i>K</i>	88	2.014–2.038	H ₂ O, NH ₃
<i>H</i>	114	1.567–1.583	H ₂ O, FeH, CO, H ₂ S	<i>K</i>	87	2.037–2.061	H ₂ O
<i>H</i>	113	1.581–1.596	H ₂ O, FeH, CO, H ₂ S	<i>K</i>	86	2.060–2.085	H ₂ O
<i>H</i>	112	1.594–1.610	H ₂ O, FeH, CO, H ₂ S	<i>K</i>	85	2.084–2.109	H ₂ O
<i>H</i>	111	1.608–1.624	H ₂ O, FeH, CO, H ₂ S	<i>K</i>	84	2.108–2.134	H ₂ O, H ₂
<i>H</i>	110	1.622–1.639	H ₂ O, FeH, CO, H ₂ S, CH ₄	<i>K</i>	83	2.133–2.159	H ₂ O
<i>H</i>	109	1.637–1.653	H ₂ O, FeH, H ₂ S, CH ₄	<i>K</i>	82	2.158–2.185	H ₂ O, NH ₃
<i>H</i>	108	1.651–1.668	H ₂ O, FeH, CH ₄	<i>K</i>	81	2.184–2.212	H ₂ O, NH ₃ , CH ₄
<i>H</i>	107	1.666–1.683	H ₂ O, FeH, CH ₄	<i>K</i>	80	2.211–2.239	H ₂ O, NH ₃ , CH ₄ , H ₂
<i>H</i>	106	1.681–1.699	H ₂ O, FeH, CH ₄	<i>K</i>	79	2.238–2.267	H ₂ O, NH ₃ , CH ₄
<i>H</i>	105	1.697–1.715	H ₂ O, FeH	<i>K</i>	78	2.266–2.295	H ₂ O, CO, NH ₃ , CH ₄
<i>H</i>	104	1.713–1.730	H ₂ O, FeH	<i>K</i>	77	2.294–2.326	CO, H ₂ O
<i>H</i>	103	1.728–1.747	H ₂ O	<i>K</i>	76	2.325–2.355	CO, H ₂ O, NH ₃ , CH ₄
<i>H</i>	102	1.745–1.764	H ₂ O	<i>K</i>	75	2.354–2.383	CO, H ₂ O, NH ₃ , CH ₄
<i>H</i>	101	1.762–1.781	H ₂ O	<i>K</i>	74	2.389–2.414	CO, H ₂ O, CH ₄ , H ₂
<i>H</i>	100	1.779–1.798	H ₂ O	<i>K</i>	73	2.420–2.445	H ₂ O, CO, CH ₄
<i>H</i>	99	1.797–1.812	H ₂ O	<i>K</i>	72	2.452–2.478	H ₂ O, CO, H ₂ S

posures via a weighted average. By combining data from different epochs, the wavelength range lost in the telluric masking is partly recovered because the relative velocity shifts of the target and telluric spectra vary at different epochs. For each wavelength point, we calculate the weighted standard errors from 93 spectra from different epochs to estimate the uncertainty of the combined spectrum. This includes not only the statistical uncertainty based on the derivation in

the reduction phase but also systematic errors potentially raised from telluric residuals or changes in instrumental or observing conditions.

The combined spectra have SNRs with an average of ~ 250 and a maximum of ~ 600 . We show in Figure 1 the order-stitched spectra over the entire wavelength coverage of IGRINS. For the order stitching, we calibrated the distortions in continuum levels, mainly induced by discrepancies between different orders, so that our pseudo-continuum is in line with that of the Magellan/FIRE medium-

dispersion spectra of Luhman 16AB in Kellogg et al. (2017). We used each order separately for the subsequent analysis. Each order of the spectral atlas is shown in Appendix B.

2.2.2 Validation of the Telluric Standard Correction

Two of the six telluric standard stars used in the reduction, HIP 52407 and HIP 53836, displayed non-negligible residuals at the Br γ line (2.1661 μm), leaving spurious emission features in the target spectra in order $m = 82$. To correct this, we substituted the 2.16544–2.16707 μm wavelength range in the combined spectra with the weighted average of only the spectra unaffected by the Br γ residuals. We also found a two-dimensional ghost on every image causing a false emission line at 2.16067 μm , near the Br γ line, in all Luhman 16B spectra. We masked a 2.5 \AA -wide region around this peak. The final spectrum in Figure 1 has been thus corrected.

We further inspected all other orders in which we could anticipate similar contamination from weaker hydrogen lines in telluric standard spectra. Several H line positions are covered in our spectral range as shown in Figure 2. The Paschen series (principal quantum number $n' = 3$ for the lower energy level) does not affect our spectra. Paschen- α falls into the gap between the two bands, and the other lines are shorter than the wavelength range of IGRINS. The Brackett series ($n' = 4$) pervades the H and K bands, with transitions from upper energy levels with $n \geq 7$. Only the Br γ ($n = 7$, 2.1661 μm) showed significant residuals in some of our spectra: corrected as outlined above. The Br δ transition ($n = 8$, 1.9451 μm) may also show a small upward residual (see panels for order $m = 92$ in Figures B1 and B2), but that is less evident in the context of the surrounding noise. The spectrum in the corresponding order ($m = 92$) is fragmented due to a large number of telluric-line masking and several points show large residuals; the upward residuals at 1.9451 μm appear to be the largest among them (Table 4). The Pfund series ($n' = 5$) lines are mostly redder than our wavelength range, and no residuals were detected even at the expected 2.2794 μm Pfund break where bound-free absorption begins. Hence, we found no further need to correct the telluric calibration of the Luhman 16AB spectra.

2.2.3 Degraded spectral resolution

The IGRINS team reports¹ that the spectral resolution of IGRINS was degraded between April 2018 and May 2019 due to a defocus of the echellogram. We found that this affected our data not only in the K band mentioned in their report but also in the H band with a resolution lower than the configured value of $\sim 40\,000$. The spectral resolution is characterised by the instrument broadening kernel, which depends on the position on the detector, i.e., wavelength. We assume this instrumental profile (IP) to be Gaussian. We estimated its full width of half maximum (FWHM) at each wavelength using clean telluric lines recorded in the spectra of the A0V telluric standard stars. We fit two relations for the FWHM of the Gaussian (in μm), in the H and K bands respectively:

$$\text{FWHM}_H(\lambda) = 9.80 \times 10^{-5} \lambda - 9.82 \times 10^{-5} \quad (1)$$

$$\text{FWHM}_K(\lambda) = 10.01 \times 10^{-5} \lambda - 13.82 \times 10^{-5} \quad (2)$$

where λ is a wavelength in μm . Figure 3 shows the resolving power R

¹ <https://sites.google.com/site/igrinsatgemini/2018-k-band-resolution>

($\lambda/\Delta\lambda$) as a function of wavelength, adopting these FWHMs as $\Delta\lambda$. The average R ranges from about 20 000 to 35 000, with an average of $\sim 28\,000$.

3 PHOTOSPHERIC ANALYSIS

3.1 Fitting of Photospheric Models

We compared the combined spectra of each component to theoretical spectral models, following the order-by-order fitting methodology of Tannock et al. (2021, 2022) (hereafter Tann22) using the MASTIFF model fitting tool² to simultaneously determine the photospheric parameters, the projected rotational velocity $v \sin i$ and the RV.

We used an iteration of the Bobcat Alternative A model adopted in Tann22, which is based on the Sonora Bobcat model (Marley et al. 2021) with more up-to-date molecular line lists. The molecules for which Tann22 updated line lists are H₂O (Polyansky et al. 2018), CH₄ (Hargreaves et al. 2020), and NH₃ (Coles et al. 2019). Sonora Bobcat calculates emergent spectra from 1D cloudless radiative-convective equilibrium model atmospheres. While a cloudless model was appropriate for the T6 dwarf analysed in Tann22, the two L/T-transition components of Luhman 16 require both condensate clouds and disequilibrium chemistry.³ We added both effects self-consistently using the PICASO 1D radiative-convective equilibrium climate model (Mukherjee et al. 2023; Batalha et al. 2019). The condensate clouds were computed using the VIRGA cloud model (Rooney et al. 2022) with a uniform sedimentation efficiency parameter f_{sed} within our self-consistent modelling framework. The vertical eddy diffusion was parameterised with the K_{zz} coefficient in these models. The K_{zz} parameter relates the local scale height, the turbulent mixing length, and the convective heat flux of the atmosphere. In convective layers of the atmosphere, it is parameterised via Equation (2) in Mukherjee et al. (2022). In radiative atmospheres, the turbulent mixing length was decreased following Equation (6) in Ackerman & Marley (2001). To account for the inherent uncertainty of K_{zz} , we employed two other cases where the nominal K_{zz} profiles were uniformly multiplied by factors of 0.1 and 100 across all atmospheric layers. We refer to this multiplication factor as $C_{K_{zz}}$ hereafter. After the initial scaling, the K_{zz} profiles were iteratively re-calculated to preserve the effective temperature of the photosphere, following Mukherjee et al. (2023). Disequilibrium chemistry was treated using the quench time approximation, also as in Mukherjee et al. (2023). We hereafter call the new self-consistent grid of models ‘‘Bobcat Alternative B.’’

The spectra from the Bobcat Alternative B model grid were generated with the DISORT radiative transfer tool (Stamnes et al. 2017). The grid of parameters included effective temperature ($1200 \leq T_{\text{eff}}/\text{K} \leq 1600$, step size of 100 K), surface gravity ($4.5 \leq \log g \leq 5.5$, step size of 0.5), sedimentation efficiency ($3 \leq f_{\text{sed}} \leq 5$, step size of 1), and eddy diffusion coefficient multiplication factor $C_{K_{zz}}$. The $C_{K_{zz}}$ multiplication factor is a scaling (0.1, 1.0, or 100) of the nominal eddy diffusion coefficient K_{zz} to account for the uncertainty of K_{zz} . We further extended the dimensionality of the photosphere grid by including rotational broadening (following Gray 1992) and

² https://github.com/megantannock/Mastiff_ModelFittingTools

³ The Sonora model series is undergoing continuous development. Disequilibrium chemistry has been introduced by Karalidi et al. (2021, Sonora Cholla) and Mukherjee et al. (2024, Sonora Elf Owl) and clouds by Morley et al. (2024, Sonora Diamondback). However, a comprehensive model combining both effects has yet to be released.

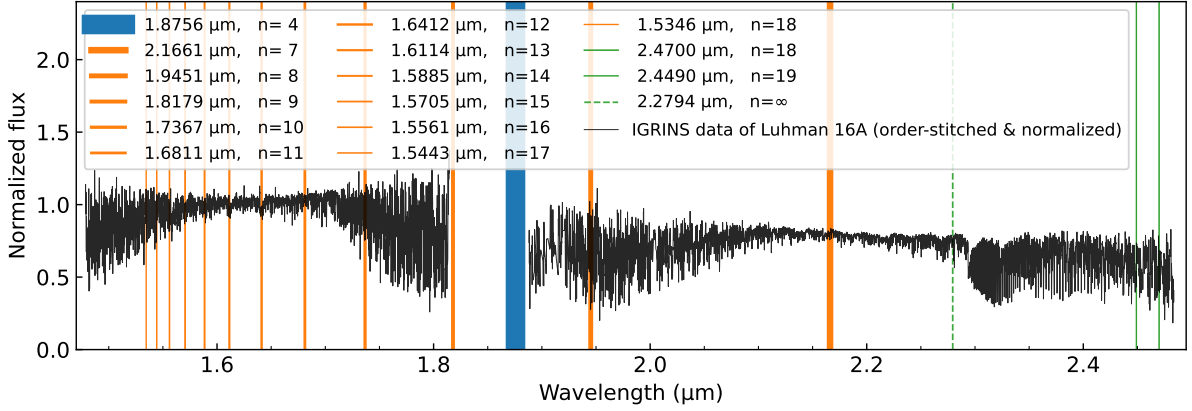


Figure 2. The positions of hydrogen atomic lines are indicated by the vertical lines overlotted on the spectrum of Luhman 16A (black spectrum). The blue line is Paschen- α , the orange lines are the Bracket series, and the green lines are the Pfund series. The n in the legend is the quantum number of the upper energy level. After removing residuals centred on the 2.1661 μm Bry line associated with two of the telluric standards, no further correction of the telluric calibration was required.

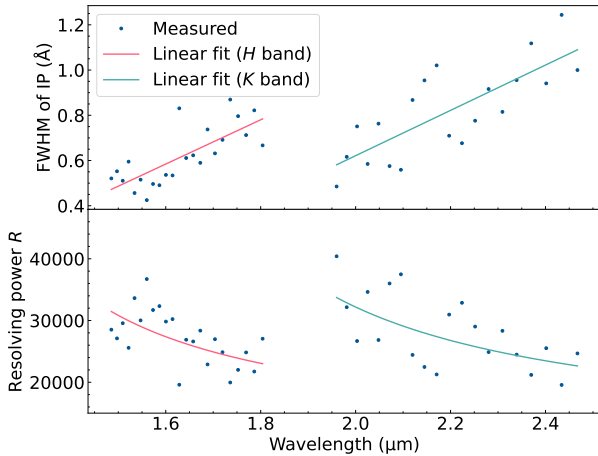


Figure 3. The FWHM of the instrumental broadening profile IP of our spectra (top) and its corresponding resolving power R (bottom) as a function of wavelength. The data points indicate our measurements for the individual used clean telluric lines in the A0V spectra. The red and green solid lines are based on the linear fits of the FWHMs (Equations 1 and 2).

RV offsets for each component of the binary. For Luhman 16A, these were $12 \leq v \sin i / (\text{km s}^{-1}) \leq 17$, step size of 0.2 km s^{-1} , and $16 \leq \text{RV} / (\text{km s}^{-1}) \leq 18$, step size of 0.05 km s^{-1} . For Luhman 16B, these were $22 \leq v \sin i / (\text{km s}^{-1}) \leq 28$, step size of 0.2 km s^{-1} , and $19 \leq \text{RV} / (\text{km s}^{-1}) \leq 22$, step size of 0.05 km s^{-1} .

The model photospheres have a higher spectral resolution ($R > 100\,000$) and 3–7 times finer wavelength sampling than the data. We first convolved the models to account for rotational and IP broadening. For the IP, we used a Gaussian with a variable FWHM as a function of wavelength, as determined from Equations 1 and 2. We then resampled the model photospheres to match the wavelength sampling for the data.

We computed the reduced chi-square goodness-of-fit statistic (χ_R^2) for each point on the model photosphere grid. We incorporated a quadratic fit to the continuum in each order as a free parameter in

the fitting, to correct for instrumental effects that curve the spectra towards the ends. As noted in Tann22, the quadratic function helps account for any systematic trends with wavelength from the blaze correction or from discrepancies between the spectra and the model photospheres. The parameters at the grid point with the smallest χ_R^2 were considered the best-fit values for each order.

In Tann22, the χ_R^2 values were scaled so that the χ_R^2 in the best-fit order was unity. However, we modified this approach to avoid over-weighting relatively featureless orders when calculating the global best-fit parameters (Section 4.1). For each object, the χ_R^2 values for all orders were adjusted so that the mean of the lower half of the χ_R^2 values is unity (Figure 4). This adjustment is not based on a strict statistical justification, but rather on practical considerations. Our primary goal is to prevent overweighting of orders with few absorption features and poor diagnostic power that may otherwise dominate the final estimates of atmospheric parameters because of their very low χ_R^2 values. This approach allows us to balance the contribution of all orders, ensuring that spectral regions with significant absorption features and good diagnostic power are appropriately weighted. We calculated the adjusted χ_R^2 by adding an extra systematic uncertainty, σ_M , in quadrature to the observational uncertainty on the data. This σ_M is attributed to a combination of the scatter of the actual IP widths around the adopted (fitted) values as a function of wavelength (Figure 3) and a systematic uncertainty of the model. The obtained values for σ_M are 1.6% and 1.4% of the normalized flux for Luhman 16A and B, respectively. We hereafter adopt the notation χ_R^2 to denote the updated computation of the reduced chi-square. The best-fit model for each order overlotted on the observed spectrum is shown in the spectral atlas in Appendix B across all orders for both objects.

3.2 Fitting Component A Using Component B as a Template

The two components of the binary Luhman 16A and B likely share the same formation and evolution history. However, the slight differences in mass and temperature give rise to the slight differences in their atmospheric chemistry. The differences are particularly interesting in the case of this binary, as its components narrowly span the L/T transition and the associated change in atmospheric composition.

To directly compare the spectral features of the two components, we broadened and shifted the spectra of the more slowly rotating

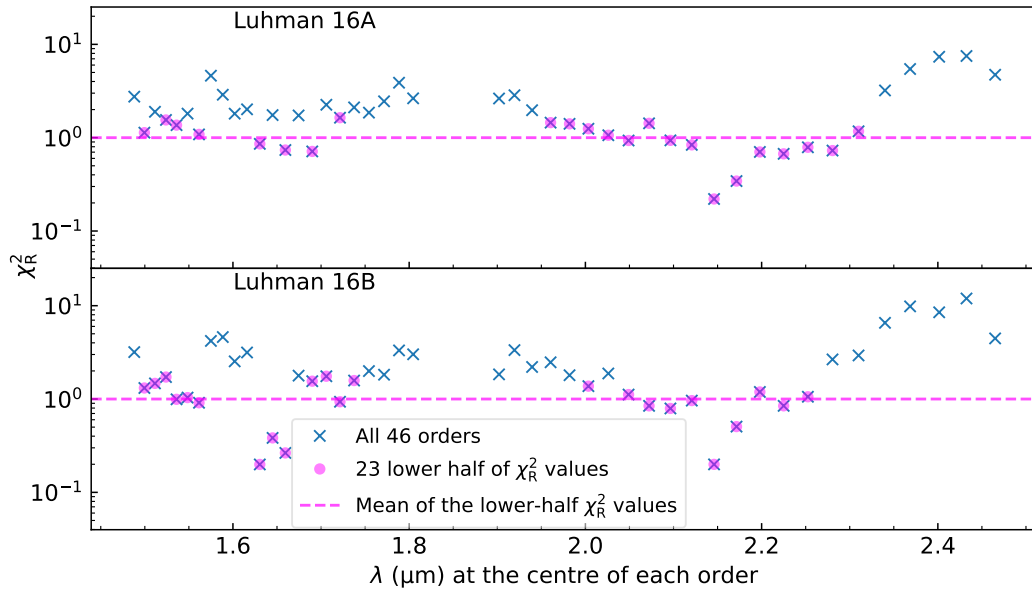


Figure 4. Fitting of photospheric models. The two panels show best-fit χ_R^2 values in each order as a function of the central wavelength of the order, for each binary component. The 23 pink circles highlight the lower half of the χ_R^2 values. The χ_R^2 values were re-evaluated by adding a 1.6% (for Luhman 16A) or 1.4% (for Luhman 16B) systematic uncertainty σ_M in the model, so that the mean of these 23 values is unity (Section 3.1).

Luhman 16A to match those of B to compensate for the differences in rotational and radial velocities. The values for the broadening and shifting are selected to minimize the χ_R^2 of the fit for each order after applying the quadratic correction to the continua to remove instrumental effects, as done for the model fitting in Section 3.1.

Example matched spectra in orders $m = 74$ and 117 are plotted in Figure 5 along with the predicted absorption from individual molecules in a separate panel. Differences that are noticeable in the peaks and troughs of the spectra indicate intrinsic differences between the spectra of the two objects. The insights for individual molecules from the comparison are discussed in Section 4.2.

4 RESULTS AND DISCUSSION

4.1 Determination of physical parameters

We show the best-fit parameters and χ_R^2 values across all orders for Luhman 16A and B, in panels (c) to (i) in Figures 6 and 7, respectively. The weighted average and 1σ standard deviation range for each parameter are indicated by the dashed and dotted horizontal lines in each panel. The noticeable trends for each parameter and χ_R^2 are discussed in the following paragraphs. For reference, panel (a) shows the order-stitched IGRINS spectrum, and panel (b) shows the model spectra calculated at the global best-fit parameters with individual molecular species only, in addition to continuum opacity from collision-induced absorption (CIA) by molecular hydrogen and helium. This helps to identify the dominant line absorbers in each wavelength region as reported in Table 1. However, because the individual molecule spectra exclude significant opacity from other molecular absorbers, the predicted absolute strengths are not reliable.

Small χ_R^2 values are observed particularly in wavelength ranges where molecular absorption is weak. As we approach the edges of both H and K bands, H_2O absorption becomes stronger, and χ_R^2

increases. Additionally, around $1.57 \mu\text{m}$ ($m = 114$ for both objects and also $m = 113$ for Luhman 16B), relatively large χ_R^2 values are shown, which coincide with a bandhead position of FeH.

The best χ_R^2 values for the individual orders were used in the same manner as Tann22 to estimate the global best-fit parameters for T_{eff} , $\log g$, f_{sed} , $\log C_{K_{zz}}$, $v \sin i$, and RV, of each object. We took the weighted average of 46 best-fit values across all 23 H - and 23 K -band orders with the weights calculated as $\exp(-\frac{1}{2}\chi_R^2)$. The global best-fit parameters are shown in Table 2. The uncertainty for each parameter is obtained as the unbiased weighted standard deviation of the best-fit values for individual orders.

The T_{eff} estimates for Luhman 16A and B have been known to be comparable within the uncertainties (the difference is about 15–30 K) based on the bolometric luminosities (Faherty et al. 2014; Lodieu et al. 2015). Our global best-fit parameters show a difference of 70 K with uncertainties of 80 K. However, the spectral fitting in nine orders, $m = 73, 75\text{--}78, 80, 81, 86,$ and 111, results in T_{eff} differences of 200 K or more (compare Figures 6 and 7). These orders coincide with wavelength regions of CH_4 absorption. This is to be expected, since the volume mixing ratio (VMR) of CH_4 is most sensitive to temperature at the L-to-T transition, compared to other species (Figure 8). To be sure, CH_4 lines are weak in both objects and do not significantly affect the overall shape of the spectra (Section 4.2.4). Nonetheless, our high-SNR data with high spectral resolution capture their T_{eff} dependence. Elsewhere in the H band, the difference in T_{eff} estimates between the two objects is generally small, suggesting that H_2O absorption lines in the H band are relatively insensitive to T_{eff} . The K -band spectra, and in particular their CH_4 line content, seem to be more sensitive to T_{eff} for brown dwarfs at the L/T transition.

Results for $\log g$ are generally consistent across orders, indicating $\log g = 5.0$ for both objects. Some orders are fit by a value of 4.5 or 5.5 dex for both objects, which points to systematics in the models.

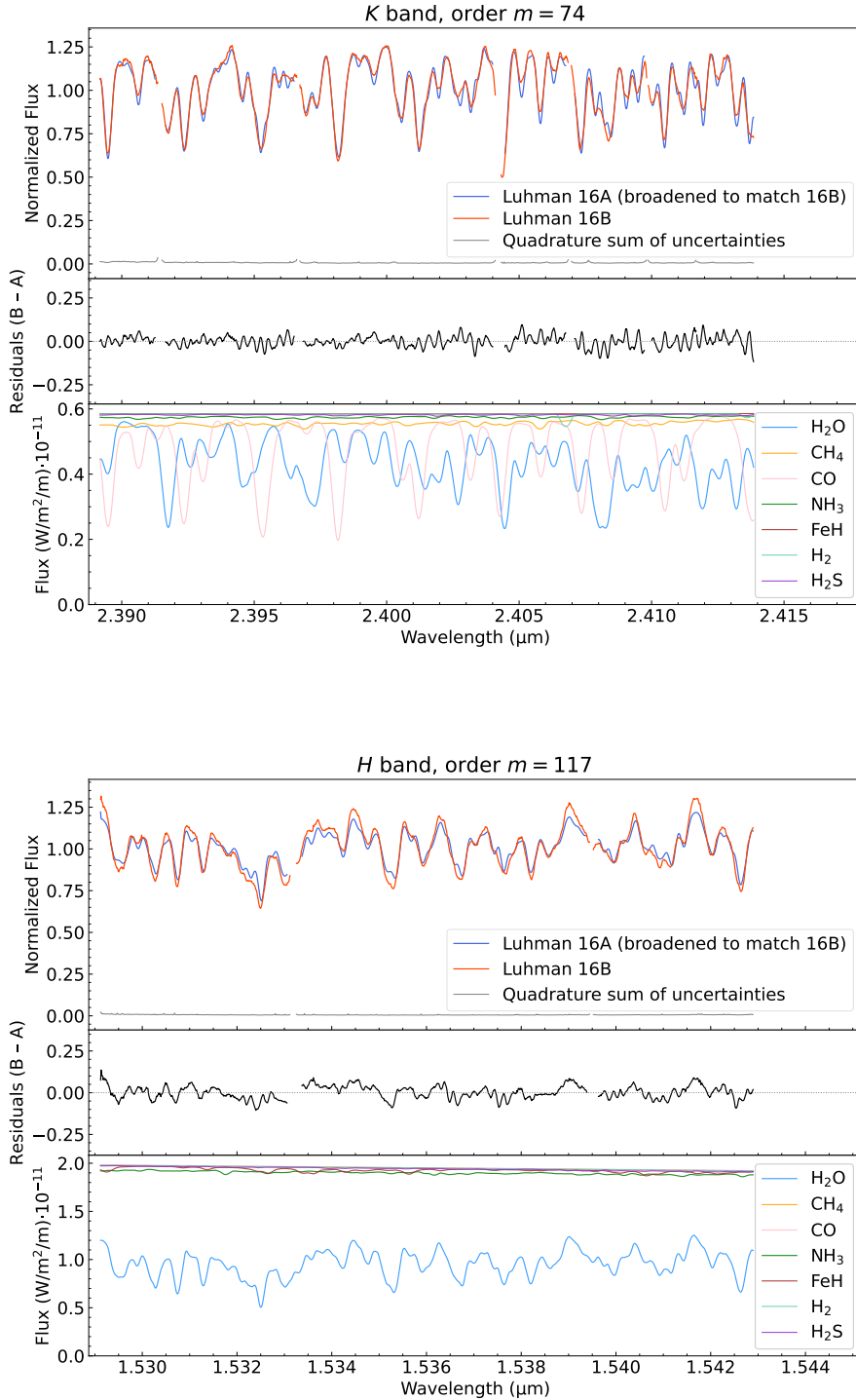


Figure 5. Comparison of the velocity-shifted and broadened spectra of Luhman 16A in orders $m = 74$ (upper set of panels, showing strong CO and H₂O absorption) and 117 (lower set of panels, dominated by H₂O) to those of Luhman 16B. Velocity broadening and shifting were applied to minimize the difference between the two spectra in each order. The top panel in each set shows both spectra and the second panel depicts the difference between them. The bottom panel displays single-molecule absorption spectra that include only line opacities from the respective molecule and continuum opacity from collision-induced H₂ and He absorption. The single-molecule spectra are calculated for the global best-fit parameters for Luhman 16B (Table 2).

The f_{sed} parameter was not strongly constrained by our modelling analysis.

More than half of the orders support nominal values for K_{ZZ} . However, the middle of the H band prefers larger K_{ZZ} and the redder part of the K band prefers smaller K_{ZZ} . The former region is sensitive to FeH features, and the latter to CO features, from which we infer that the volume mixing ratios (VMR) of these molecules are affected by disequilibrium processes.

The results for $v \sin i$ and RV are consistent across all wavelengths. The reason for the larger dispersion in RV for Luhman 16B is the greater line broadening by faster rotation. Our global best-fit value of $v \sin i$ for Luhman 16A is slightly smaller than previous estimates (Crossfield et al. 2014; Kawahara et al. 2022). This is likely due to our lower spectral resolution, which is insufficient to measure the $v \sin i$ of this object accurately, and so our analysis may underestimate the value.

Our estimates of the stellar parameters are generally consistent with the recent determinations by Chen et al. (2024) and more precise. Chen et al. (2024) used the Sonora Diamondback models, which include clouds but do not treat chemical disequilibrium, so the difference of best-fit values in f_{sed} could be attributed to the disequilibrium effects that are incorporated in our custom Sonora Bobcat Alternative B models.

Combining our $v \sin i$ for Luhman 16B of $24.9 \pm 0.8 \text{ km s}^{-1}$ with its radius of 1.02 ± 0.07 Jupiter radii (R_{J}) estimated by Filippazzo et al. (2015) and its rotation period of 5.28 hr derived photometrically by Apai et al. (2021, 5.25 hr in the follow-on study by Fuda et al. 2024), we evaluated its spin axis inclination to be $> 73^\circ$, supporting the Apai et al. (2021) estimate of an almost equator-on view. This also agrees with the orbital inclination of $79.92 \pm 0.01^\circ$ (Bedin et al. 2024), indicating that the rotation axis of Luhman 16B is aligned with the orbital axis of the binary system. The 6.94-hr rotation period of Luhman 16A tentatively suggested by Apai et al. (2021) combined with our $v \sin i$ ($13.9 \pm 0.9 \text{ km s}^{-1}$) and its radius ($1.01 \pm 0.07 R_{\text{J}}$) from Filippazzo et al. (2015) yields a spin axis inclination of $50_{-6}^{+7}^\circ$, in modest misalignment with the binary orbit, while it should be noted that the suggested underestimation of the $v \sin i$ of Luhman 16A may change the conclusion.

4.2 Features of individual molecular species

Table 1 lists the molecular line absorbers in each IGRINS order along with the correspondence of the orders and wavelengths. Most parts of our spectra are dominated by H_2O and in some regions CO also exhibits strong features. Absorption by FeH, CH_4 , and NH_3 produces more subdued effects in some wavelength regions. We also detect absorption by individual lines of H_2 at 2.1218 μm , 2.2233 μm , and 2.4066 μm , and H_2S at 1.5900 μm . Tann22 were the first to detect H_2 or H_2S in a star-like object outside the solar system: a T6 dwarf. Hood et al. (2023) and Lew et al. (2024) subsequently reported H_2S in a T9 dwarf and a Y dwarf, respectively. The detections here show that H_2 and H_2S are seen at high spectral resolution in brown dwarfs as early as L7.5.

The vertical profiles of the VMR of the major chemical species expected in the target atmospheres are shown in Figure 8 based on the model atmospheres with the best-fit parameters for individual orders. Species whose profiles are plotted as solid lines here have their spectral features discussed in the following sections.

4.2.1 Water

The most prominent molecular absorber is water (H_2O), which contributes most of the line absorption in the H and K bands and forms a pseudo-continuum in many parts. The direct comparison of Luhman 16A and 16B shows the water lines to be nearly identical in strength in the two objects (e.g., Figure 5), even if at some wavelengths the absorption is slightly stronger in component A (e.g., the 2.408–2.414 μm region in Figure 5, top) while at others it is slightly stronger in B (e.g., the 1.529–1.543 μm region in Figure 5, bottom).

Tann22 found the ExoMol/POKAZATEL water line list from Polyansky et al. (2018) to be the most reliable in fitting the IGRINS spectrum of a T6 dwarf with their Bobcat Alternative A model. This is also the water line list used in the present Bobcat Alternative B model, and we confirm that the fits to the spectra are satisfactory. Nevertheless, we do find that in some spectral regions dominated by water, the residuals between the observed spectra and the best-fit model exhibit P Cygni profile-like features, indicative of slight ($< 1 \text{ nm}$) inaccuracies of some water line wavelengths. A comparison to the T6 dwarf spectrum and modelling in Tann22 confirms that they are present for that object, too. A discussion of these residuals in the context of other potential new features or contributions from isotopologues is presented in Section 4.3.3.

4.2.2 Carbon monoxide

The second most prominent absorber in the spectra is carbon monoxide (CO), with three bandheads at 1.558 μm , 1.578 μm , and 2.294 μm . The absorption lines in the K band are particularly strong, comparable to those of H_2O , and depress the continuum in orders $m = 72\text{--}78$. The comparison between Luhman 16A and B in Figure 5 (top panel) and in Figure 9 shows that the difference in the normalized depths of CO lines between the two components is almost negligible. CO absorption strength in Luhman 16B is only $\lesssim 5\%$ stronger at the 2.3 μm bandhead. The H -band CO lines show no significant difference between the two objects.

This follows expectations from the Sonora Bobcat models. The CO mixing ratio decreases with decreasing temperature from the L dwarfs into the T dwarfs as CH_4 consumes more carbon. However, this is offset by a predicted increase in the CO absorption line strength with decreasing T_{eff} at the L/T transition. The trade-off between these two effects results in the normalized depth of the CO lines being insensitive to the T_{eff} across the L/T transition.

4.2.3 Iron hydride

Iron hydride (FeH) has absorption lines in the wavelength range of 1.58–1.72 μm (orders $m = 104\text{--}114$) in the H band. Our model, which assumes solar chemical composition, predicts a strong contribution from FeH in the spectrum of Luhman 16A (Figure 6b) and a more subdued one in Luhman 16B (Figure 7b). The strongest effect of FeH absorption should be detectable at the 1.582 μm bandhead, where its contribution should jump from zero to nearly half of the atmospheric line opacity in Luhman 16A (Figure 6b and bottom panel of Figure 10). However, no FeH bandhead is visible in our spectra of either Luhman 16 component (Figures 6a and 7b). A comparison of the best-fit models to Luhman 16A with and without FeH shows that the addition of FeH is not favoured with the global best-fit parameters (Figure 10, middle panel).

There is also no appreciable difference between Luhman 16A and 16B at the FeH bandhead (Figure 11), despite expectations based on their slightly different spectral types and effective temperatures.

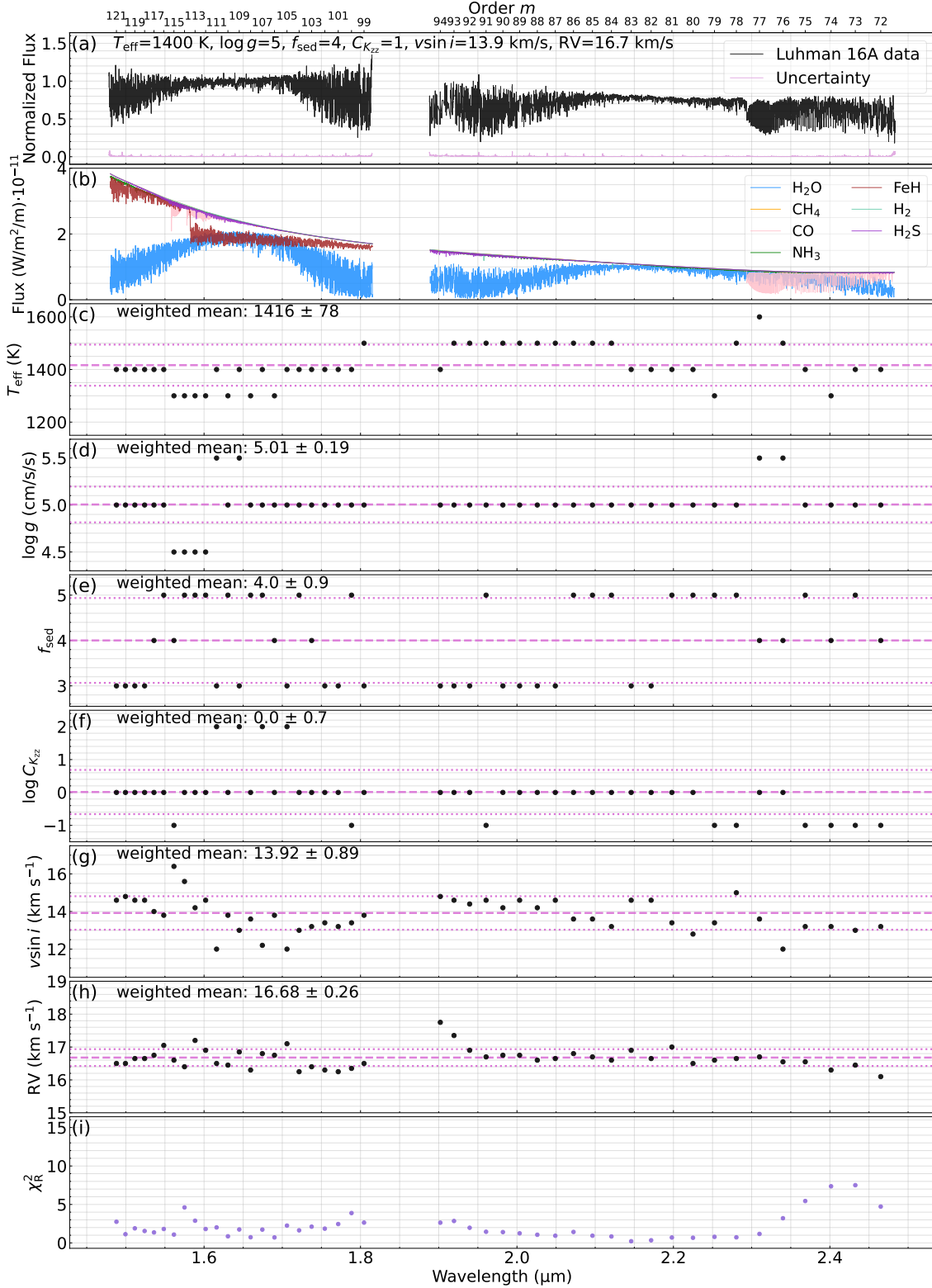


Figure 6. Results of the parameter estimation from the model fitting for Luhman 16A. Panel (a): IGRINS spectrum normalized to unity over the 1.6–1.7 μm wavelength range after masking telluric lines and stitching the orders across each band. The IGRINS echelle order numbers (m) are shown along the top axis. Panel (b): Individual molecular absorption spectra with CIA continuum opacity due to H₂ and He included, resampled to match the spectral resolution of IGRINS. The y axis indicates the model flux expected at the surface of the object. Because the individual absorber spectra exclude significant opacity from other molecules, they are used only as an indication where absorption may be expected, rather than as a representation of the actual absorption strength. Six panels from (c) to (h): the stellar parameters of the best-fit model for each order. From the top to bottom, the parameters are as follows: T_{eff} , $\log g$, f_{sed} , $\log C_{K_{zz}}$, $v \sin i$, and RV. The weighted average of each parameter is given in the upper left corner. The dashed and dotted horizontal lines indicate the weighted average and 1σ range. Panel (i): The χ_R^2 value for each order as an indicator of goodness of fit, adjusted as described in Section 3.1.

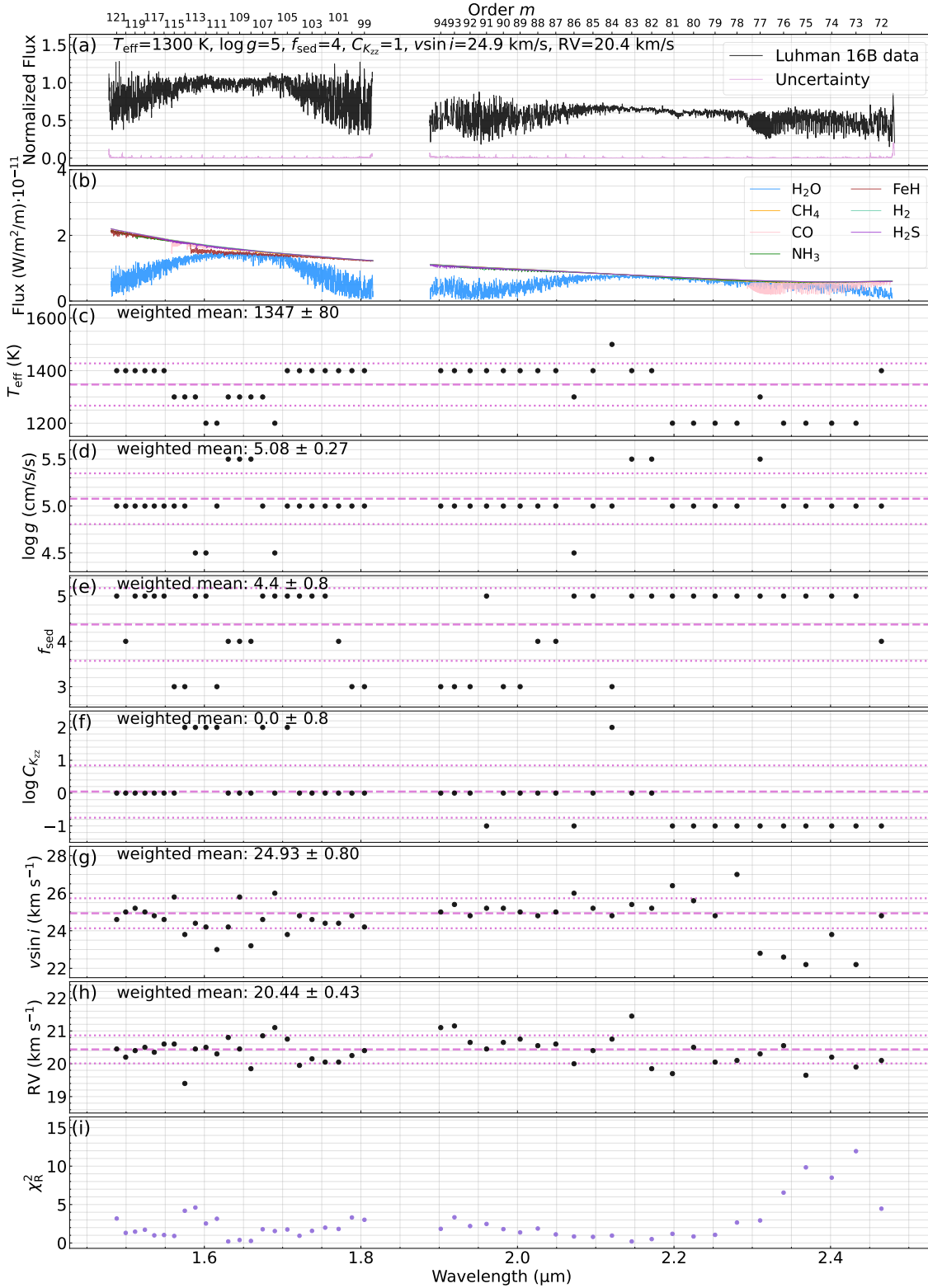


Figure 7. Same as Figure 6 but for the cooler component, Luhman 16B. While most parameters are estimated with similar precision to those of Luhman 16A, the uncertainty of the RV is larger here due to the broader line width caused by the faster rotation. The wavelength dependence of each estimated parameter or χ_R^2 shows a similar distribution to that of the hotter counterpart.

Table 2. Best-fit photospheric model parameters determined for the IGRINS spectra of Luhman 16A and B.

Parameter	Luhman 16A	Luhman 16B
Effective temperature, T_{eff}/K	1416 ± 78	1347 ± 80
Surface gravity, $\log(g/\text{cm s}^{-2})$	5.0 ± 0.2	5.1 ± 0.3
Sedimentation efficiency parameter, f_{sed}	4.0 ± 0.9	4.4 ± 0.8
Vertical eddy diffusion coefficient, $^a \log C_{K_{zz}}$	0.0 ± 0.7	0.0 ± 0.8
Projected rotational velocity, $v \sin i / (\text{km s}^{-1})$	13.9 ± 0.9	24.9 ± 0.8
Radial velocity, $RV / (\text{km s}^{-1})$	16.7 ± 0.3	20.4 ± 0.4

^a $K_{zz} = \text{nominal value} \times C_{K_{zz}}$, where the units of K_{zz} are $\text{cm}^2 \text{s}^{-1}$. See Section 3.1 for more details.

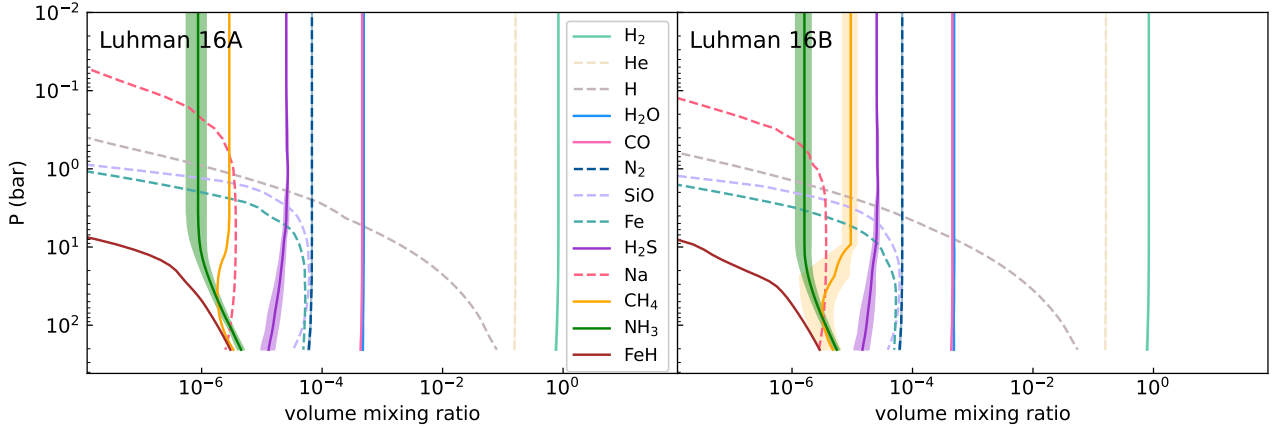


Figure 8. The vertical profiles of the chemical abundances expected for the Luhman 16A (left) and B (right) atmospheres based on the model fitting. The solid line shows the average profile of the best-fit models of 46 individual orders, and the shaded area shows the range of 1σ above and below it. The plot shows the VMR of the top 13 most abundant chemical species in the $P=10$ -bar layer. This illustrates their relative abundances across different pressure levels.

The FeH-only model calculated with the global best-fit parameters predicts stronger FeH absorption in the spectrum of Luhman 16A compared to B (panel (b) in Figures 6 and 7), while such is not seen in the difference of the two spectra.

The local best-fit photospheric models favour lower T_{eff} and higher K_{zz} than those in the global best-fit models in the FeH-affected orders ($m = 109$ – 114) for both Luhman 16A and B (panels c and f of Figures 6 and 7). Both lower T_{eff} and stronger vertical mixing result in a cooler temperature-pressure profile for the entire atmosphere, which would agree with weaker FeH absorption. We thus suspect that the model may not fully capture the efficiency of the iron rainout (e.g., Burgasser et al. 2002; Cushing et al. 2003) that removes iron from the atmosphere at temperatures below ~ 1500 – 2000 K (Visscher et al. 2010). The Sonora Bobcat model already has the FeH line strengths (from Hargreaves et al. 2010) scaled down by a factor of $1/3$ to account for discrepancies with early-L dwarf spectra (Marley et al. 2021). We find that an even further decrease of the overall FeH opacity would be needed—amounting to a near-complete condensation of iron at the L/T transition—to explain the observation that neither Luhman 16A nor B shows signs of FeH absorption.

4.2.4 Methane

Methane (CH_4) lines are not strongly expressed in the spectra of our L7.5 and T0.5 targets. Nonetheless, we do detect significant differences between the spectra of Luhman 16A and B in the wavelength regions where CH_4 absorption is expected. Around $1.64 \mu\text{m}$ (or-

ders $m = 109, 110$) and $2.20 \mu\text{m}$ (orders $m = 78$ – 81), comb-like residuals appear in the difference between the spectra of Luhman 16B and 16A. Figure 12 shows that these features are aligned with the wavelengths of CH_4 lines, even though most parts of the nearby pseudo-continuum are determined by H_2O . Methane absorption is thus weak but diagnostic at the L/T transition: it is not the strongest absorber at the $1.6 \mu\text{m}$ and $2.2 \mu\text{m}$ methane bandheads even in the T0.5 dwarf, but shows the strongest sensitivity to temperature (Section 4.1).

4.2.5 Ammonia

Although ammonia (NH_3) is characteristic of the much colder Y spectral type and is known to exhibit prominent features at lower temperatures (e.g., Delorme et al. 2008; Cushing et al. 2011), it has also been detected in a high-SNR IGRINS spectrum of a T6 dwarf by Tann22.

In our spectra, there is only a very limited region in orders $m = 78$ – 82 where the NH_3 opacity exceeds that of other molecules. The NH_3 opacity is small and most of the lines are veiled by H_2O lines. Figure 13 shows the the IGRINS order in which the NH_3 lines can be most easily discerned. Models with NH_3 opacity reproduce the spectra for both objects slightly better, especially for Luhman 16B, than models without NH_3 opacity. Notably, the strongest residuals from models lacking NH_3 opacity are at the wavelengths where NH_3 absorption is expected. The effect is more strongly noticeable for Luhman 16B, but the same wavelengths also show NH_3 -related residuals in Luhman

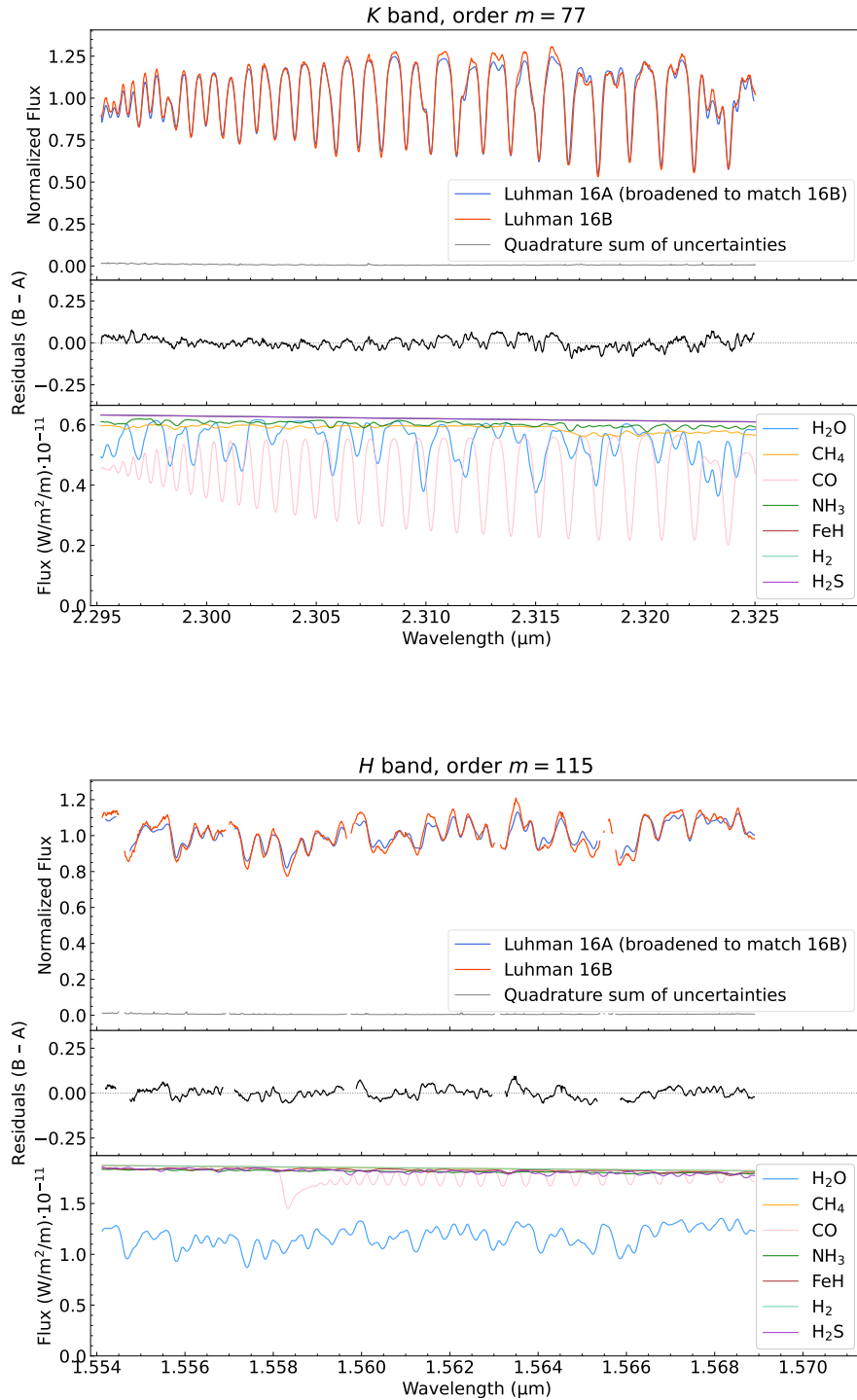


Figure 9. Comparison of Luhman 16A and B as in Figure 5 but for orders $m = 77$ (K band) and $m = 115$ (H band) where the CO absorption lines are prominent.

16A. This makes Luhman 16A one of the warmest $1416 \pm 78\text{K}$; Table 2 atmospheres with robust NH_3 detection along with DENIS J025503.3–470049 (L9; de Regt et al. 2024).

4.2.6 Molecular hydrogen

Both Luhman 16A (L7.5) and 16B (T0.5) spectra show unambiguous detections of molecular hydrogen (H_2) lines. This is only the second report of H_2 detection in substellar objects outside the solar

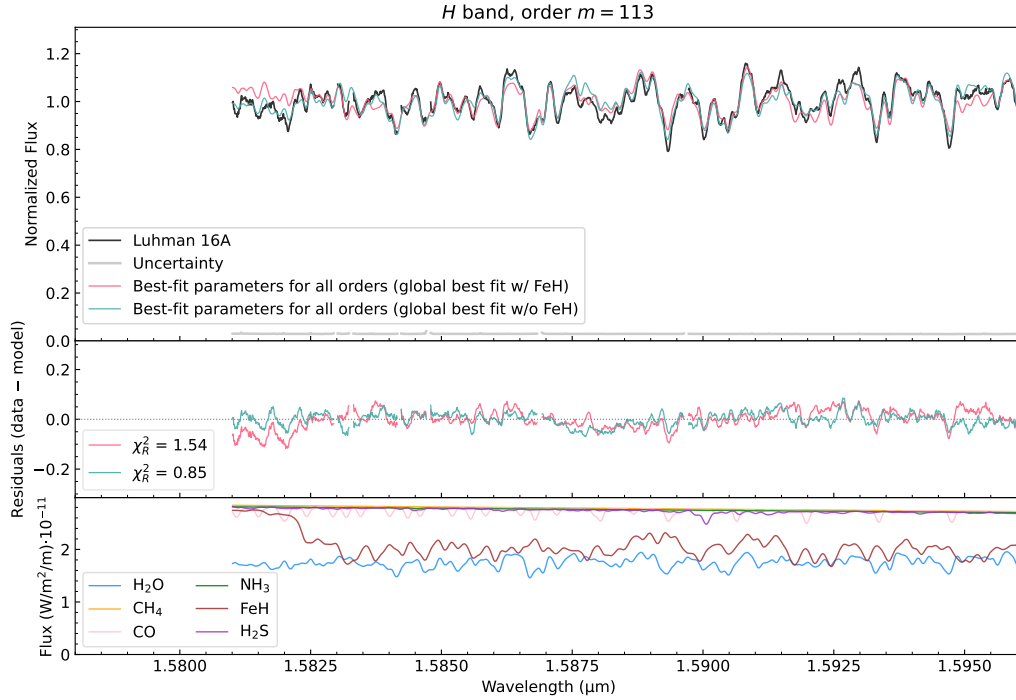


Figure 10. A test of the required FeH opacity contribution in photospheric models of Luhman 16A. Order $m = 113$ contains the FeH bandhead at $1.582 \mu\text{m}$, which is expected to nearly double the atmospheric line opacity dominated by water. The data (in black) and its uncertainty (in gray) are plotted in the top panel, along with two global best-fit model photospheres ($T_{\text{eff}} = 1400 \text{ K}$, $\log g = 5.0$, $f_{\text{sed}} = 4$, $C_{K_{zz}} = 1$): one including FeH opacity (red spectrum) and one without FeH opacity (green spectrum). The second panel shows the residuals between the data and the respective models, where the legend indicates the χ_R^2 values. The bottom panel shows the models for individual molecular species and CIA by H_2 and He. They are calculated with the global best-fit parameters for Luhman 16A.

system, following the discovery of the $1-0 \text{ S}(1)$ quadrupole transition $2.1218 \mu\text{m}$ H_2 line in the IGRINS spectrum of a T6 dwarf by Tann22.

Figure 14 shows the spectral fit for order $m = 84$ where the $2.1218 \mu\text{m}$ H_2 line appears in both objects. It illustrates that the addition of H_2 in the model makes the residuals flatter and improves the χ_R^2 value of the fit. While this is the most significant detection, we also found indications of other absorption lines by H_2 . The $1-0 \text{ S}(0)$ line at $2.2233 \mu\text{m}$ ($m = 80$, Figure B1) is relatively shallow, but thanks to the excellent reproduction of the surrounding H_2O lines in the model, we found that the addition of H_2 to the model improves the χ_R^2 value. The $1-0 \text{ Q}(1)$ line at $2.4066 \mu\text{m}$ ($m = 74$, Figure B2) is in a wavelength range crowded with telluric lines, but both visually and in terms of the χ_R^2 , the fit also improves with the addition of H_2 . Some other promising H_2 lines either fall into the gap between the K and H bands (e.g., 1.8358 , $1.8919 \mu\text{m}$) or are obscured by stronger water absorption (e.g., $1.7480 \mu\text{m}$ in order $m = 102$, $1.9576 \mu\text{m}$ in order $m = 91$, $2.0337 \mu\text{m}$ in order $m = 88$) and are not detected.

Despite being the most abundant gas in substellar atmospheres, H_2 is difficult to detect because it has no dipole transitions because of its symmetric structure. We detect quadrupole transitions, which are weak, and prior to Tann22 have only been seen in solar system giant planets. The observation of the quadrupole lines of H_2 was predicted by Herzberg (1938) and identified in the spectra of Uranus and Neptune by Herzberg (1952). These lines have been used to infer hydrogen abundances, ortho-para ratios, atmospheric vertical structures and cloud distributions (e.g., Fletcher et al. 2017; Carlson et al. 1992; Tanaka 1966). More recently, Atai et al. (2021) and

Atai & Farziyev (2021) have detected H_2 quadrupole lines at optical wavelengths in the atmospheres of all four solar-system giant planets and use these to estimate the physical parameters of the absorption layer and the content of molecular hydrogen.

As done in Tann22, we estimate the H_2 column density (N_{H_2}) and dust extinction in the H_2 absorbing layer by comparing to ISM-like conditions. We assume that the top of the absorbing layer is set by the brightness temperature (T_b) of the continuum around the H_2 line in the best-fit model spectra. The temperature-pressure ($T - P$) profile of the atmospheric model can then be used to infer the pressure of the absorbing layer (Figure 15): $P_{\text{abs}} = 2.6 \text{ bar}$ for Luhman 16A and $P_{\text{abs}} = 3.5 \text{ bar}$ for Luhman 16B. We then computed the local number density of H_2 molecules for each atmospheric layer with the ideal gas law and a model-informed VMR of H_2 , which is approximately constant of 0.84 in all atmospheric layers of interest in both objects. Since the physical distance between each layer can be calculated from the density and pressure difference, we integrated the H_2 number density from P_{abs} to the top of the atmosphere to obtain column densities of $N_{\text{H}_2} \sim 4.7 \times 10^{25} \text{ cm}^{-2}$ for Luhman 16A and $N_{\text{H}_2} \sim 6.5 \times 10^{25} \text{ cm}^{-2}$ for Luhman 16B. As done in Tann22, we adopt the K -band extinction law of Cardelli et al. (1989) and assume that all the hydrogen is comprised of H_2 molecules, which yields H_2 column density per magnitude of ISM-like K -band extinction of $N_{\text{H}_2}/A_K = 0.97 \times 10^{22} \text{ cm}^{-2} \text{ mag}^{-1}$. If the gas-to-dust ratios in our targets were ISM-like, these N_{H_2} values would correspond to K -band extinctions of $A_K \sim 4900 \text{ mag}$ and $\sim 6700 \text{ mag}$ for Luhman 16A and B, respectively. The fact that the H_2 lines are clearly detected

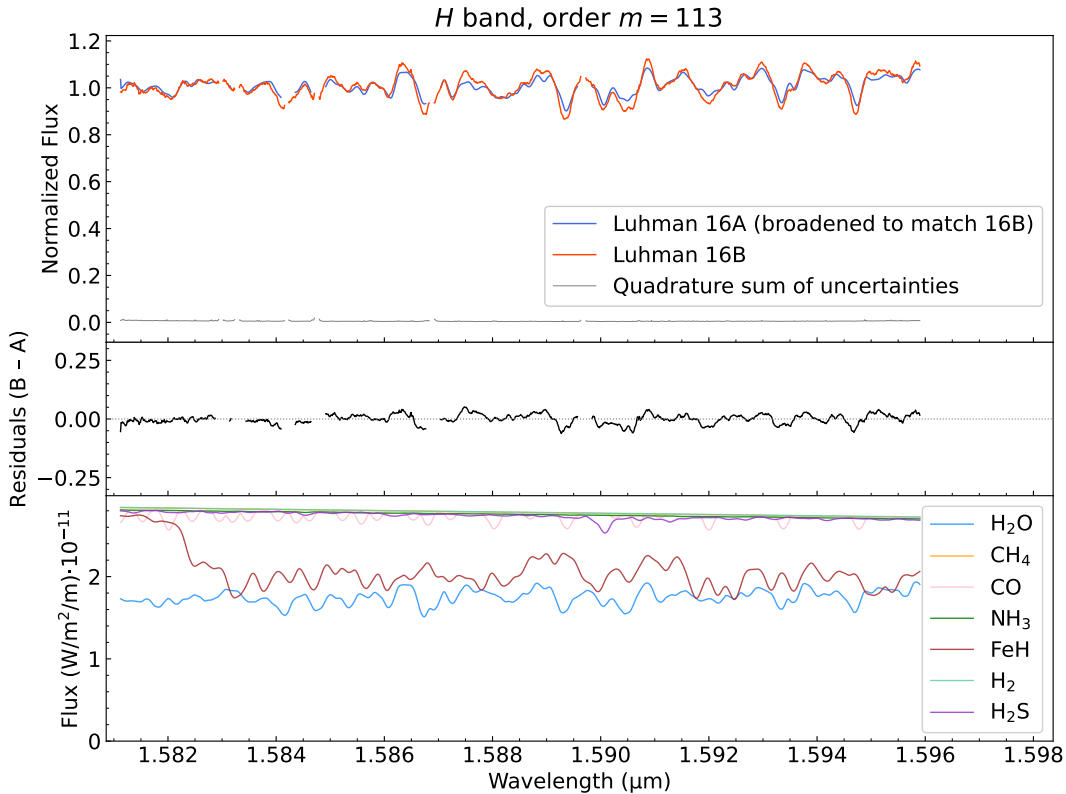


Figure 11. Comparison of Luhman 16A and B as in Figure 5, but for order $m = 113$, where the FeH absorption should be most prominent. The single-molecule spectra in the bottom panel are based on Luhman 16A’s global best-fit parameters. There is no difference between the spectra of the two objects even at the 1.582 μm onset of the FeH bandhead, contrary to expectations from the global best-fit photospheres (Section 4.2.3).

indicates that the actual dust concentration is several thousand times smaller than in the ISM. That is, the dust has separated from the gas to form clouds that reside mostly below the H_2 gas absorption layer.

A comparison to the pressure level of the cloud base in our adopted model confirms that it is at a similar or higher pressure than P_{abs} (Figure 15). This is consistent with the expected sedimentation of dust clouds below the photosphere at $T_{\text{eff}} < 1400$ K (e.g., Brock et al. 2021; Saumon & Marley 2008; Marley et al. 2010).

4.2.7 Hydrogen sulfide

As with the detection of H_2 , both Luhman 16A and 16B spectra show unambiguous detections of hydrogen sulfide (H_2S). The H_2S 1.5900 μm line in order $m = 113$ is shown in Figure 16. We also tentatively found H_2S contributions at wavelengths of 1.5687, 1.5700, 1.6163, 1.6165, 1.6265, 1.6435, 1.9094, 1.9815 and 2.4634 μm . Since the best-fit models in the spectral atlas in Appendix B do not include H_2S opacity unless otherwise stated, the small dips at those wavelengths seen in the (data – model) residuals can be attributed to H_2S . The 2.1084 μm feature predicted by Saumon et al. (2000) was not detected in our target or in the T6 spectrum of Tann22, nor was it reproduced in our model.

The only previous bona fide near-infrared detection of H_2S is by Tann22 in the IGRINS spectrum of a T6 dwarf. A follow-on near-infrared detection is reported tentatively in a T9 dwarf by Hood et al.

(2023) and in a Y dwarf by Lew et al. (2024). H_2S is fully expected in our atmospheric model at temperatures $\lesssim 2000$ K. However, its detection in low-dispersion near-infrared spectra is challenging because of surrounding H_2O absorption. At >3 μm thermal infrared wavelengths, H_2S has a more prominent absorption signature between 3.5–4.5 μm , which has been detected in JWST NIRSpec spectra: in the Y dwarf WISEPA J182831.08+265037.8 (Lew et al. 2024).

H_2S is the dominant sulfur-bearing species in most substellar atmospheres (e.g., Visscher et al. 2006). It is relatively under-studied, as it is challenging to detect outside the solar system. Its importance has been discussed in the literature in two cases. On the one hand, sulfur abundance can be a differentiator among planet-formation scenarios, distinguishing between pebble- or planetesimal accretion formation modes (Crossfield 2023). Since sulfur compounds are more volatile than carbon- or oxygen-bearing compounds, the C/S and O/S ratios in the atmosphere of a planet formed via pebble accretion are predicted to be higher than those of a planet formed via planetesimal accretion, for which the C/S and O/S ratios should be similar to the host star. On the other hand, H_2S is also important as a precursor of SO_2 , which is an indicator molecule for photochemical reactions (e.g., Tsai et al. 2023; Sing et al. 2024). Photochemistry is a contributing factor in setting the temperature structure and cloud composition in the upper atmospheres of irradiated planets.

The high-SNR H_2S detections in L7.5 and T0.5 dwarfs reported here, in a T6 in Tann22, and in a Y dwarf in Lew et al. (2024) can

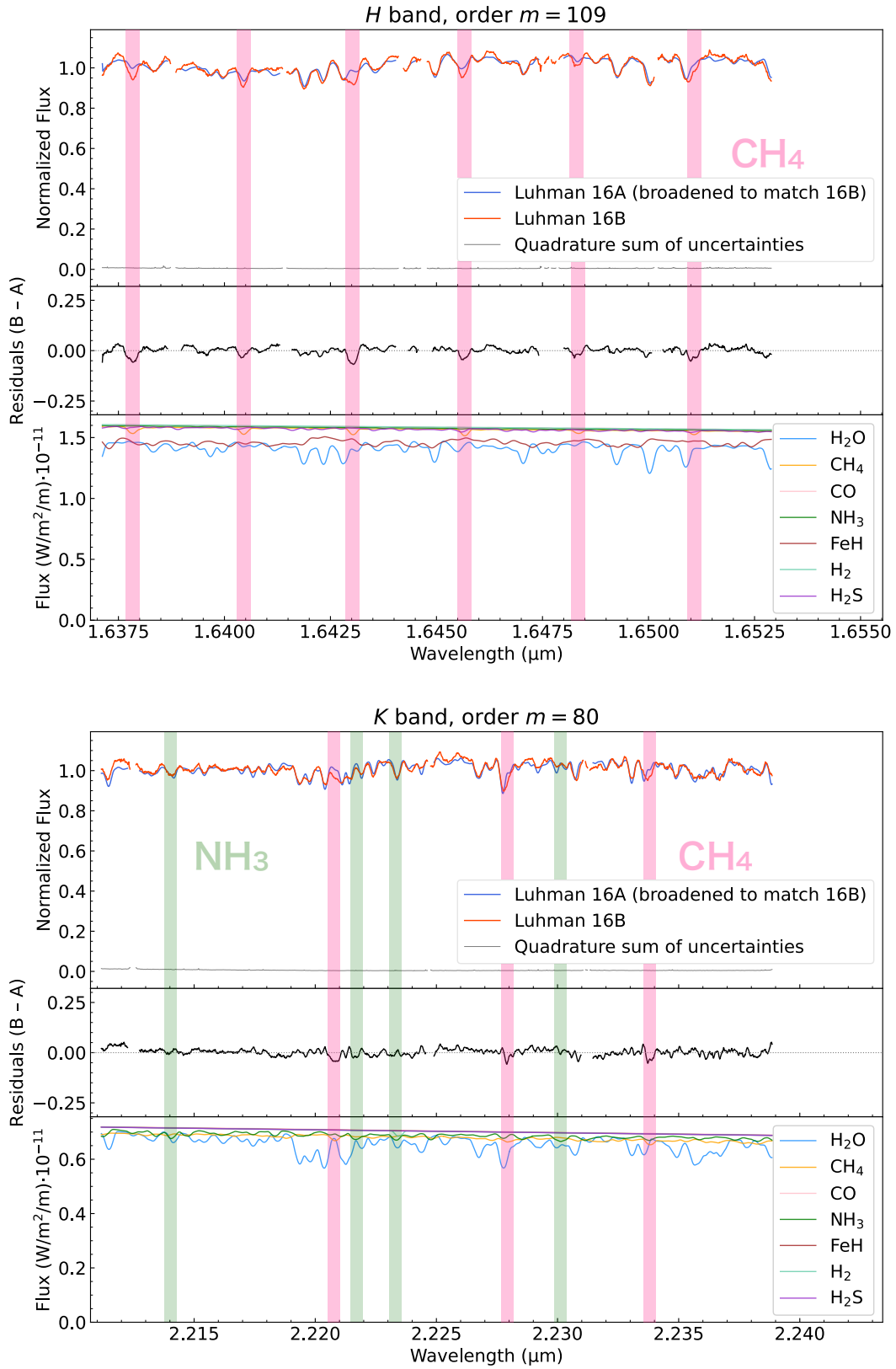


Figure 12. Methane absorption as a diagnostic of the L/T transition. The figure follows the same format as Figure 5 but for orders $m = 109$ and 80 in the upper and lower panels, respectively. The pink-shaded regions highlight CH_4 absorption and the green-shaded regions highlight NH_3 . CH_4 shows deeper absorption in the spectra of Luhman 16B than those of Luhman 16A, while differences in the depths of NH_3 lines (or any of the other molecular absorbers) are less pronounced. The model spectra of individual molecules in the bottom panels are calculated based on the global best-fit parameters for Luhman 16B.

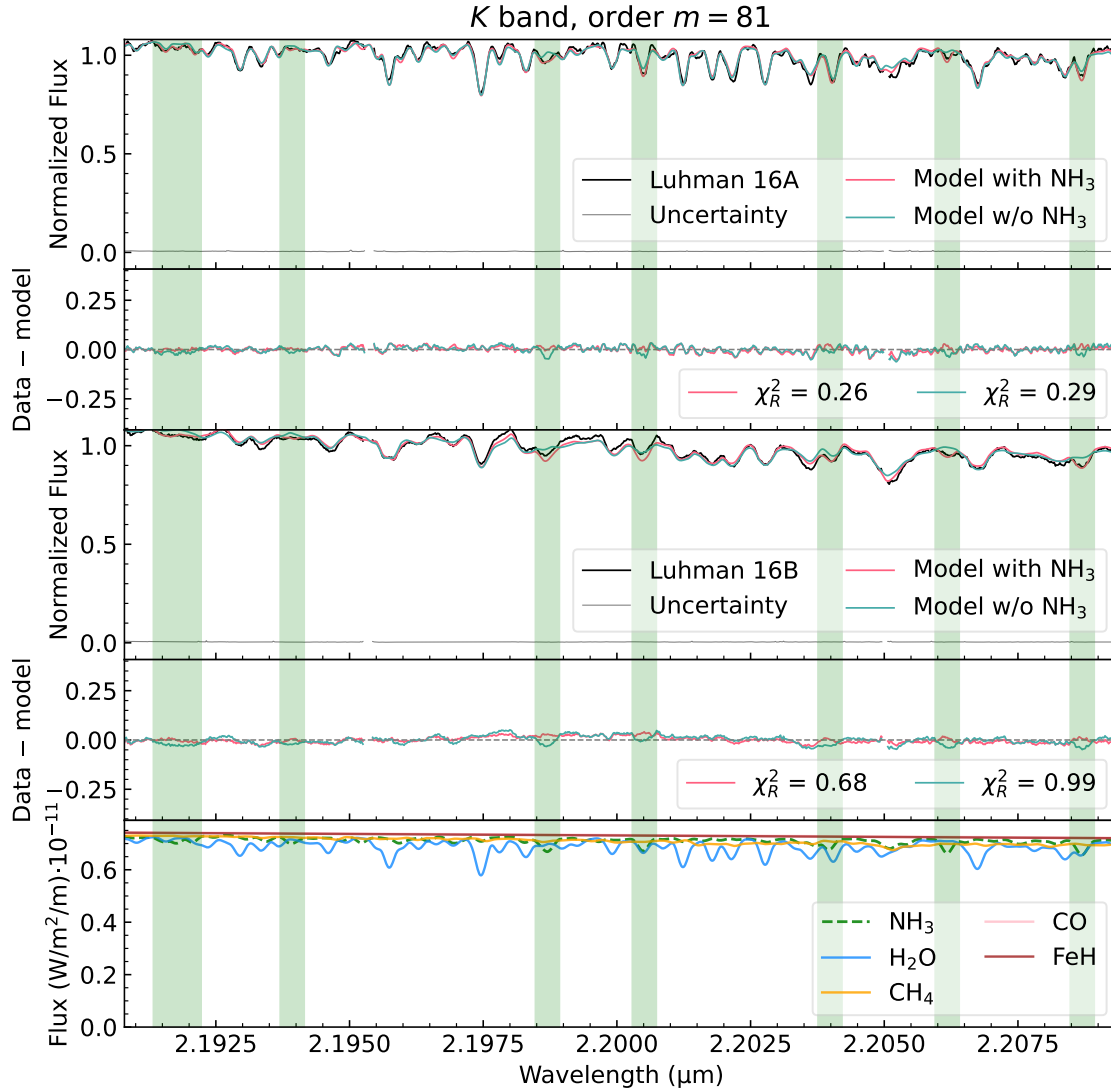


Figure 13. The $m = 81$ IGRINS order of the Luhman 16A and B spectra, demonstrating the NH_3 line detection. The data and uncertainties for Luhman 16A and B spectra, their local best-fit models with or without NH_3 opacity, and the residuals between the data and models (the legend indicates the χ_R^2 of each model fit) are shown in the top four panels. The bottom panel shows the spectra for each molecule alone with the CIA continuum, using the global (rather than local) best-fit parameters for Luhman 16B. The wavelength regions where the contribution of NH_3 is expected to be strongest are shaded in green.

be used as a baseline for future analyses of substellar atmospheres. Importantly, the atmospheric concentration of H_2S is relatively insensitive to temperature or convection. Our model shows that the VMR of H_2S is constant to within 20% at 2.5×10^{-5} for both objects in atmospheric layers with temperatures in 1000–2000 K range (Figure 17). We calculate the H_2S column densities $N_{\text{H}_2\text{S}}$ from the flux around the 1.5900 μm H_2S line, as we did for H_2 (Section 4.2.6). The computed $N_{\text{H}_2\text{S}}$ values are $\sim 1.6 \times 10^{21} \text{ cm}^{-2}$ and $\sim 2.8 \times 10^{21} \text{ cm}^{-2}$ for Luhman 16A and B, respectively. H_2S is known to be one of the main components of the clouds of Uranus (Irwin et al. 2018) and Neptune (Irwin et al. 2019). Without any anticipated H_2S condensation at the ≥ 1300 K temperatures of Luhman 16A or B, our $N_{\text{H}_2\text{S}}$

estimates are respectively 6–270 times and 10–470 times higher than those for the solar system ice giants.

4.2.8 Hydrogen fluoride

We extend the line search to hydrogen fluoride (HF) following the reports of HF detections in young late-M dwarfs (González Picos et al. 2024), a directly imaged young super-Jupiter (Zhang et al. 2024), and isolated, likely 0.02–3 Gyr, L4–L5 dwarfs (Mulder et al. 2025). We compared the locations of the expected HF lines (Coxon & Hajigeorgiou 2015) to our residuals (data – model) and confirmed

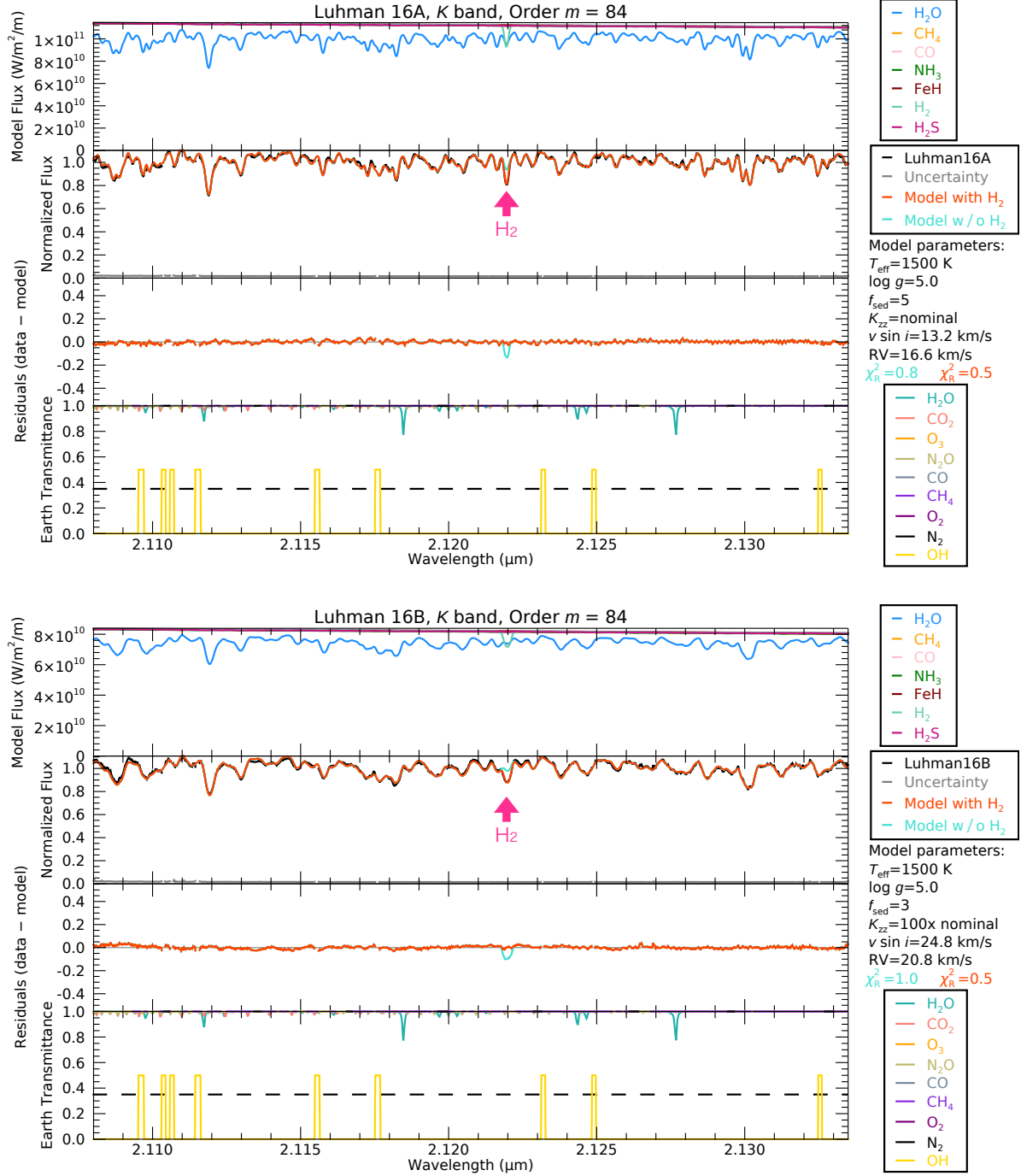


Figure 14. Detection of the H_2 2.1218 μm quadrupole line in the spectra of Luhman 16A (top set of four panels) and 16B (bottom set of four panels). The top panel of each set of four shows the contribution of each molecular species to the model, which indicates that this spectral region is shaped mostly by H_2O absorption features. The IGRINS spectrum and its best-fit models with and without H_2 line opacity are plotted in the second panel from the top. Their differences (data - model) are plotted in the third panel from the top. The differences show a clearly visible residual at the H_2 wavelength. The bottom panel shows the PSG Earth's transmittance to help assess the telluric lines in our spectra. The positions of OH emission lines are indicated with the yellow boxes, although box height is not proportional to line strength. The horizontal dashed line indicates the 35 percent transmittance threshold used to mask out the telluric-affected region (see Section 2.2), although no such contamination is found in this echelle order. The physical parameters of the best-fit model for each order are written in the margins between the legend boxes on the right side of the panels.

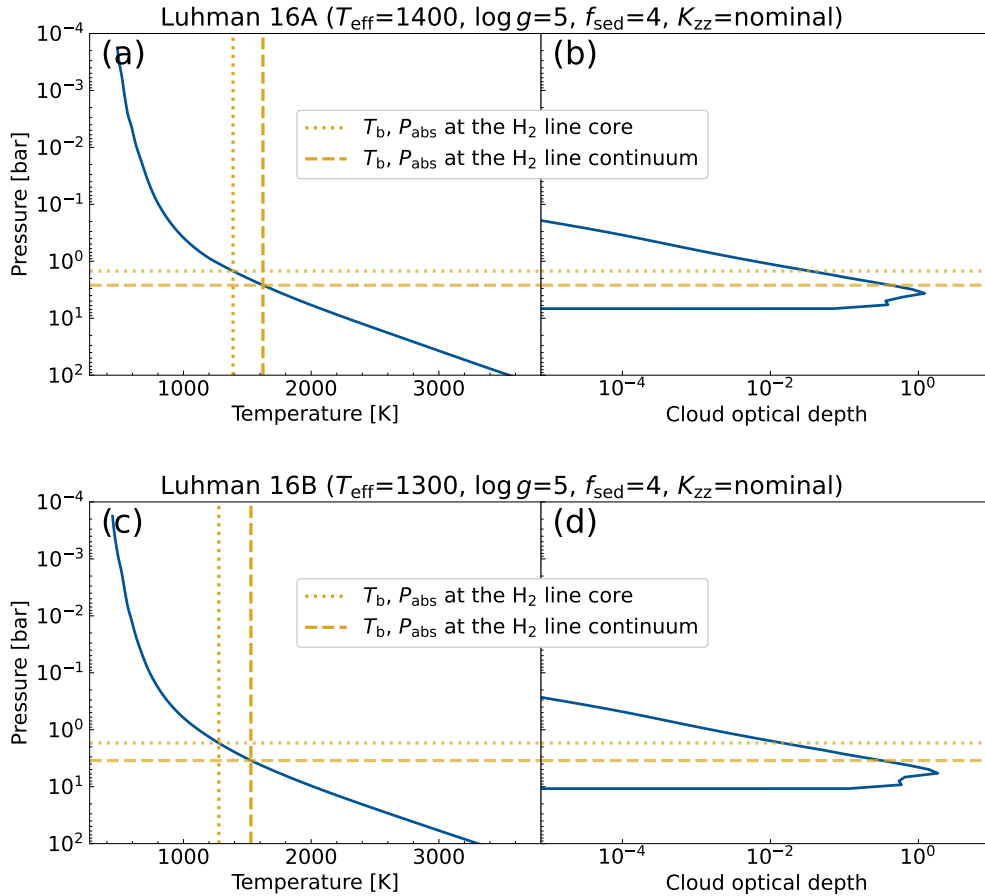


Figure 15. Temperature-pressure (T - P) profiles (panels a and c) and cloud optical depth (panels b and d) for Luhman 16A (top) and B (bottom) in the global best-fit atmospheric models. The yellow vertical dotted and dashed lines in panels (a) and (c) indicate the brightness temperatures (T_b) corresponding to the 2.1218 μm centre of the H_2 line and the nearby pseudo-continuum, respectively. The horizontal dotted and dashed yellow lines indicate the pressure at which the T - P profile and the corresponding vertical lines intersect. The cloud optical depth peaks at a comparable or higher pressure than the pressure of the absorbing layer corresponding to the centre of the H_2 line, consistent with our inference of a cloud-free upper atmosphere, from which we detect H_2 absorption.

Table 3. Detected HF lines

Order m	Wavelength (μm)	Notes
72	2.4759	
72	2.4556	
72	2.4538	
73	2.4331	overlapped by a telluric mask
74	2.4138	unclear as this is on the order edge
74	2.3958	
75	2.3791	
75	2.3636	
76	2.3494	detected only in Luhman 16A
76	2.3365	

that we see them in both components of Luhman 16. HF is thus detectable over a range of substellar temperatures and into at least early T dwarfs. Table 3 lists the detected HF lines and Figure 18 shows the clearest examples. These HF lines are not detected in the T6 spectrum in Tann22 because the CH_4 opacity is much larger and obscures contributions from most other species in this wavelength region.

4.3 Unidentified features

While the spectra of both binary components were well reproduced by the model, the high SNR and high wavelength resolution of our data revealed several discrepancies with the best-fit model photospheres. Compiling them could help recognize new absorbing species not included in the current model or identify incompleteness in the molecular line lists (e.g., as in Tann22).

Following Tann22, we adopted two criteria to identify discrepancies between the model and data. For the first criterion, we calculated the standard deviation (σ) of the residuals (data – model) for each order and selected regions where the residuals exceed 3σ for more than five consecutive data points. For the second criterion, we used matched filtering with a line profile kernel. The kernel consists of the instrumental broadening and rotational broadening profiles. The wavelength-dependent IPs at H and K were as determined in Section 3.1: we used Gaussian with the FWHM given by Equations 1 and 2. For the $v \sin i$ of rotation broadening, we adopted the global best-fit values for each object in Table 2. We convolved the (data – model) residual spectra with the line profile kernel to obtain filtered residuals. We selected spectral regions where the square of the filtered residuals exceeded 3σ . The regions selected by both of these criteria were further examined for potential unidentified features.

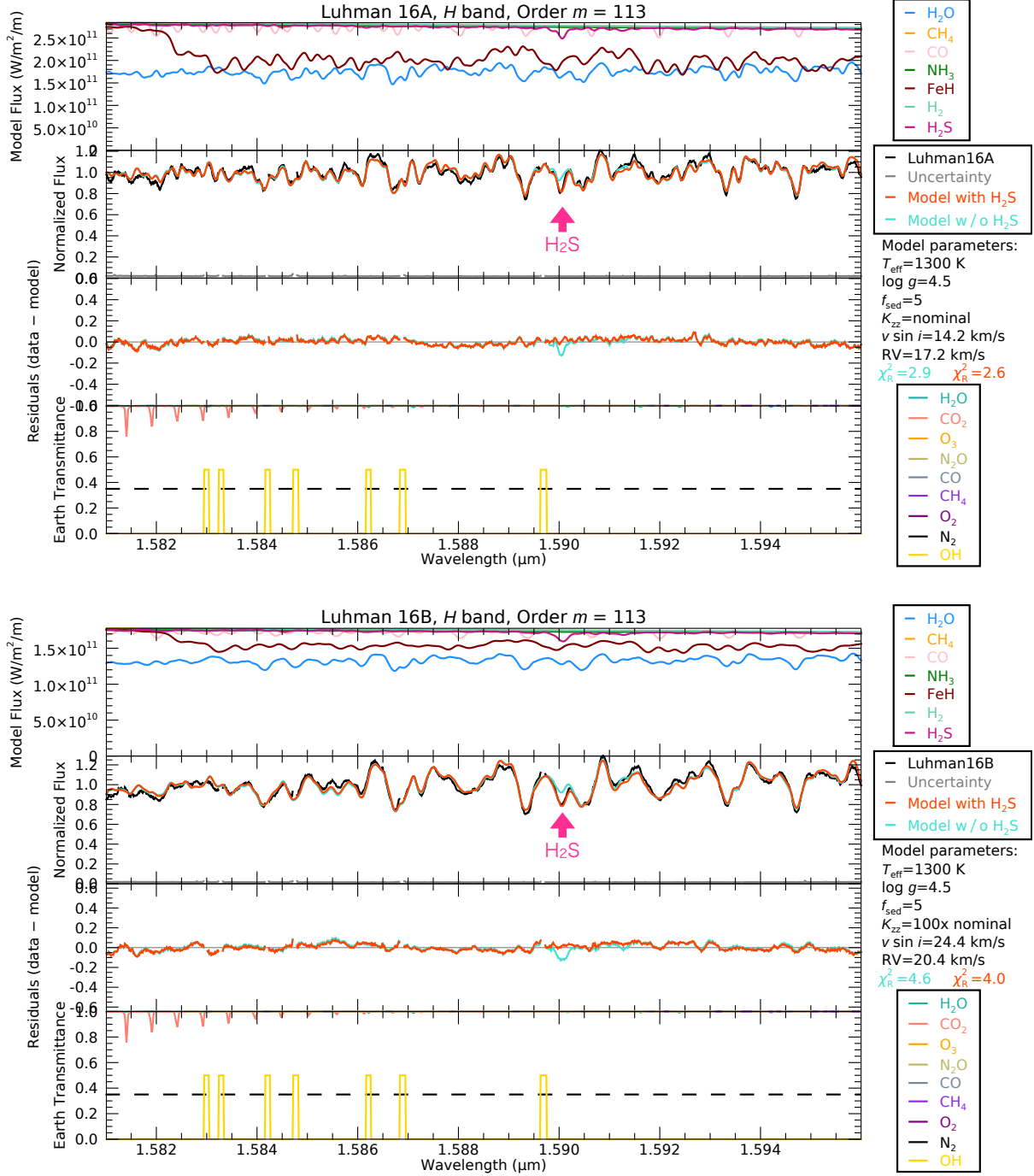


Figure 16. Detection of the H_2S 1.5900 μm line in IGRINS order $m = 113$ the spectra of Luhman 16A (top set of four panels) and 16B (bottom set of four panels). The layout is the same as in Figure 14.

The quadratic fit of the data to the continuum in the reduction process (Section 2.2) can produce unintended deviations in about 1 nm ranges at each edge of an IGRINS order. Candidate unidentified features detected in these edge regions were checked against the adjacent order to eliminate false detections.

With the availability of two simultaneously observed spectra of similar objects, and the previously published T6 spectrum in Tann22, we adopted a third criterion for confirming candidate unidentified features. Features that appear in the residuals in at least two, or in all

three of the objects, are highly likely to be of astrophysical origin. In all cases, we find that their widths match the rotational widths of other spectroscopic features in the respective objects.

We list and explore the unidentified regions in Sections 4.3.1–4.3.3. Features detected in both or either of Luhman 16A and B are summarized in Table 4 and their presence in the T6 dwarf spectra of Tann22 is added in the fifth column. Even if a feature met the first two criteria in only Luhman 16A, it was deemed to be detected in both objects when it met the criteria for Luhman 16B using 1σ cutoff

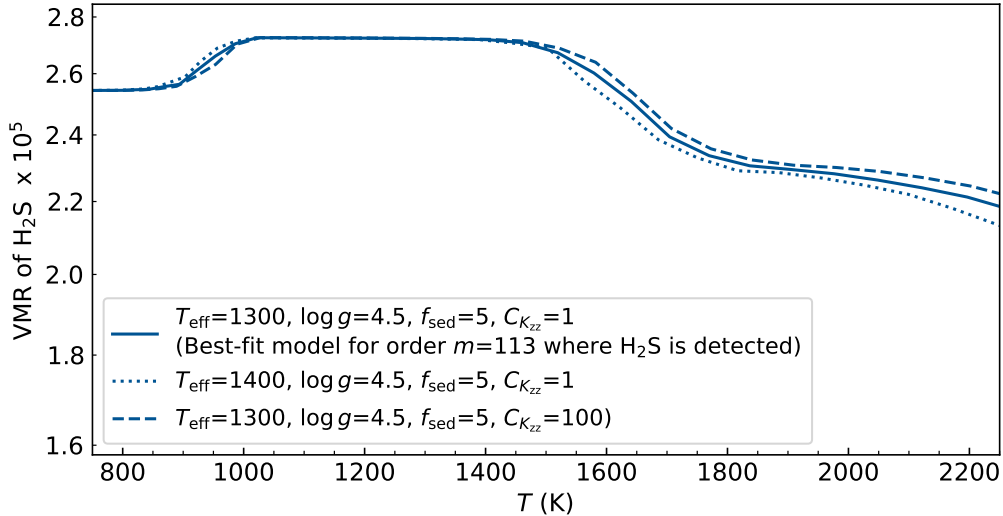


Figure 17. Dependence of the H_2S VMR (solid line) on temperatures in Luhman 16A based on the best-fit model atmosphere for order $m = 113$, where the H_2S line is detected. The y-axis is on a logarithmic scale. The VMR changes only by a factor of 1.2 between 1000 and 2000 K, throughout the photosphere. The dotted and dashed lines show that this is also the case for models with different T_{eff} and K_{zz} , respectively. This illustrates that the strength of the H_2S line is sensitive mostly to the S abundance, and not to temperature or disequilibrium effects.

instead of 3σ on account of the faster rotation of Luhman 16B that further smeared features.

In the T6 spectra in Tann22, the pseudo-continuum over 1.60–1.73 μm and 2.10–2.48 μm is dominated by CH_4 absorption, unlike in our targets. No common unidentified features are detected at all in these wavelength ranges, as any Luhman 16AB features are likely obscured by CH_4 in the T6 dwarf. On the other hand, most of the unidentified features detected at these wavelengths by Tann22 are not detected in our targets, suggesting that they may be attributed to inaccuracies in the CH_4 line list.

4.3.1 Absorption-like features

The most numerous of the newly detected features are those that appear as absorption (i.e., troughs) in the (data – model) residuals, as noted in Table 4. We show an example of such regions in Figure 19 with the vertical dashed line indicating the region of interest. This feature is found in the same wavelength position in all three objects including the T6 dwarf analysed in Tann22.

We searched for spectral lines that matched the wavelengths of these features using the line lists from the compilation of the ExoMol database (Tennyson et al. 2016) or the Vienna Atomic Line Database (VALD; Kupka et al. 1999, Ryabchikova et al. 2015). Specifically, we checked for absorption by H_2O , H_2 , CO, or CH_4 isotopologues, OH, CH, NH, C_2 , MgH, NaH, CaH, PH_3 , C_2H_2 , H_2^+ , HeH^+ , H_3^+ , OH^+ , and CH^+ . We did not find any matches among the known lines. All of these unidentified features fall in wavelength regions dominated by water absorption, although in some cases there is also strong absorption by CO (Table 4). We therefore suspect that the unidentified absorption features are either new molecular lines or the result of slight inaccuracies in the wavelengths or strengths of known transitions of the water or possibly the CO molecule.

4.3.2 Emission-like features

An upward bump in the (data – model) residual at 1.52085 μm (Figure 20) is one of the most intriguing unidentified features. It is

the clearest emission-like feature without any other contaminating factors in the "Notes" column of Table 4, such as a potentially miss-estimated CO line absorption (e.g., 2.29338 μm), part of a P Cygni profile-like residual (e.g., 2.24378 μm ; Section 4.3.3), or remnants from telluric line contamination (e.g., 1.94519 μm). It is seen in the IGRINS spectra of all three objects, presented here and in Tann22. The fact that it appears broader in Luhman 16B than in 16A, like other stellar absorption lines, confirms that it is intrinsic in origin. An upward profile suggests that either an emission line was observed or that the model is overestimating absorption.

We found a FeH line from a $F^4\Delta - X^4\Delta$ electronic transition in the MoLLIST (Bernath 2020) recorded in the ExoMol database that matches this wavelength. However, there is no reason to think that FeH would exhibit an emission line as the rest of the nearby FeH lines are in absorption, if at all present (Section 4.2.3). Moreover, Tann22 reported a similar discrepancy at the same wavelength in the analysis of a T6 object, where the contribution of FeH should be even smaller. We therefore conclude that FeH is not the cause.

In this wavelength range the shape of the model spectrum is determined almost entirely by H_2O absorption (see panels of order $m = 118$ in Figures B1 and B2), so if the model's overestimation of water absorption is the cause, the feature would be attributed to an inaccuracy in the water line list.

4.3.3 P Cygni profile-like features in the residuals

A notable class of feature in several regions dominated by water is a P Cygni-like profile in the residuals, where a peak and a trough are found adjacent to each other. Figure 21 shows examples in a part of the K band and Figure 22 shows some in the H band. Most of them show bluer peaks and redder troughs in the residuals, although some exhibit the opposite pattern (e.g., 1.517 μm ; see Figure 22). They are always found in both components of Luhman 16 and also in the T6 dwarf of Tann22 in most cases.

Figures 21 and 22 highlight the strongest P Cygni-like residuals from the model photosphere subtraction. All such features that pass our 3σ threshold (Section 4.3) are listed in Table 4. However, many

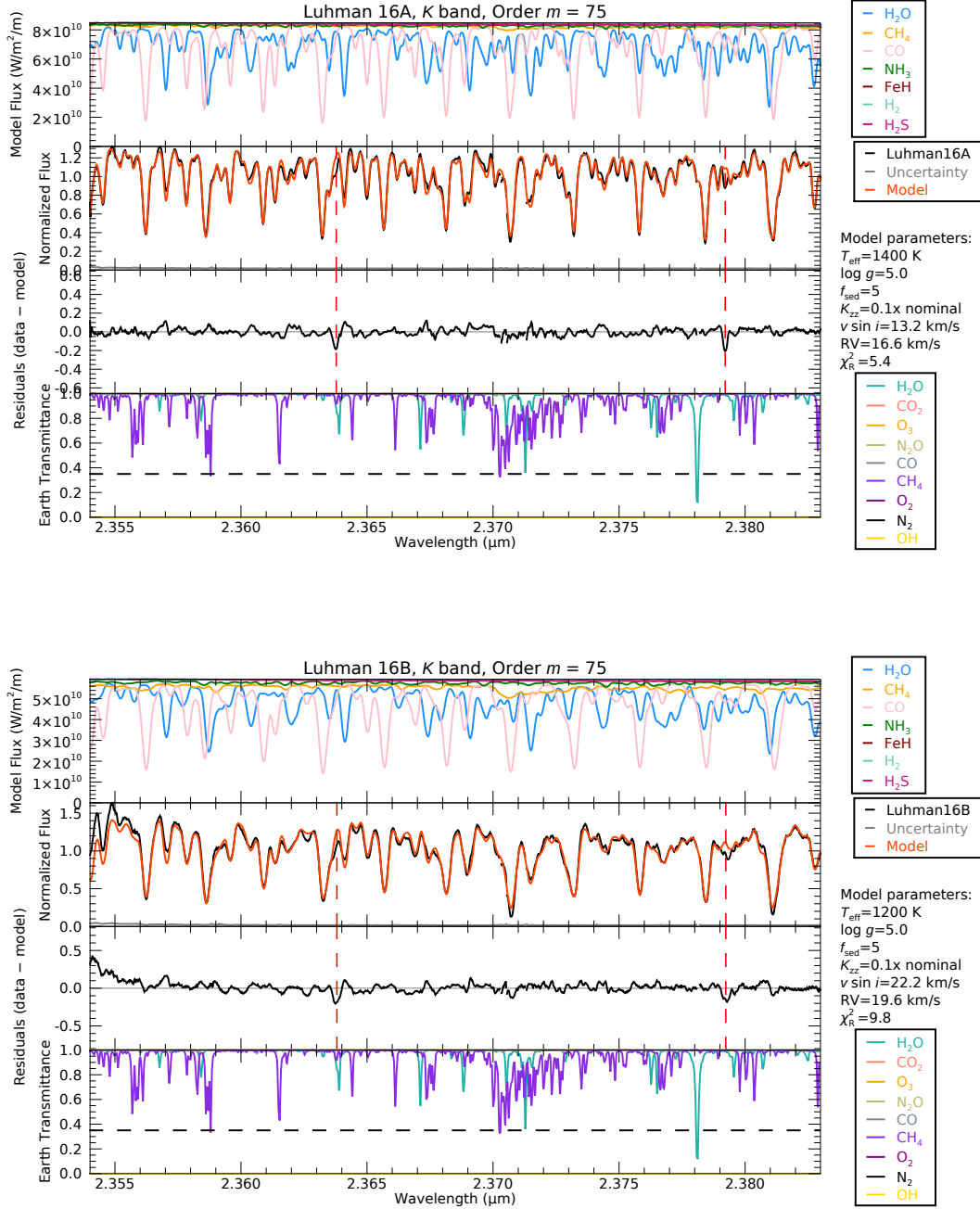


Figure 18. Example detections of HF lines at $2.3636 \mu\text{m}$ and $2.37905 \mu\text{m}$ in order $m = 75$ of both Luhman 16A (top four panels) and B (bottom four panels) spectra. The layout is the same as Figure 14. These are the most prominent examples, but we detect multiple HF lines in orders 72–76 (Table 3). Our models do not include HF opacity. The red vertical dashed lines indicate where the HF lines are predicted (Coxon & Hajigeorgiou 2015), coinciding with the positions of the noticeable dips in the residual plot (data – model).

more such features exist below the 3σ threshold. These features are ubiquitous in broad regions where H_2O sets the pseudo-continuum. It is often difficult to attribute them to any particular absorption line because they do not necessarily appear around prominent H_2O lines.

We tested the possibility that the P Cygni-like residuals are caused by isotopologues of water by plotting the spectra of three isotopologues in the top panels of Figures 21 and 22: $^1\text{H}_2^{16}\text{O}$ (Polyansky et al.

2018), $^1\text{H}^2\text{H}^{16}\text{O}$ (Voronin et al. 2010), and $^1\text{H}_2^{18}\text{O}$ (Polyansky et al. 2017). The plotted spectra were normalized to their respective averages because the actual isotopic ratios are unknown and our purpose is to check for correspondence among the isotopologue lines and the P Cygni-like residuals. Most residual features do not line up with the wavelengths where an isotopologue has a strong line. While in a few cases alignment exists, realistic isotopic ratios (e.g., on Earth, ^{18}O is

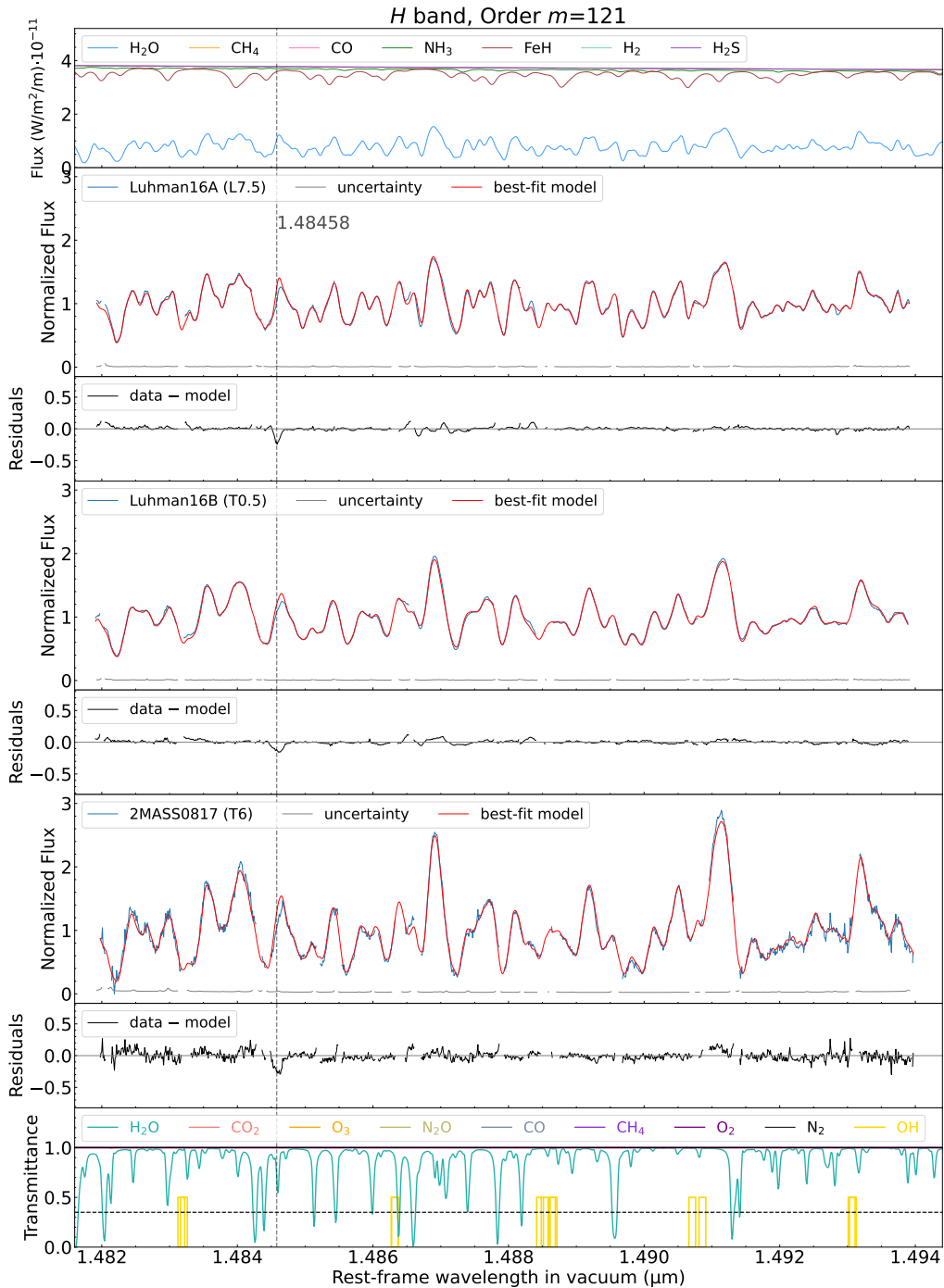


Figure 19. Example of a previously unidentified absorption feature in the spectra of Luhman 16A (L7.5), Luhman 16B (T0.5), and 2MASS J08173001–6155158 (T6; Tann22). The top panel shows the absorption contributions for individual molecular species and CIA for the global best-fit model to Luhman 16A. For each object, the upper panel shows the IGRINS spectrum and the best-fit photospheric model for this order, and the lower panel shows the residuals between them. The vertical dashed line indicates the position of the newly detected unidentified feature. The bottom panel shows the Earth’s transmittance to illustrate the masking of telluric-affected regions. The format is the same as the bottom panel of Figure 14.

about 0.2% of ^{16}O and ^2H is less than 0.02% of ^1H) dictate that the contributions from the minor isotopologues should be significantly lower than the main isotopologue $^1\text{H}_2^{16}\text{O}$, and so should not produce detectable residuals. We conclude that the contribution of the two minor water isotopologues is negligible and they do not cause the P Cygni-like residuals.

Instead, as a likely explanation, we suspect inaccuracies in the H_2O

line list. It is possible that absorption lines with specific quantum parameters share similar wavelength shifts, which could explain the consistent blue peak / red trough for the majority of the P Cygni-like residuals, but no further conclusions can be drawn in this study.

Table 4. Unidentified features: discrepancies between data and best-fit models.

Order <i>m</i>	Wavelength (μm)	Prominent Absorbers	Type of Feature	Detected in L7.5/T0.5/T6 [†] ?	Notes
73	2.44152	H ₂ O, CO	emission-like residual	Y/Y/N	
76	2.34465	H ₂ O, CO	absorption	Y/Y/N	
76	2.34201	H ₂ O, CO	absorption	Y/Y/N	
77	2.32392	H ₂ O, CO	emission-like residual	Y/Y/N	
77	2.32248	H ₂ O, CO	emission-like residual	Y/Y/N	
78	2.29393	H ₂ O, CO	absorption	Y/Y/N	CO bandhead
78	2.29338	H ₂ O, CO	emission-like residual	Y/Y/N	CO bandhead
79	2.25475	H ₂ O	emission-like residual	Y/N/N	
79	2.24378	H ₂ O	emission-like residual	Y/Y/N	might be a part of P Cygni-like residual [‡]
81	2.18466	H ₂ O	emission-like residual	Y/Y/N	confirmed in the adjacent order $m = 82$.
82	2.16681	H ₂ O	emission-like residual	Y/N/N	residual effect of telluric Br γ
83	2.14736	H ₂ O	absorption	Y/N/N	
85	2.09493	H ₂ O	P Cygni-like residual	Y/Y/Y	
85	2.08698	H ₂ O	P Cygni-like residual	Y/Y/Y	
85	2.08420	H ₂ O	absorption	Y/Y/N	confirmed in the adjacent order $m = 86$.
86	2.07405	H ₂ O	absorption	Y/N/N	
88	2.02351	H ₂ O	emission-like residual	Y/N/N	might be affected by a CO ₂ line in telluric standard stars
90	1.98139	H ₂ O	absorption	Y/Y/Y	
92	1.94519	H ₂ O	emission-like residual	Y/Y/N	might be affected by a hydrogen line in telluric standard stars
100	1.79740	H ₂ O	P Cygni-like residual	Y/Y/Y	confirmed in the adjacent order $m = 99$
100	1.78683	H ₂ O	P Cygni-like residual	Y/Y/Y	
100	1.78667	H ₂ O	P Cygni-like residual	Y/Y/Y	
101	1.78081	H ₂ O	absorption	Y/Y/N	
102	1.75665	H ₂ O	absorption	Y/Y/N	
102	1.75064	H ₂ O	emission-like residual	Y/N/N	
103	1.74238	H ₂ O	P Cygni-like residual	Y/Y/Y	
103	1.74223	H ₂ O	P Cygni-like residual	Y/Y/Y	
103	1.73535	H ₂ O	absorption	Y/N/N	
104	1.72719	H ₂ O	P Cygni-like residual	Y/Y/N	
106	1.69776	H ₂ O	absorption	Y/Y/N	
110	1.62739	H ₂ O	absorption	Y/N/N	
114	1.56890	H ₂ O	P Cygni-like residual	Y/Y/Y	
115	1.56397	H ₂ O, CO	P Cygni-like residual	Y/Y/Y	
115	1.56383	H ₂ O, CO	P Cygni-like residual	Y/Y/Y	
116	1.55114	H ₂ O	P Cygni-like residual	Y/Y/Y	
116	1.54166	H ₂ O	P Cygni-like residual	Y/Y/Y	
117	1.53842	H ₂ O	P Cygni-like residual	Y/Y/Y	
118	1.52595	H ₂ O	P Cygni-like residual	Y/Y/Y	
118	1.52085	H ₂ O	emission-like residual	Y/Y/Y	
119	1.51877	H ₂ O	absorption	Y/Y/N	barely verified in the adjacent order $m = 118$.
118	1.51700	H ₂ O	P Cygni-like residual	Y/Y/Y	confirmed in the adjacent order $m = 119$.
119	1.51689	H ₂ O	P Cygni-like residual	Y/Y/Y	
119	1.51700	H ₂ O	P Cygni-like residual	Y/Y/Y	
120	1.50227	H ₂ O	absorption	Y/Y/Y	
121	1.48459	H ₂ O	absorption	Y/Y/Y	

[†]T6 dwarf 2MASS J08173001–6155158 in Tann22.[‡]See Section 4.3.3 for discussion of all P Cygni profile-like residuals.

4.4 Disequilibrium chemistry

Our models incorporate disequilibrium, and as already seen for the best-fit models for Luhman 16A (Figure 6) and B (Figure 7), the $C_{K_{zz}}$ eddy diffusion coefficient parameter is around unity, although with an up to an order of magnitude scatter across the spectral orders. A clear example of the need for chemical disequilibrium is seen in the fitting of the 1.58–1.75 μm H -band orders, where FeH is expected to be an important absorber. The average of the best-fit photospheric models across all orders requires a moderate amount of

eddy diffusion ($\log C_{K_{zz}} = 0.1$). However, some of the H -band FeH orders are fit with a value two orders of magnitude higher, $\log C_{K_{zz}} = 2$, for both Luhman 16A and B. The effect of the disequilibrium here is to decrease the contribution of FeH through changes in the atmospheric temperature-pressure profiles, so that iron has rained out more at lower altitude and FeH is mostly undetectable (Figure 10, Section 4.2.3).

A more typical manifestation of disequilibrium chemistry at the L/T transition is stronger-than-expected CO absorption. Figure 23

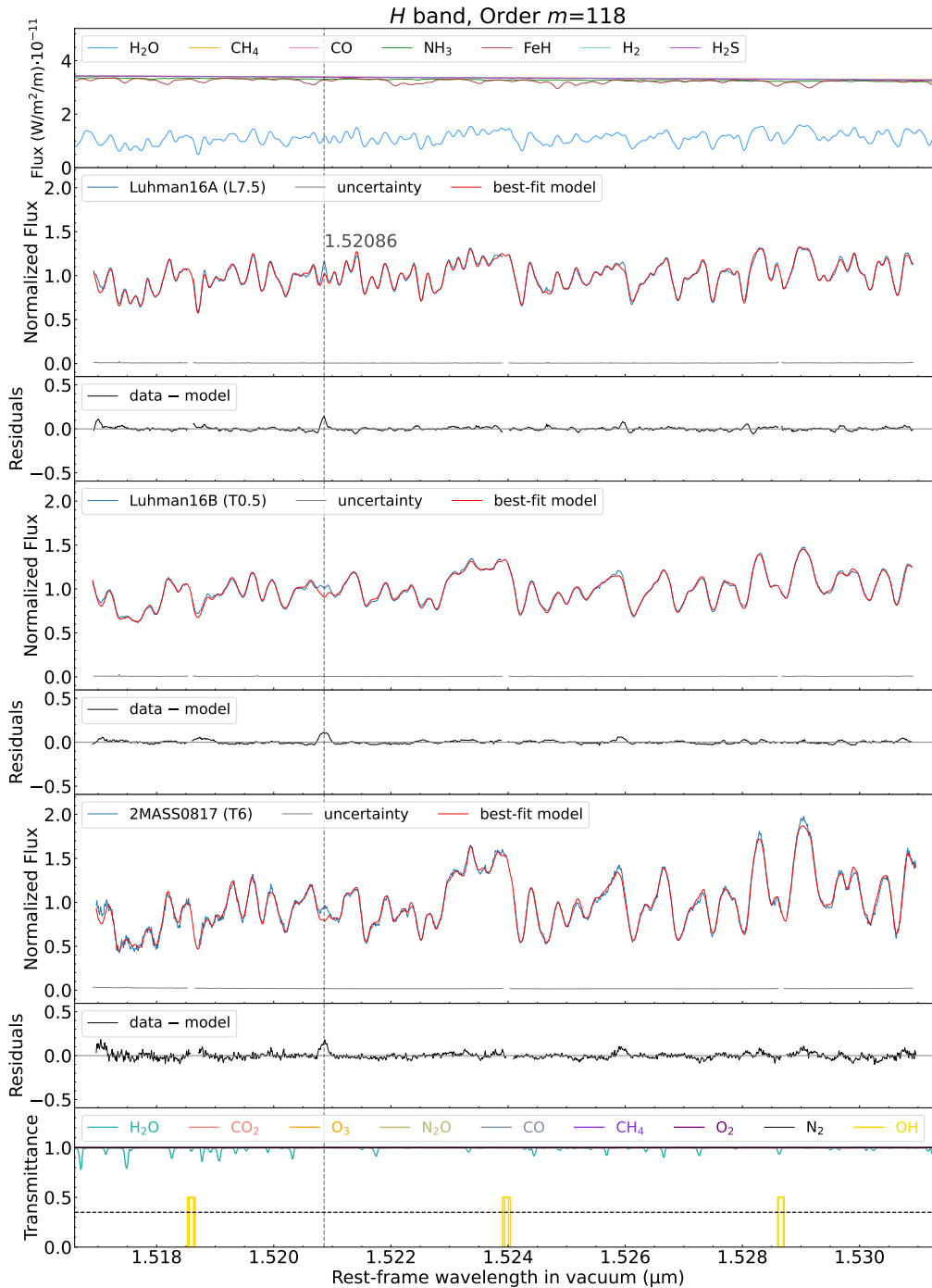


Figure 20. The clearest example of a previously unidentified emission-like feature—at 1.52085 μm —in the (data – model) residual spectra of Luhman 16A (L7.5), Lumhan 16B (T0.5), and 2MASS J08173001–6155158 (T6; Tann22). The figure format is the same as of Figure 19. As discussed in Section 4.3.2, this feature is possibly the result of over-estimated water line absorption in the atmospheric model.

demonstrates this by comparing best-fit models without and with disequilibrium chemistry for both L7.5 and T0.5 components of Luhman 16. The best-fit equilibrium models require an effective temperature that is too high ($T_{\text{eff}} = 1600$ K) and still underestimate the normalized depths of the CO lines. Their χ^2_{R} values are also significantly higher than for the disequilibrium model fits. Even if the $C_{K_{zz}}$ values of the best-fit models are in this case modest (0.1), the need for disequilibrium treatment is evident.

5 PLANET SEARCH

Our series of high-dispersion spectroscopic observations spans 70 days with a cadence as short as 0.15 days but most commonly 1 day. We use these to set upper limits on the RV variations due to unseen planets around either component.

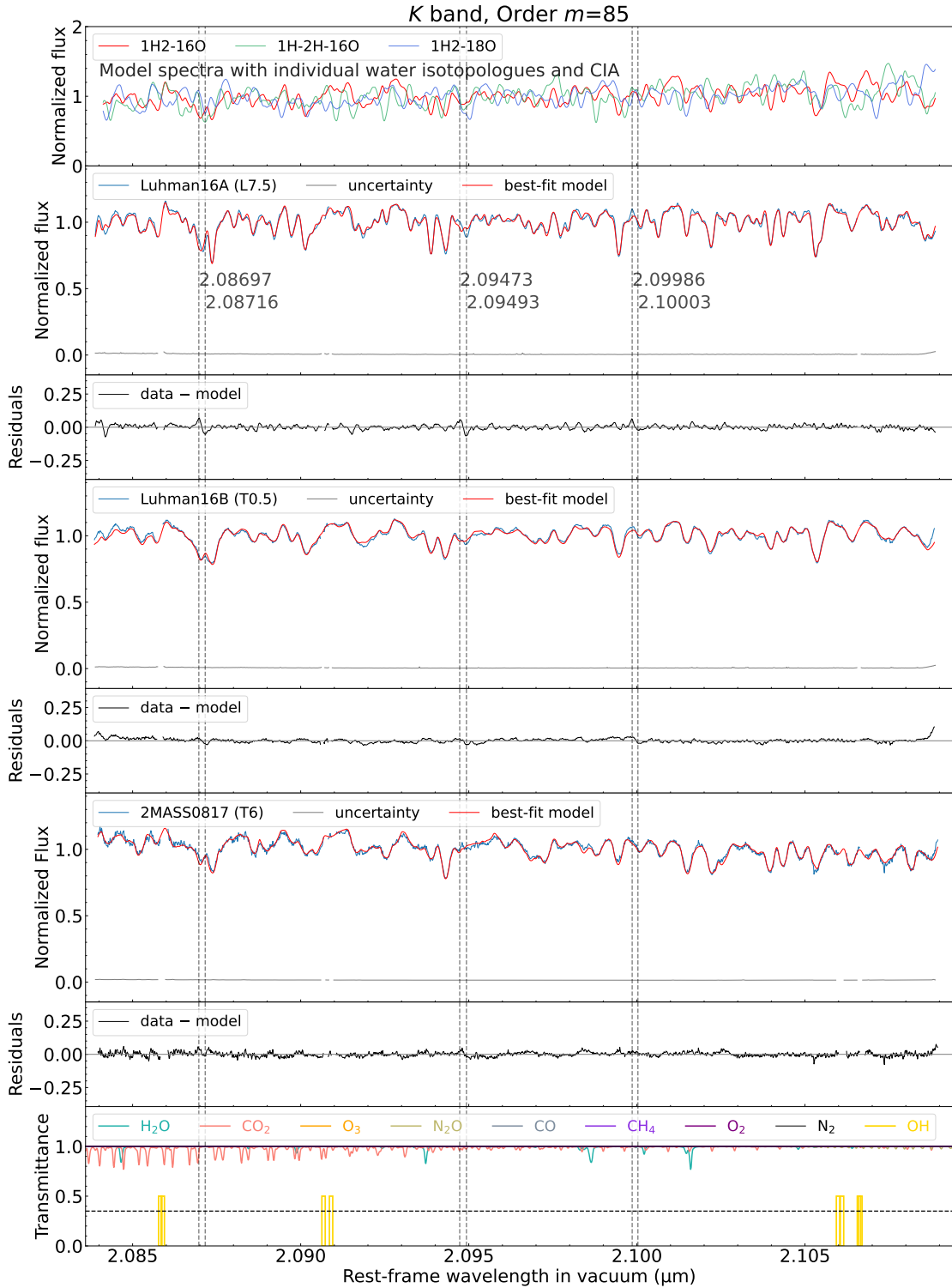


Figure 21. P Cygni-like features observed in the (data – model) residuals in the wavelength region dominated by H_2O absorption are indicated by vertical dashed lines. This is an example in order $m = 85$ in the K band. The top panel shows normalized model spectra of three water isotopologues ($^1\text{H}_2^{16}\text{O}$, $^1\text{H}^2\text{H}^{16}\text{O}$, $^1\text{H}_2^{18}\text{O}$), that also include CIA. The following six panels, in three pairs of two panels each, show the IGRINS spectra and their best-fit models for Luhman 16A, Luhman 16B, and 2MASS J08173001–6155158 (T6), respectively, and the (data – model) residuals. The residuals of the three objects show common P Cygni-like patterns at the same wavelengths. The bottom panel shows the Earth’s transmittance to see the effects of the masking of telluric-affected regions, as in Figure 19.

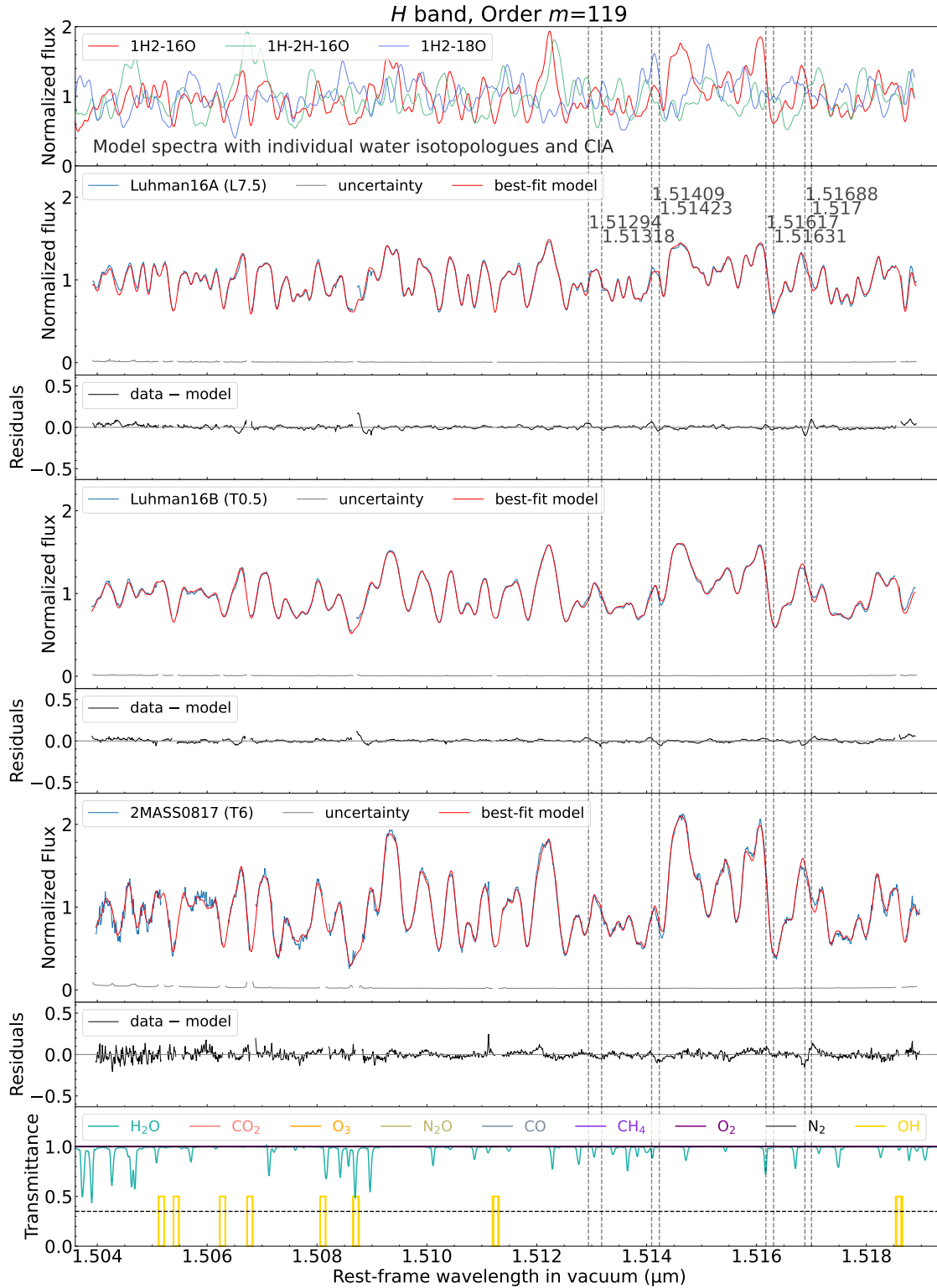


Figure 22. Same as Figure 21 but for order $m = 119$ in the H band. Most P Cygni-like residuals have bluer peaks and redder troughs, although an exception is seen around $1.517 \mu\text{m}$ here.

5.1 Radial velocity measurements

Precise RV measurements involve using a spectroscopic template as a reference spectrum to be shifted to the spectra at each epoch. We considered two different approaches to creating spectroscopic

templates. The first approach uses the high-SNR barycentric motion-corrected, combined spectrum of Luhman 16A or Luhman 16B as a self-reference template for itself at every epoch. The second approach uses the spectrum of Luhman 16A as a template for the spectrum of Luhman 16B. Since the spectra of the two components are observed at

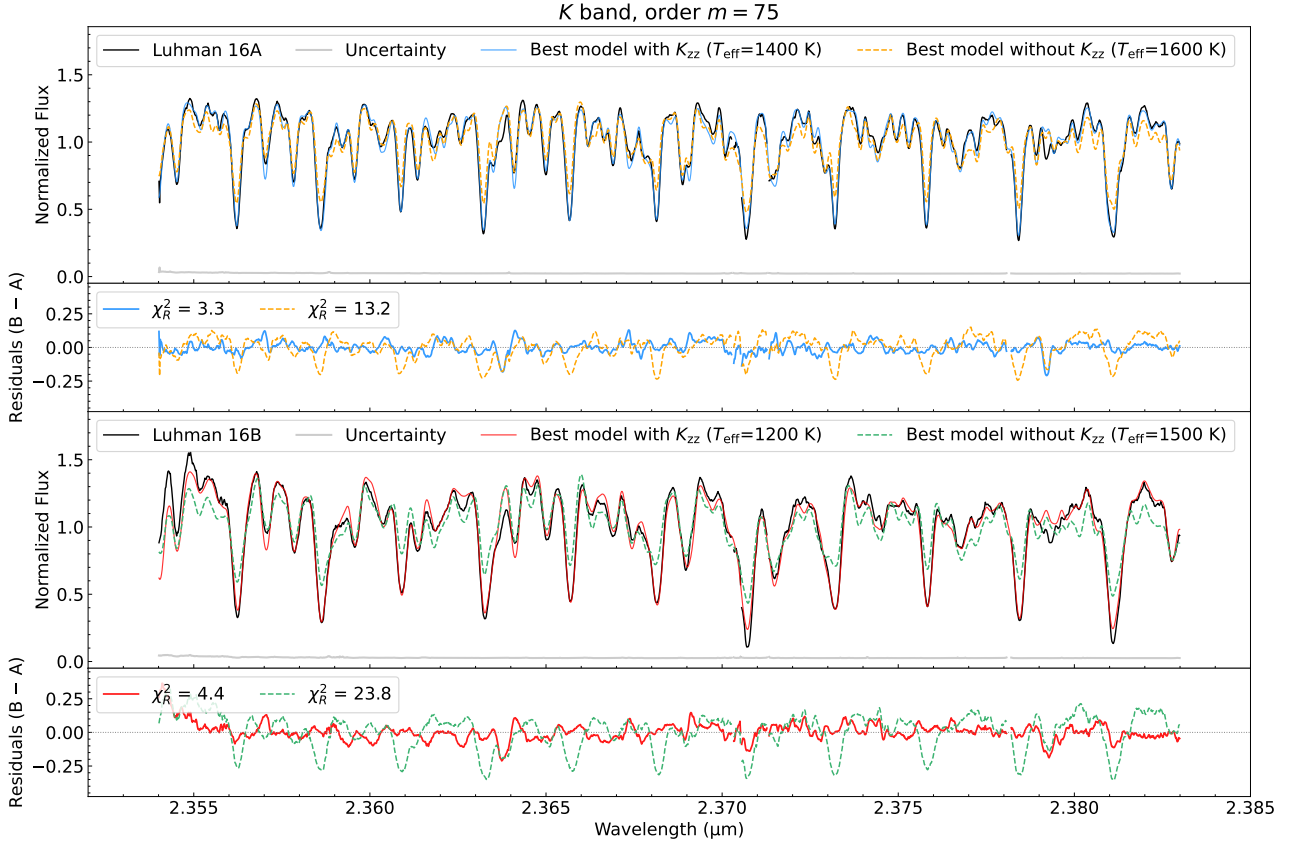


Figure 23. Comparison of the inclusion of vertical mixing as a cause for disequilibrium chemistry in a wavelength region where CO is the primary absorber (order $m = 75$). The top two panels show the spectral fitting and residuals for Luhman 16A and the bottom two for Luhman 16B. Models that incorporate vertical mixing (K_{zz} parameter) reproduce the data better.

the same time and under the same conditions and instrumental setup, the relative RVs are expected to be free from observational systematic effects. Because the spectral types of the components are similar, L7.5 and T0.5, either component is a good template for the other. Luhman 16A is the slower rotator and exhibits sharper absorption lines than B. Hence, we convolved the spectra of Luhman 16A with a rotational broadening kernel to match those of Luhman 16B. The value of the relative $v \sin i$ for the broadening kernel is fixed to 14.0 km s^{-1} , which was the average determined from the order-by-order matching of the combined spectra of the two components (Section 3.2).

We thus analyse three different RV series:

- (i) individual epochs of Luhman 16A velocity-shifted to match the high-SNR combined spectrum of Luhman 16A;
- (ii) individual epochs of Luhman 16B velocity-shifted to match the high-SNR combined spectrum of Luhman 16B;
- (iii) individual epochs of Luhman 16B velocity-shifted to the corresponding simultaneous Luhman 16A spectra.

For each of the three RV series, we detrended for possible activity-induced RV variations using the following procedure. We calculated a chromatic RV index (Zechmeister et al. 2018) as the slope of a linear fit to the RV values from each echelle order as a function of the natural logarithm of the central wavelength of each order (left panel in Figure 24). The RV series of some orders shows a correlation between RVs and chromatic indices at individual epochs (right panel in Figure 24). This indicates RV variation caused by weather-induced

phenomena such as surface spots rather than planetary companions. We removed this correlation by subtracting a linear fit to the RV values in each order and adding back the average. After detrending, we took a weighted average of RVs for all individual orders at each epoch to get an overall RV time series for later analysis.

The three order-averaged RV series are shown in Figure 25. The scatter of relative RVs as a function of time were consistent among the three approaches. However, the 0.80 km s^{-1} standard deviation of the case (iii) RV series is larger than the 0.55 km s^{-1} quadrature sum of those for cases (i) 0.27 km s^{-1} and (ii) 0.48 km s^{-1} . That is, systematic uncertainties arising from the intrinsic spectroscopic differences of these two similar but not identical objects have a greater effect on the RV than systematics arising from the observing or instrumental environment. Hence, the approach that our custom observations were intended to benefit from, namely measuring RVs using binary components observed simultaneously as mutual references to each other, is not necessarily advantageous.

5.2 Periodogram Analysis

We searched for periodic RV signals by computing the generalised Lomb-Scargle (GLS) periodograms (Zechmeister & Kürster 2009) for each binary component, and for the relative RVs of B with respect to A, for the period range 0.3–70 days. We also calculated the window function for our data, to avoid spurious signals arising from the sampling. The resulting power spectra are shown in Figure 26 with the horizontal lines marking False Alarm Probability (FAP) levels

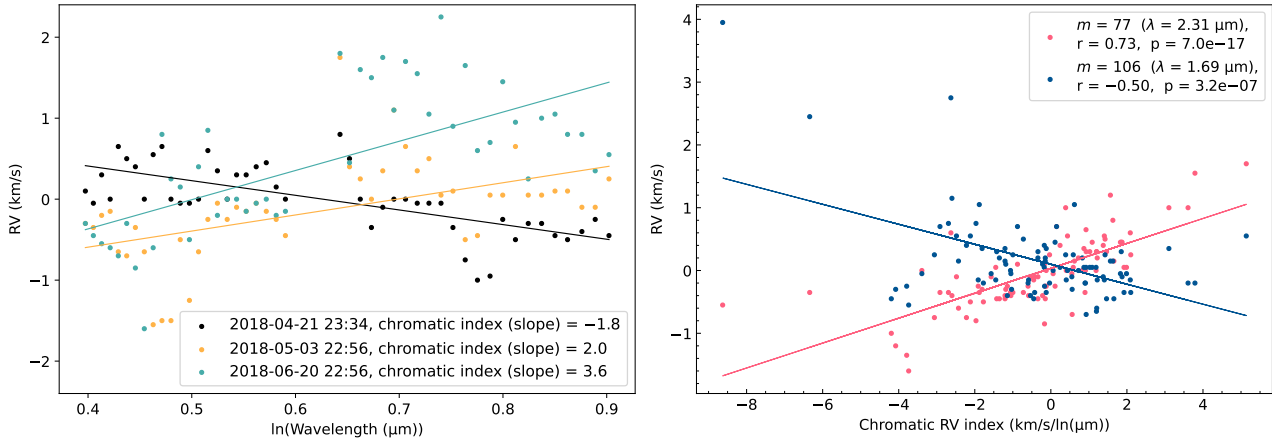


Figure 24. Examples of the derivation of the chromatic RV indices (left panel) and the correlation between these indices and RVs (right panel). The chromatic index is derived, for the entire *H*- and *K*-band spectrum at each epoch, as the slope of a straight line fitted to the RV as a function of the natural logarithm of wavelengths, following the definition in Zechmeister et al. (2018). The left panel shows examples of three different epochs for Luhman 16A. The solid lines represent linear fits to data points with the corresponding colours, and their slopes are the chromatic indices. The right panel exemplifies the correlation between the RVs of Luhman 16A and the chromatic indices in two different echelle orders, $m = 77$ and $m = 106$. The legend shows the Pearson correlation coefficient r with the associated p-value, which confirms the correlation between RV and chromatic index. The correlation indicates that the RV variability is due to surface inhomogeneities rather than a planetary companion.

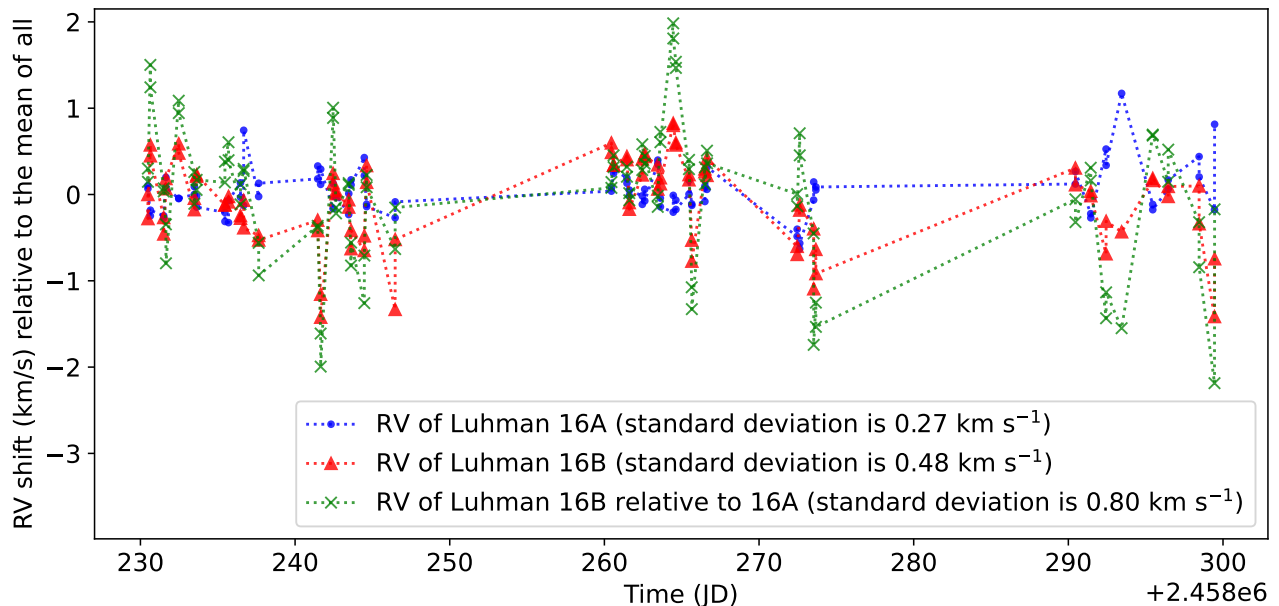


Figure 25. Time series of RV shifts relative to the mean of all data points for Luhman 16A and 16B as a function of time in Julian days. The blue circles and the red triangles indicate the RV series for each binary component with its own multi-epoch combined spectrum as a reference. The green crosses show the relative RV of Luhman 16B with respect to 16A, measured by shifting 16A’s broadened spectrum to match that of 16B at each epoch.

between 0.1–10%. The window function shows prominent peaks at 1 day and 0.5 days, corresponding to the most common spacing between the observations and its first overtone frequency. We do not identify any notable signals with FAP < 0.1% away from prominent peaks of the window function.

The highest periodogram peak that is distinct from a peak in the window function is found in the RV series of Luhman 16B: at 1.70 days (panels b and c in Figure 26). The phase-folded RV data for this period are shown in Figure 27. If this were caused by a real planet around Luhman 16B, the minimum mass is estimated to be 0.16 M_J with a semi-major axis of 0.008 au. Here we have adopted the mass

estimates for the individual binary components from Lazorenko & Sahlmann (2018): 33.5 M_J for Luhman 16A and 28.6 M_J for 16B.

Our RV analysis does not yield a significant planet detection. We discuss the detectability and upper limits on $M \sin i$ for potential planets in Section 5.3.

5.3 Constraints on planetary companions

To assess the limitations of our current data for detecting planets, we injected sinusoidal signals with periods 0.3–70 days and semi-amplitudes corresponding to planets with masses of 0.025–3.2 M_J

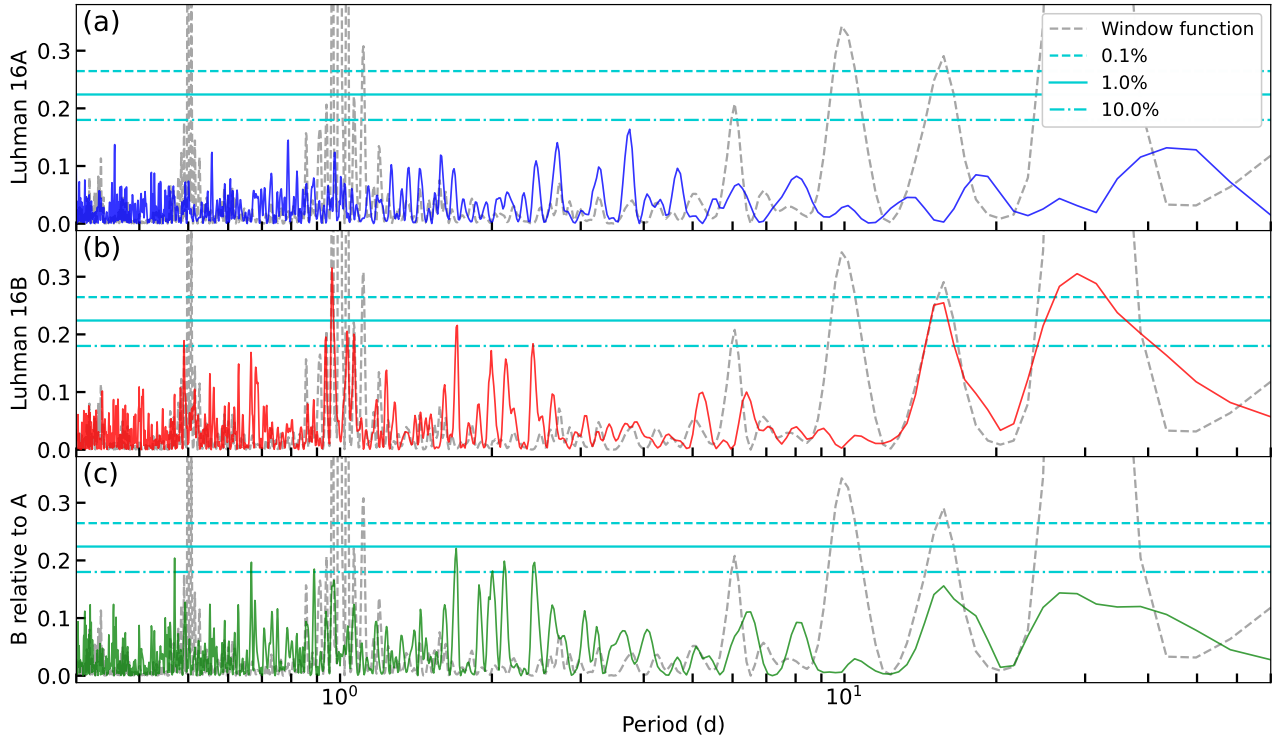


Figure 26. Generalized LS periodograms for the RV data points in Figure 25. From top to bottom, the panels depict the power spectrum of the RVs of Luhman 16A, that for Luhman 16B, and that for the relative RVs of Luhman 16B with respect to 16A. The dashed grey lines in all panels show the window function. The three horizontal lines indicate FAP levels from 0.1 to 10%.

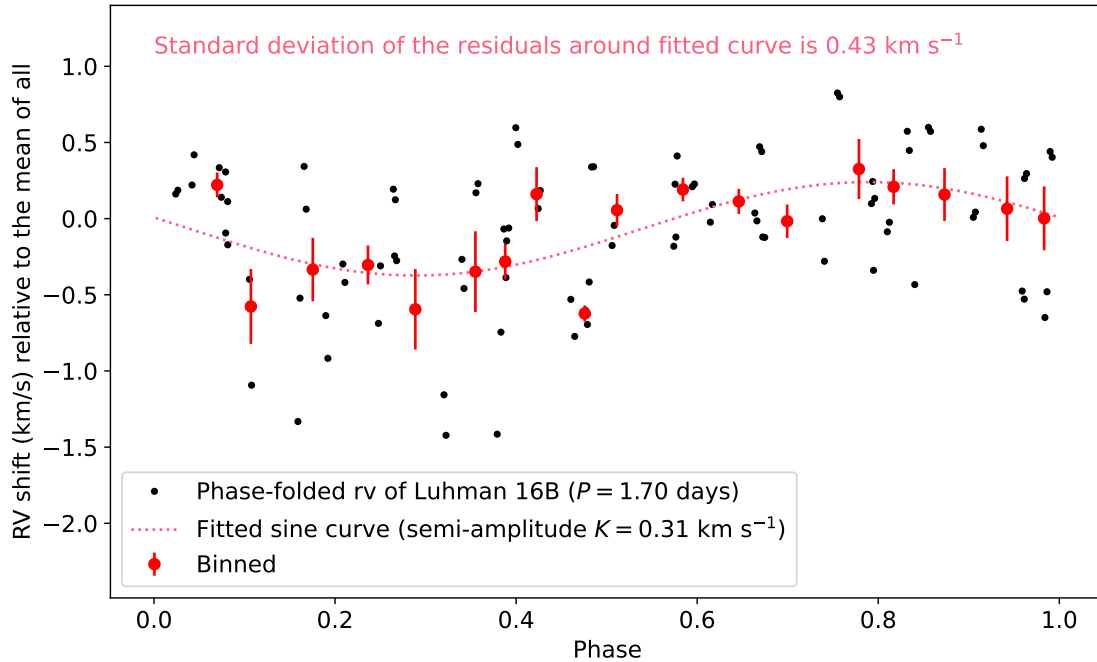


Figure 27. Time series of RVs of Luhman 16B folded on the 1.70-day period that corresponds to the highest peak (FAP = 1.7%) in the Luhman 16B periodogram (Figure 26, panel (b)). The black points represent the data from all 93 exposures, and the red points are the binning of every 5 data points. The dotted line is the best-fit sine curve. Its semi-amplitude is 0.31 km s^{-1} .

around each binary component, and performed the same periodogram analysis as in Section 5.2. We randomly sampled eccentricities from a Rayleigh distribution with $\sigma = 0.19$ (Sagear & Ballard 2023) and inclinations from a uniform distribution between $0-2\pi$. We deemed the injected signals to be recovered when the power at the injected period was above a FAP threshold of 0.1%. The detection efficiency was calculated at each grid point of periods and masses, as the fraction of injected signals that were successfully recovered in the periodogram. Figure 28 shows the results. Barring extremely unfavourable orbital inclinations, the data are sensitive to planets of masses above $\sim 0.2 M_J$ up to periods of 1 d and $\sim 0.4 M_J$ up to 10 d for Luhman 16A, and $\sim 0.3 M_J$ up to periods of 1 d and $\sim 0.7 M_J$ up to 10 d for Luhman 16B except for the period ranges affected by the window function. We rule out the presence of the planets in these parameter spaces, although planets that are smaller or on near-face-on orbits may still be hidden. Nevertheless, it should be noted that signals with <2 -day periods would have been under-sampled, given that our typical observation frequency is 1 day.

6 CONCLUSIONS

We have presented a comprehensive $1.48-2.48 \mu\text{m}$ $R = 28\,000$ spectroscopic atlas of the L7.5 and T0.5 components of the Luhman 16AB binary system: the closest pair of brown dwarfs to Earth. Our high-SNR combined spectra allow us to test the accuracy of photospheric models and their adopted line lists, to identify previously undetected molecules in L/T-transition dwarfs. Our 70-day-long spectroscopic campaign also enables us to place upper limits on the presence of planets around either component of the binary.

Our specific findings are:

- The Sonora Bobcat atmospheric models (Marley et al. 2021) can fit the high-dispersion $1.48-2.48 \mu\text{m}$ spectra of the L7.5 and T0.5 components sufficiently well, provided that they are augmented to include disequilibrium chemistry and clouds. We named this model family Sonora Bobcat Alternative B, iterating on the cloudless Sonora Bobcat Alternative A models discussed in Tannock et al. (2022).
- The well-established CO (HITEMP2019; Rothman et al. 2010; Li et al. 2015) and the updated CH₄ (Hargreaves et al. 2020) line lists match the high-dispersion spectra well. The H₂O line list from Polyansky et al. (2018) is noted as an improvement over previous H₂O line lists by Tann22. However, an ensemble comparison of the present data together with the spectrum of a T6 dwarf in Tann22 shows that wavelength discrepancies in the water lines remain, manifested as P Cygni-like profiles in the (data – model) residuals.
- FeH lines, while expected to be strong in the spectra of the two components under chemical equilibrium conditions, especially in the L7.5 component A, are not detected. Wavelength regions that should be affected by FeH favour lower- T_{eff} or higher- $C_{K_{zz}}$ models and more efficient iron rainout than models with the global best-fit parameters.
- We detected NH₃ lines in both Luhman 16A and B spectra, which makes them the warmest objects, along with the L9 dwarf DENIS J025503.3–470049, for which NH₃ is detected.
- We detected H₂ and H₂S absorption lines in L/T transition objects for the first time, following similar detections of both molecules in a T6 dwarf by Tann22 and reports of tentative or significant H₂S detections in a T9 dwarf (Hood et al. 2023) or in a Y dwarf (Lew et al. 2024). Such detections have been challenging in low-dispersion data because of contamination from other strong molecular bands—mainly H₂O or CH₄—despite the significant abundance of H₂ and H₂S.

- The detection of H₂—to date only with IGRINS—is a testament to the exquisite sensitivity attainable in the near-infrared at high spectral resolution with IGRINS on bright brown dwarfs. We employ the H₂ column density measurement to set a lower limit on the atmospheric pressure of the cloud deck. We conclude that the clouds in Luhman 16A and B reside at pressure levels $P_{\text{abs}} \geq 3$ bar.

- H₂S is important as the primary sulfur reservoir in hydrogen/helium-dominated atmospheres and, in combination with CO and H₂O measurements (Polman et al. 2023), can be used to estimate the bulk sulfur abundance. This is relevant for informing models of planet formation and evolution.

- We detect HF lines in L/T transition objects for the first time, extending the regime in which HF has previously been detected: a young directly imaged super-Jupiter, young late M dwarfs and field L4–L5 brown dwarfs (González Picos et al. 2024; Zhang et al. 2024; Mulder et al. 2025).

- Our 70-day RV monitoring campaign of the Luhman 16 binary did not yield any significant planet detections. We rule out planets with $M \sin i > 0.2 M_J$ in <1 -day orbital periods $>0.4 M_J$ in <10 -day periods around Luhman 16A, and $M \sin i > 0.3 M_J$ in <1 -day orbital periods $>0.7 M_J$ in <10 -day periods around Luhman 16B.

ACKNOWLEDGEMENTS

We acknowledge the support of the Canadian Space Agency through the Flights and Fieldwork for the Advancement of Science and Technology (FAST) program (reference No. 21FAUWOB12) and the Natural Sciences and Engineering Research Council of Canada (NSERC) Discovery Grants program, RGPIN-2019-06822.

This paper contains data based on observations obtained at the international Gemini Observatory (Program ID GS-2018A-Q-304), a program of NSF’s NOIRLab, which is managed by the Association of Universities for Research in Astronomy (AURA) under a cooperative agreement with the National Science Foundation on behalf of the Gemini Observatory partnership: the National Science Foundation (United States), National Research Council (Canada), Agencia Nacional de Investigación y Desarrollo (Chile), Ministerio de Ciencia, Tecnología e Innovación (Argentina), Ministério da Ciência, Tecnologia, Inovações e Comunicações (Brazil), and Korea Astronomy and Space Science Institute (Republic of Korea).

This work used the Immersion Grating Infrared Spectrometer (IGRINS) that was developed under a collaboration between the University of Texas at Austin and the Korea Astronomy and Space Science Institute (KASI) with the financial support of the US National Science Foundation under grants AST-1229522 and AST-1702267, of the University of Texas at Austin, and of the Korean GMT Project of KASI. We thank the IGRINS team for their continued support throughout this project.

PAMP acknowledges the use of the grant RYC2021-031173-I funded by MCIN/AEI/10.13039/501100011033 and by the ‘European Union NextGenerationEU/PRTR’ as well as by the grant MDM-2017-0737. RK acknowledges partial support from ANID’s FONDECYT Regular grant #1240249 and ANID’s Millennium Science Initiative through grants ICN12 009 and AIM23-0001.

The authors declare no competing interests.

DATA AVAILABILITY

The raw IGRINS data for Luhman 16AB are available on the Gemini Archive under Program ID GS-2018A-Q-114. The data underlying

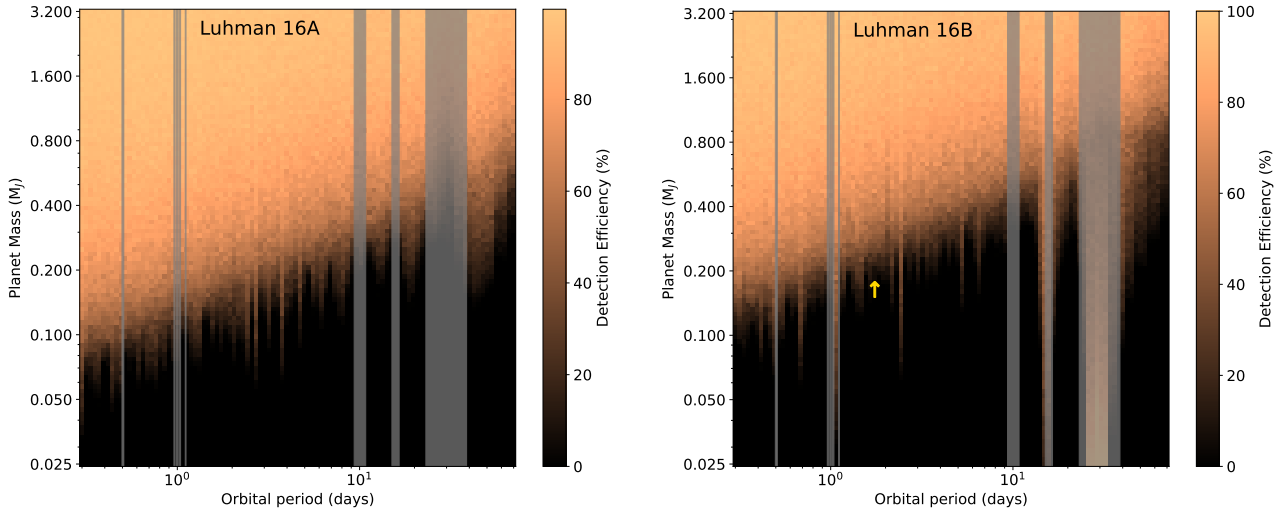


Figure 28. Detection efficiency as a function of orbital period and planet mass of potential planets around Luhman 16A (left panel) and B (right panel). The colour map represents the fraction of injected signals that were successfully recovered in the injection-recovery tests. The x axis shows the orbital period in days, while the y axis indicates the planet mass in Jupiter masses. The shades in grey indicate period ranges where the power of the window function is greater than the horizontal line indicating FAP=10% in Figure 26. The possible planet signal at $M \sin i = 0.16M_J$ and $P = 1.70$ days around Luhman 16B discussed in Section 5.2 is marked with a yellow upward arrow, indicating a lower limit of M . Regions in a bright colour indicate high detection efficiency, while darker regions signify lower efficiency. While shorter-period planets would be more readily evident in our data, any <2-day periods would be under-sampled by our ~ 1 -day observing cadence.

this article are available in [repository name, e.g. the Dryad Digital Repository], at [https://dx.doi.org/\[doi\]](https://dx.doi.org/[doi]) All reduced spectra and the best-fit Bobcat Alternative B model spectra, along with best-fit parameters for each order in Figures 6 and 7 and RV analysis results in Figures 24 and 25, are available as supplementary files, in Zenodo at <https://doi.org/10.5281/zenodo.15001024>, or in Harvard Dataverse at <https://doi.org/10.7910/DVN/TKY3KC>.

REFERENCES

- Ackerman A. S., Marley M. S., 2001, *ApJ*, **556**, 872
 Apai D., Nardiello D., Bedin L. R., 2021, *ApJ*, **906**, 64
 Atai A. A., Farziyev Z. S., 2021, *Azerbaijani Astronomical Journal*, **16**, 83
 Atai A. A., Yuzbashov E. R., Mikailov K. M., Farziyev Z. S., 2021, *Kinematics and Physics of Celestial Bodies*, **37**, 230
 Batalha N. M., 2014, *Proceedings of the National Academy of Science*, **111**, 12647
 Batalha N. E., Marley M. S., Lewis N. K., Fortney J. J., 2019, *ApJ*, **878**, 70
 Bedin L. R., Pourbaix D., Apai D., Burgasser A. J., Buenzli E., Boffin H. M. J., Libralato M., 2017, *MNRAS*, **470**, 1140
 Bedin L. R., Dietrich J., Burgasser A. J., Apai D., Libralato M., Griggio M., Fontanive C., Pourbaix D., 2024, *Astronomische Nachrichten*, **345**, e20230158
 Bernath P. F., 2020, *J. Quant. Spectrosc. Radiative Transfer*, **240**, 106687
 Biller B. A., et al., 2013, *ApJ*, **778**, L10
 Brock L., Barman T., Konopacky Q. M., Stone J. M., 2021, *ApJ*, **914**, 124
 Buenzli E., Saumon D., Marley M. S., Apai D., Radigan J., Bedin L. R., Reid I. N., Morley C. V., 2015, *ApJ*, **798**, 127
 Burgasser A. J., Marley M. S., Ackerman A. S., Saumon D., Lodders K., Dahn C. C., Harris H. C., Kirkpatrick J. D., 2002, *ApJ*, **571**, L151
 Burgasser A. J., et al., 2013a, *Mem. Soc. Astron. Italiana*, **84**, 1017
 Burgasser A. J., Sheppard S. S., Luhman K. L., 2013b, *ApJ*, **772**, 129
 Cardelli J. A., Clayton G. C., Mathis J. S., 1989, *ApJ*, **345**, 245
 Carlson B. E., Laci A. A., Rossow W. B., 1992, *ApJ*, **393**, 357
 Chen X., et al., 2024, *MNRAS*, **533**, 3114
 Coles P. A., Yurchenko S. N., Tennyson J., 2019, *MNRAS*, **490**, 4638
 Coxon J. A., Hajigeorgiou P. G., 2015, *J. Quant. Spectrosc. Radiative Transfer*, **151**, 133
 Crossfield I. J. M., 2023, *ApJ*, **952**, L18
 Crossfield I. J. M., et al., 2014, *Nature*, **505**, 654
 Cushing M. C., Rayner J. T., Davis S. P., Vacca W. D., 2003, *ApJ*, **582**, 1066
 Cushing M. C., et al., 2011, *ApJ*, **743**, 50
 Delorme P., et al., 2008, *A&A*, **482**, 961
 Faherty J. K., Beletsky Y., Burgasser A. J., Tinney C., Osip D. J., Filippazzo J. C., Simcoe R. A., 2014, *ApJ*, **790**, 90
 Filippazzo J. C., Rice E. L., Faherty J., Cruz K. L., Van Gordon M. M.,Looper D. L., 2015, *ApJ*, **810**, 158
 Fletcher L. N., de Pater I., Reach W. T., Wong M., Orton G. S., Irwin P. G. J., Gehr R. D., 2017, *Icarus*, **286**, 223
 Fuda N., Apai D., Nardiello D., Tan X., Karalidi T., Bedin L. R., 2024, *ApJ*, **965**, 182
 Gharib-Nezhad E., Iyer A. R., Line M. R., Freedman R. S., Marley M. S., Batalha N. E., 2021, *ApJS*, **254**, 34
 Gillon M., Triaud A. H. M. J., Jehin E., Delrez L., Opatom C., Magain P., Lendl M., Queloz D., 2013, *A&A*, **555**, L5
 González Picos D., et al., 2024, *A&A*, **689**, A212
 Gordon I. E., et al., 2022, *J. Quant. Spectrosc. Radiative Transfer*, **277**, 107949
 Gray D. F., 1992, *The observation and analysis of stellar photospheres*. Cambridge University Press
 Hargreaves R. J., Hinkle K. H., Bauschlicher Charles W. J., Wende S., Seifahrt A., Bernath P. F., 2010, *AJ*, **140**, 919
 Hargreaves R. J., Gordon I. E., Rey M., Nikitin A. V., Tyuterev V. G., Kochanov R. V., Rothman L. S., 2020, *ApJS*, **247**, 55
 Heinze A. N., Metchev S., Kurtev R., Gillon M., 2021, *ApJ*, **920**, 108
 Herzberg G., 1938, *ApJ*, **87**, 428
 Herzberg G., 1952, *ApJ*, **115**, 337
 Hood C. E., Fortney J. J., Line M. R., Faherty J. K., 2023, *ApJ*, **953**, 170
 Irwin P. G. J., Toledo D., Garland R., Teanby N. A., Fletcher L. N., Orton G. A., Bézard B., 2018, *Nature Astronomy*, **2**, 420
 Irwin P. G. J., Toledo D., Garland R., Teanby N. A., Fletcher L. N., Orton G. S., Bézard B., 2019, *Icarus*, **321**, 550
 Karalidi T., Apai D., Marley M. S., Buenzli E., 2016, *ApJ*, **825**, 90
 Karalidi T., Marley M., Fortney J. J., Morley C., Saumon D., Lupu R., Visscher C., Freedman R., 2021, *ApJ*, **923**, 269

- Kawahara H., Kawashima Y., Masuda K., Crossfield I. J. M., Pannier E., van den Bekerom D., 2022, *ApJS*, **258**, 31
- Kellogg K., Metchev S., Heinze A., Gagné J., Kurtev R., 2017, *ApJ*, **849**, 72
- Kniazev A. Y., et al., 2013, *ApJ*, **770**, 124
- Kupka F., Piskunov N., Ryabchikova T. A., Stempels H. C., Weiss W. W., 1999, *A&AS*, **138**, 119
- Lazorenko P. F., Sahlmann J., 2018, *A&A*, **618**, A111
- Lee J.-J., Gullikson K., Kaplan K., 2017, *igrins/plp* 2.2.0, doi:10.5281/zenodo.845059, <https://doi.org/10.5281/zenodo.845059>
- Lew B. W. P., et al., 2024, *AJ*, **167**, 237
- Li G., Gordon I. E., Rothman L. S., Tan Y., Hu S.-M., Kassi S., Campargue A., Medvedev E. S., 2015, *ApJS*, **216**, 15
- Lodieu N., Zapatero Osorio M. R., Rebolo R., Béjar V. J. S., Pavlenko Y., Pérez-Garrido A., 2015, *A&A*, **581**, A73
- Luhman K. L., 2013, *ApJ*, **767**, L1
- Mace G., et al., 2016, in Evans C. J., Simard L., Takami H., eds, Society of Photo-Optical Instrumentation Engineers (SPIE) Conference Series Vol. 9908, Ground-based and Airborne Instrumentation for Astronomy VI. p. 99080C, doi:10.1117/12.2232780
- Mace G., et al., 2018, in Evans C. J., Simard L., Takami H., eds, Society of Photo-Optical Instrumentation Engineers (SPIE) Conference Series Vol. 10702, Ground-based and Airborne Instrumentation for Astronomy VII. p. 107020Q, doi:10.1117/12.2312345
- Marley M. S., Saumon D., Goldblatt C., 2010, *ApJ*, **723**, L117
- Marley M. S., et al., 2021, *ApJ*, **920**, 85
- Melso N. D., Kaldon K. M., Luhman K. L., 2015, *AJ*, **150**, 62
- Morley C. V., et al., 2024, *ApJ*, **975**, 59
- Mukherjee S., Fortney J. J., Batalha N. E., Karalidi T., Marley M. S., Visscher C., Miles B. E., Skemer A. J. I., 2022, *ApJ*, **938**, 107
- Mukherjee S., Batalha N. E., Fortney J. J., Marley M. S., 2023, *ApJ*, **942**, 71
- Mukherjee S., et al., 2024, *ApJ*, **963**, 73
- Mulder W., et al., 2025, *A&A*, **694**, A164
- Park C., et al., 2014, in Ramsay S. K., McLean I. S., Takami H., eds, Society of Photo-Optical Instrumentation Engineers (SPIE) Conference Series Vol. 9147, Ground-based and Airborne Instrumentation for Astronomy V. p. 91471D, doi:10.1117/12.2056431
- Polman J., Waters L. B. F. M., Min M., Miguel Y., Khorshid N., 2023, *A&A*, **670**, A161
- Polyansky O. L., Kyuberis A. A., Lodi L., Tennyson J., Yurchenko S. N., Ovsyannikov R. I., Zobov N. F., 2017, *MNRAS*, **466**, 1363
- Polyansky O. L., Kyuberis A. A., Zobov N. F., Tennyson J., Yurchenko S. N., Lodi L., 2018, *MNRAS*, **480**, 2597
- Rooney C. M., Batalha N. E., Gao P., Marley M. S., 2022, *ApJ*, **925**, 33
- Rothman L. S., et al., 2010, *J. Quant. Spectrosc. Radiative Transfer*, **111**, 2139
- Rousselot P., Lidman C., Cuby J. G., Moreels G., Monnet G., 2000, *A&A*, **354**, 1134
- Ryabchikova T., Piskunov N., Kurucz R. L., Stempels H. C., Heiter U., Pakhomov Y., Barklem P. S., 2015, *Phys. Scr.*, **90**, 054005
- Sagear S., Ballard S., 2023, *Proceedings of the National Academy of Science*, **120**, e2217398120
- Saumon D., Marley M. S., 2008, *ApJ*, **689**, 1327
- Saumon D., Geballe T. R., Leggett S. K., Marley M. S., Freedman R. S., Lodders K., Fegley B. J., Sengupta S. K., 2000, *ApJ*, **541**, 374
- Sing D. K., et al., 2024, *Nature*
- Stahl A. G., et al., 2021, *AJ*, **161**, 283
- Stamnes K., Tsay S. C., Jayaweera K., Wiscombe W., Stamnes S., Jin Z., Lin Z., 2017, DISORT: DIScrete Ordinate Radiative Transfer, Astrophysics Source Code Library, record ascl:1708.006
- Tanaka W., 1966, *PASJ*, **18**, 339
- Tannock M. E., et al., 2021, *AJ*, **161**, 224
- Tannock M. E., Metchev S., Hood C. E., Mace G. N., Fortney J. J., Morley C. V., Jaffe D. T., Lupu R., 2022, *MNRAS*, **514**, 3160
- Tennyson J., et al., 2016, *Journal of Molecular Spectroscopy*, **327**, 73
- Tennyson J., et al., 2020, *J. Quant. Spectrosc. Radiative Transfer*, **255**, 107228
- Tsai S.-M., et al., 2023, *Nature*, **617**, 483
- Vacca W. D., Cushing M. C., Rayner J. T., 2003, *PASP*, **115**, 389
- Villanueva G. L., Smith M. D., Protopapa S., Faggi S., Mandell A. M., 2018, *J. Quant. Spectrosc. Radiative Transfer*, **217**, 86
- Visscher C., Lodders K., Fegley Bruce J., 2006, *ApJ*, **648**, 1181
- Visscher C., Lodders K., Fegley Bruce J., 2010, *ApJ*, **716**, 1060
- Voronin B. A., Tennyson J., Tolchenov R. N., Lugovskoy A. A., Yurchenko S. N., 2010, *MNRAS*, **402**, 492
- Yuk I.-S., et al., 2010, in McLean I. S., Ramsay S. K., Takami H., eds, Society of Photo-Optical Instrumentation Engineers (SPIE) Conference Series Vol. 7735, Ground-based and Airborne Instrumentation for Astronomy III. p. 77351M, doi:10.1117/12.856864
- Zechmeister M., Kürster M., 2009, *A&A*, **496**, 577
- Zechmeister M., et al., 2018, *A&A*, **609**, A12
- Zhang Y., et al., 2024, *AJ*, **168**, 246
- de Regt S., et al., 2024, *A&A*, **688**, A116

APPENDIX A: INFORMATION OF EACH EXPOSURE

Table A1 contains the details of each exposure during the 70-day observation.

Table A1: Gemini South/IGRINS Spectroscopic Observations of Luhman 16AB under Gemini program ID GS-2018A-Q-114 (PI: S. Metchev). The given SNR values are for the final, combined spectra. All exposure times are 300 s, except for the latter two exposures of 2018 05 26, which were 600 s each.

Date observed	Slit pos.	Target airmass	Telluric A0V standard	Luhman 16A		Luhman 16B		Julian day of mid-exposure
				<i>H</i> -band SNR (at 1.589 μm)	<i>K</i> -band SNR (at 2.101 μm)	<i>H</i> -band SNR (at 1.589 μm)	<i>K</i> -band SNR (at 2.101 μm)	
2018 04 21	A	1.17	HIP 41373	73	71	76	66	2458230.482323
2018 04 21	B	1.16	HIP 41373	76	74	79	70	2458230.486176
2018 04 21	A	1.17	HIP 55019	70	68	73	63	2458230.641519
2018 04 21	B	1.18	HIP 55019	64	61	67	56	2458230.645374
2018 04 22	A	1.13	HIP 61557	99	97	100	89	2458231.503751
2018 04 22	B	1.12	HIP 61557	105	101	105	93	2458231.507600
2018 04 22	A	1.18	HIP 52407	56	54	59	50	2458231.646716
2018 04 22	B	1.19	HIP 52407	74	73	79	72	2458231.650565
2018 04 23	A	1.17	HIP 53836	72	70	73	63	2458232.481006
2018 04 23	B	1.16	HIP 53836	77	76	77	68	2458232.481006
2018 04 24	A	1.15	HIP 53836	80	77	85	74	2458233.482268
2018 04 24	B	1.15	HIP 53836	82	78	86	75	2458233.486127
2018 04 24	A	1.17	HIP 79229	73	74	77	68	2458233.632515
2018 04 24	B	1.17	HIP 79229	77	77	81	71	2458233.636476
2018 04 26	A	1.18	HIP 53836	73	69	76	65	2458235.461515
2018 04 26	B	1.18	HIP 53836	74	71	77	67	2458235.465363
2018 04 26	A	1.40	HIP 53836	52	48	56	48	2458235.695114
2018 04 26	B	1.42	HIP 53836	60	55	66	55	2458235.698980
2018 04 27	A	1.16	HIP 53836	79	77	81	72	2458236.472315
2018 04 27	B	1.16	HIP 53836	82	79	83	74	2458236.472315
2018 04 27	A	1.31	HIP 53836	66	61	65	54	2458236.673351
2018 04 27	B	1.33	HIP 53836	72	66	60	55	2458236.677218
2018 04 28	A	1.22	HIP 53836	34	34	33	29	2458237.644928
2018 04 28	B	1.23	HIP 53836	23	22	22	17	2458237.648777
2018 05 02	A	1.15	HIP 53836	62	59	63	57	2458241.462518
2018 05 02	B	1.14	HIP 53836	66	65	70	63	2458241.466366
2018 05 02	A	1.28	HIP 53836	52	47	53	42	2458241.652099
2018 05 02	B	1.30	HIP 53836	49	44	50	39	2458241.655941
2018 05 03	A	1.16	HIP 53836	85	80	85	74	2458242.455635
2018 05 03	B	1.15	HIP 53836	84	79	85	74	2458242.459502
2018 05 03	A	1.26	HIP 53836	81	79	84	75	2458242.644415
2018 05 03	B	1.28	HIP 53836	79	78	82	73	2458242.648266
2018 05 04	A	1.13	HIP 53836	83	79	85	75	2458243.466576
2018 05 04	B	1.13	HIP 53836	84	80	87	76	2458243.470438
2018 05 04	A	1.19	HIP 53836	80	75	80	69	2458243.617409
2018 05 04	B	1.20	HIP 53836	88	82	91	78	2458243.621260
2018 05 05	A	1.12	HIP 53836	52	49	63	44	2458244.475526
2018 05 05	B	1.11	HIP 53836	60	57	61	52	2458244.479377
2018 05 05	A	1.22	HIP 53836	74	70	74	64	2458244.624893
2018 05 05	B	1.23	HIP 53836	72	68	72	62	2458244.628746
2018 05 07	A	1.12	HIP 53836	36	34	35	30	2458246.473160
2018 05 07	B	1.11	HIP 53836	40	38	40	33	2458246.473160
2018 05 21	A	1.10	HIP 53836	84	79	87	76	2458260.453650
2018 05 21	B	1.09	HIP 53836	86	82	88	78	2458260.457504
2018 05 21	A	1.27	HIP 53836	78	73	82	71	2458260.599531
2018 05 21	B	1.28	HIP 53836	73	67	74	64	2458260.599531
2018 05 22	A	1.09	HIP 53836	83	75	87	73	2458261.455328
2018 05 22	B	1.09	HIP 53836	80	74	84	71	2458261.459198
2018 05 22	A	1.32	HIP 53836	75	67	67	56	2458261.610750
2018 05 22	B	1.33	HIP 53836	75	67	67	56	2458261.610750
2018 05 23	A	1.10	HIP 53836	77	77	76	72	2458262.449235
2018 05 23	B	1.09	HIP 53836	68	71	67	65	2458262.453122
2018 05 23	A	1.33	HIP 53836	71	67	74	63	2458262.611687
2018 05 23	B	1.35	HIP 53836	78	72	82	69	2458262.611687

Table A1: Gemini South/IGRINS Spectroscopic Observations of Luhman 16AB under Gemini program ID GS-2018A-Q-114 (PI: S. Metchev). The given SNR values are for the final, combined spectra. All exposure times are 300 s, except for the latter two exposures of 2018 05 26, which were 600 s each.

Date observed	Slit pos.	Target airmass	Telluric A0V standard	Luhman 16A		Luhman 16B		Julian day of mid-exposure
				<i>H</i> -band SNR (at 1.589 μm)	<i>K</i> -band SNR (at 2.101 μm)	<i>H</i> -band SNR (at 1.589 μm)	<i>K</i> -band SNR (at 2.101 μm)	
2018 05 24	A	1.09	HIP 53836	92	83	96	81	2458263.454796
2018 05 24	B	1.09	HIP 53836	89	80	93	78	2458263.454796
2018 05 24	A	1.39	HIP 53836	78	74	82	70	2458263.618141
2018 05 24	B	1.41	HIP 53836	77	72	82	68	2458263.622030
2018 05 25	A	1.09	HIP 53836	76	73	77	67	2458264.454588
2018 05 25	B	1.09	HIP 53836	78	74	79	68	2458264.454588
2018 05 25	A	1.42	HIP 53836	68	63	70	57	2458264.621200
2018 05 25	B	1.44	HIP 53836	79	73	82	68	2458264.625079
2018 05 26	A	1.09	HIP 53836	72	69	76	66	2458265.469989
2018 05 26	B	1.09	HIP 53836	67	65	72	62	2458265.473883
2018 05 26	A	1.62	HIP 53836	74	63	77	57	2458265.655182
2018 05 26	B	1.68	HIP 53836	72	61	75	55	2458265.655182
2018 05 27	A	1.10	HIP 53836	59	55	59	50	2458266.498218
2018 05 27	B	1.11	HIP 53836	59	55	61	51	2458266.502085
2018 05 27	A	1.54	HIP 53836	54	48	52	41	2458266.634776
2018 05 27	B	1.56	HIP 53836	54	47	53	40	2458266.638647
2018 06 02	A	1.09	HIP 53836	39	39	42	36	2458272.463061
2018 06 02	B	1.09	HIP 53836	50	49	52	45	2458272.466923
2018 06 02	A	1.61	HIP 53836	47	44	49	39	2458272.628868
2018 06 02	B	1.64	HIP 53836	48	44	50	39	2458272.632761
2018 06 03	A	1.18	HIP 53836	56	51	57	47	2458273.530479
2018 06 03	B	1.19	HIP 53836	44	41	47	36	2458273.534409
2018 06 03	A	2.11	HIP 53836	45	41	50	39	2458273.673587
2018 06 03	B	2.16	HIP 53836	39	36	45	34	2458273.677470
2018 06 20	A	1.13	HIP 53836	41	36	41	32	2458290.455811
2018 06 20	B	1.13	HIP 53836	40	33	39	29	2458290.459661
2018 06 21	A	1.12	HIP 53836	62	59	67	57	2458291.447734
2018 06 21	B	1.13	HIP 53836	71	68	77	68	2458291.451685
2018 06 22	A	1.11	HIP 53836	43	39	45	39	2458292.443055
2018 06 22	B	1.12	HIP 53836	43	40	47	40	2458292.443055
2018 06 23	B	1.12	HIP 53836	29	27	33	27	2458293.444549
2018 06 25	A	1.15	HIP 53836	65	60	69	54	2458295.453290
2018 06 25	B	1.15	HIP 53836	72	66	78	63	2458295.457146
2018 06 26	A	1.15	HIP 53836	83	78	89	77	2458296.455378
2018 06 26	B	1.16	HIP 53836	84	78	90	76	2458296.459242
2018 06 28	A	1.16	HIP 53836	38	33	42	32	2458298.454360
2018 06 28	B	1.17	HIP 53836	37	34	42	33	2458298.458221
2018 06 29	A	1.16	HIP 53836	31	27	33	26	2458299.453755
2018 06 29	B	1.17	HIP 53836	46	35	35	21	2458299.456855

**APPENDIX B: THE 1.48–2.48 MICRON $R=28\,000$
SPECTRAL ATLAS AND BEST-FIT MODELS OF LUHMAN
16A AND B**

The high-SNR weighted-average-combined IGRINS spectrum and the best-fit model for all orders are presented in Figures [B1](#) for Luhman 16A and in Figures [B2](#) for Luhman 16B.

This paper has been typeset from a $\text{\TeX}/\text{\LaTeX}$ file prepared by the author.

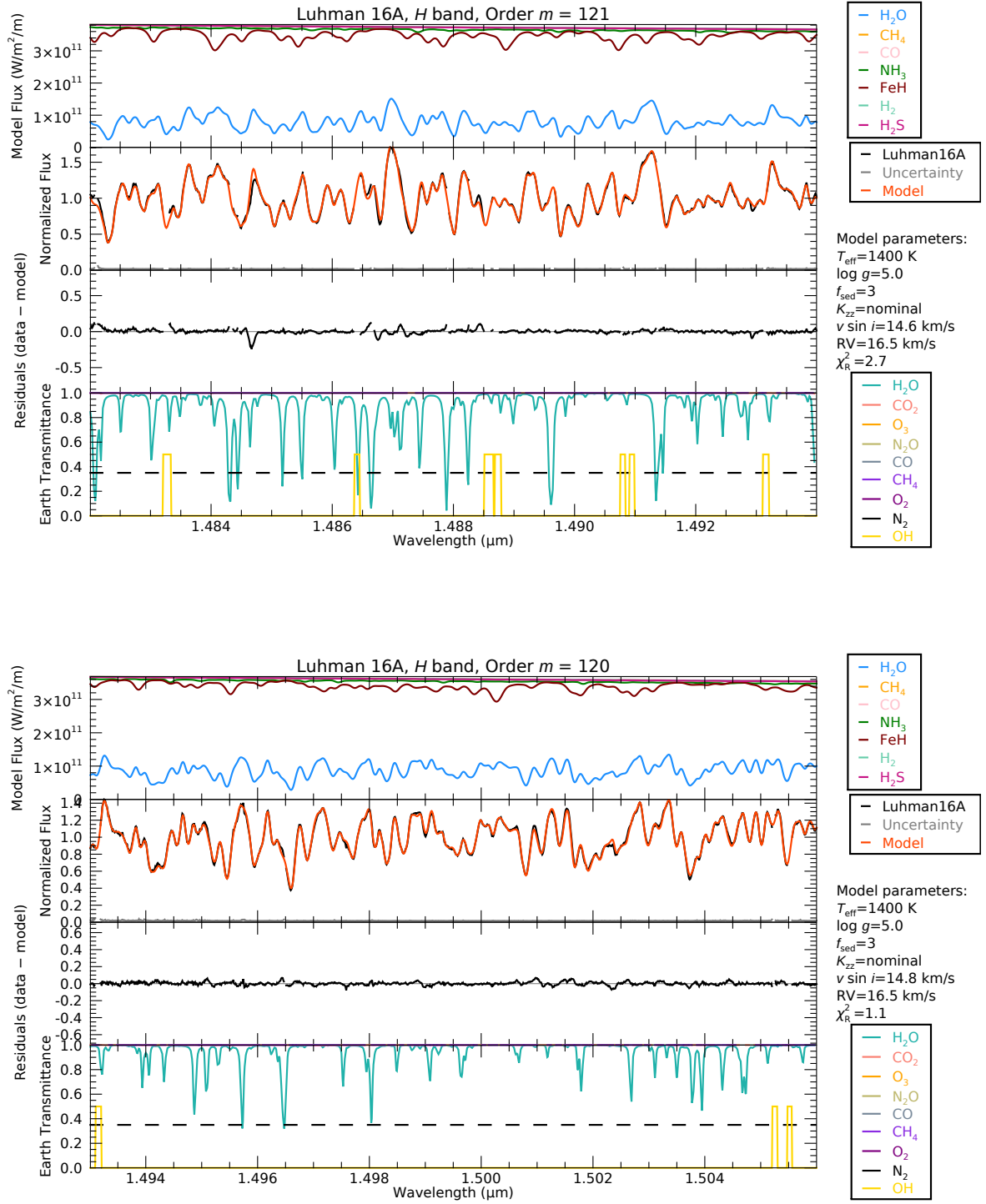


Figure B1. The spectral atlas of Luhman 16A over the full wavelength range of IGRINS from 1.48 to 2.48 μm . Each figure shows the spectrum in each echelle order. The physical parameters of the best-fit model for each order are written in the margins between the legend boxes on the right side of the panels. The top panel indicates the contribution of individual molecular species to the model spectrum (CIA is also included). They are calculated with the global best-fit parameters for the corresponding object, not the local best-fit parameters for that echelle order. The second panel from the top shows the IGRINS data with the best-fit Bobcat Alternative B model for the order. The third panel from the top shows the residuals (data - model) on the same y-axis scale as the panel above it. The bottom panel shows the PSG Earth's transmittance to help assess the telluric lines in our spectra. The positions of OH emission lines are shown as yellow boxes with wide boxes indicating blended OH lines. The box height is uniform, not indicating line strength. The horizontal dashed line indicates the 35 percent transmittance threshold used to select the telluric-affected region to mask (see Section 3.1). In the wavelength regions where detected or potential H_2 and H_2S absorption lines are present (e.g., orders $m = 84$ and 113), the two central panels include both cases where the models are with and without the line opacity of the molecule.

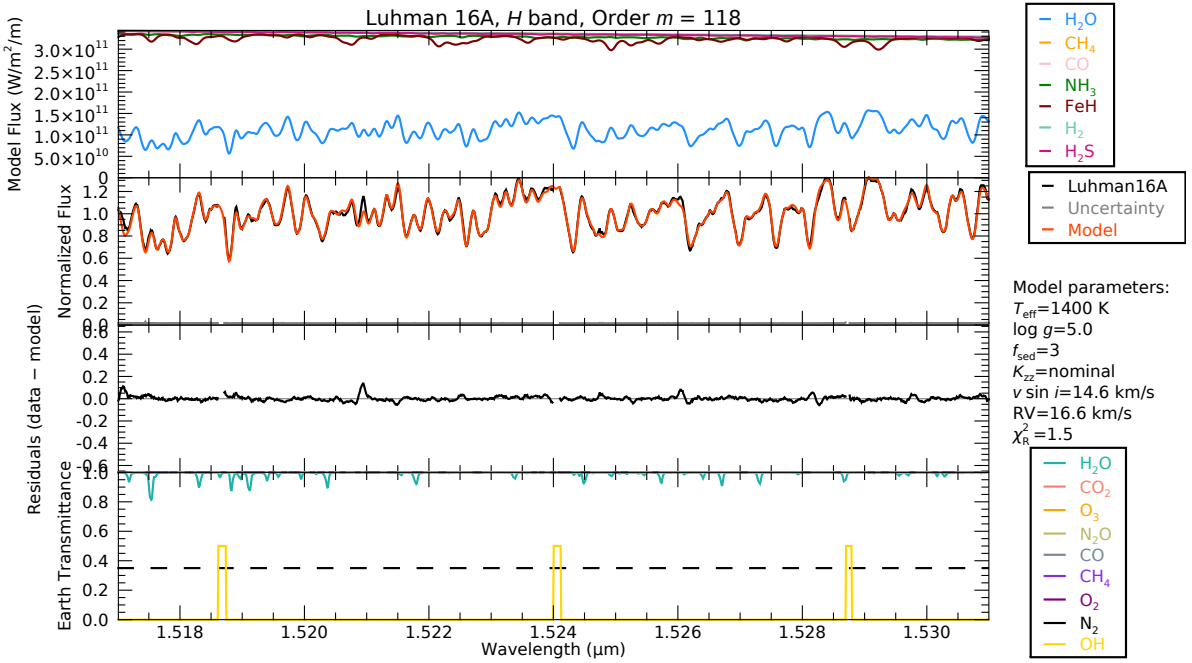
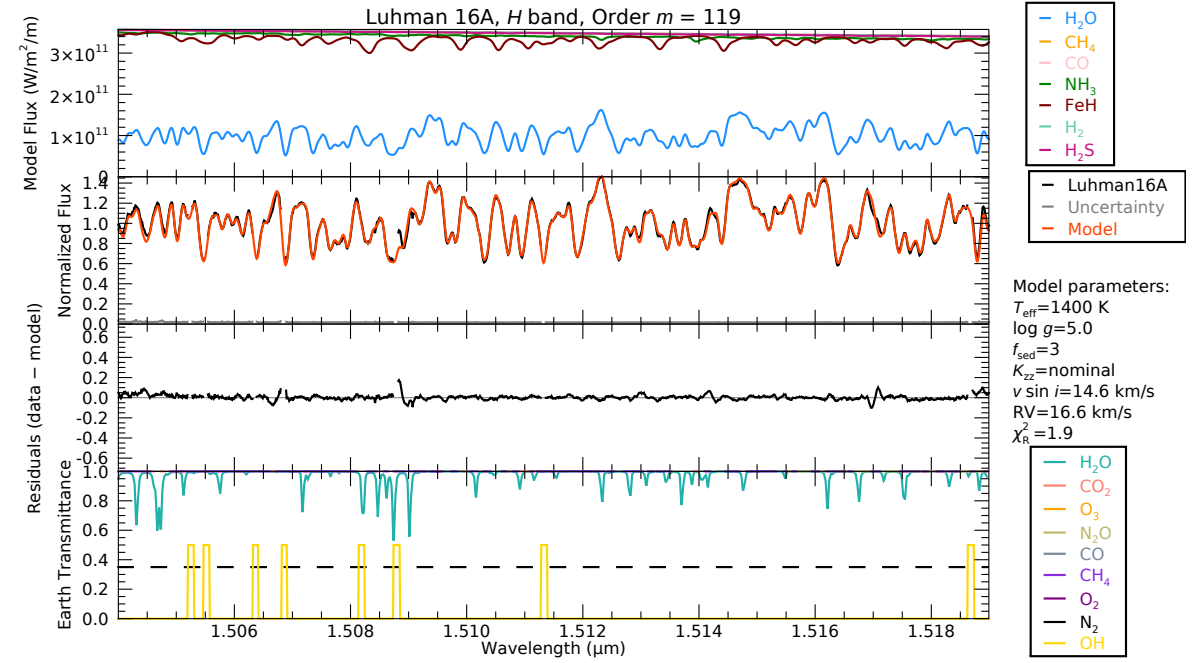


Figure B1. Continued.

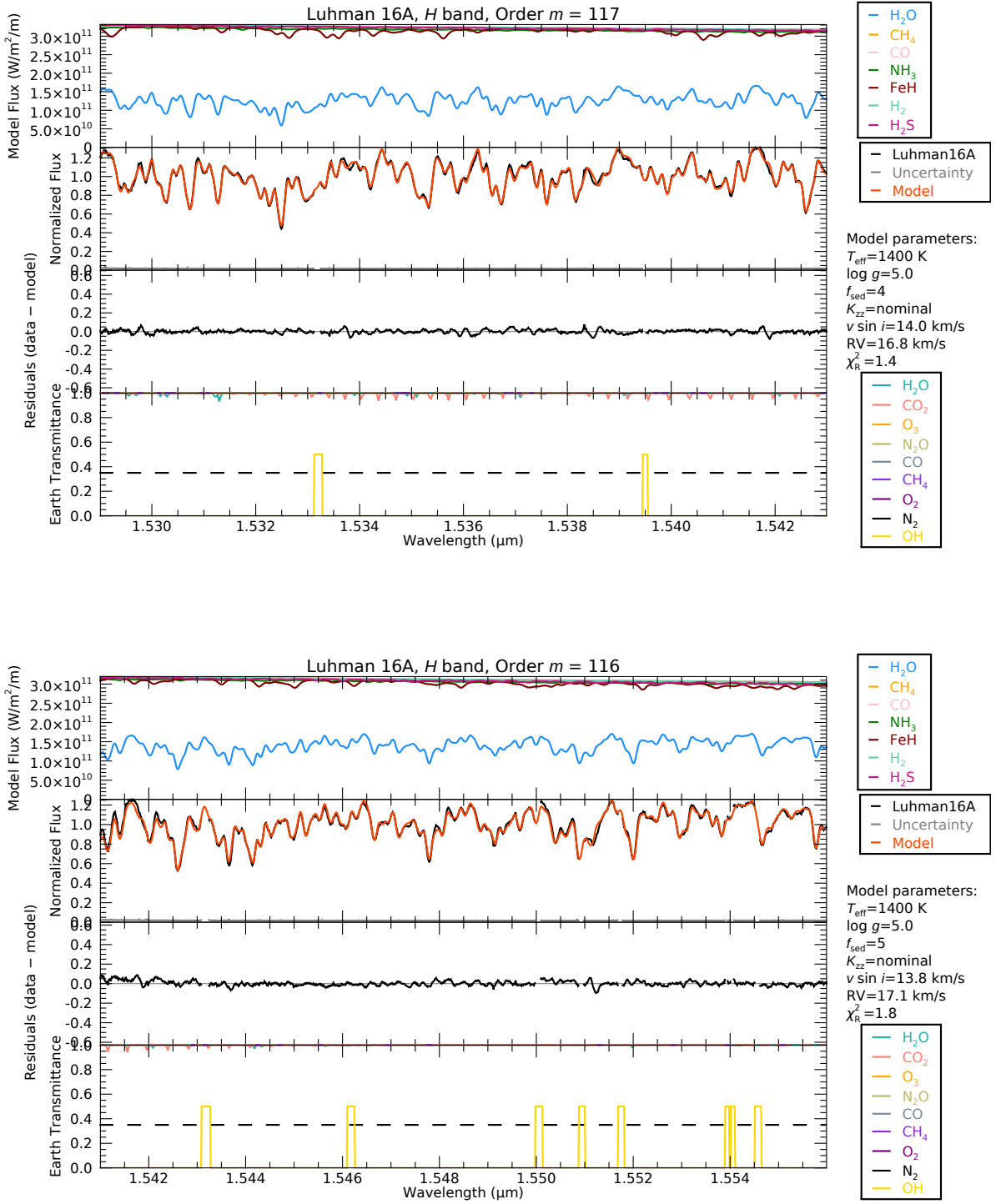


Figure B1. Continued.

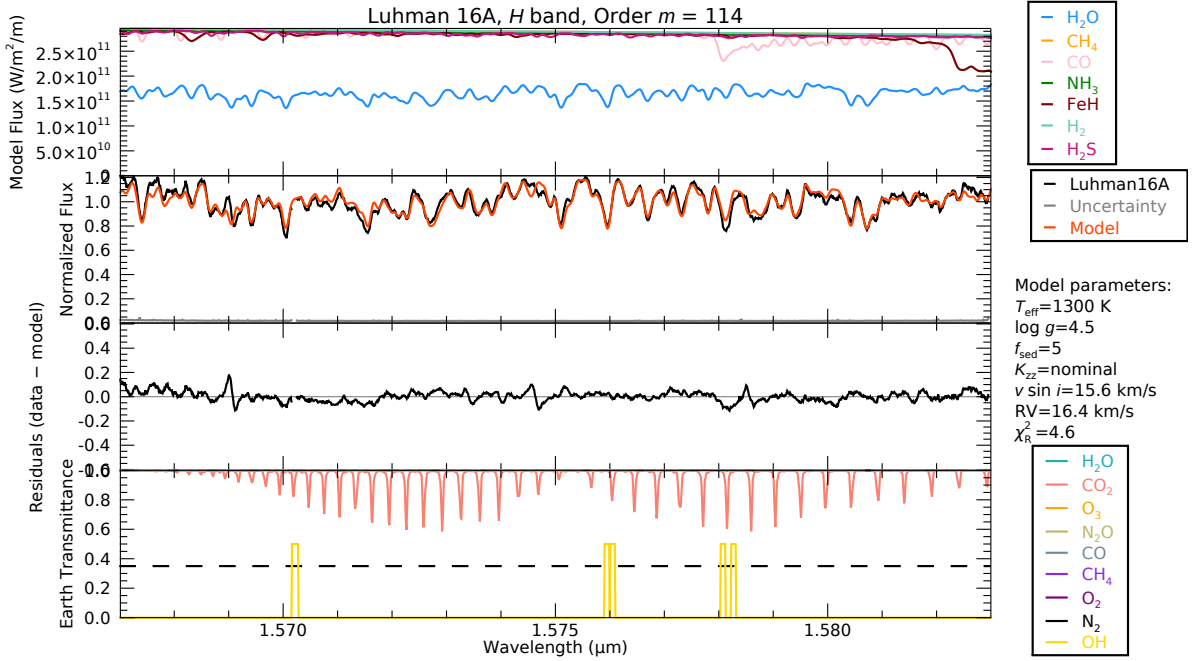
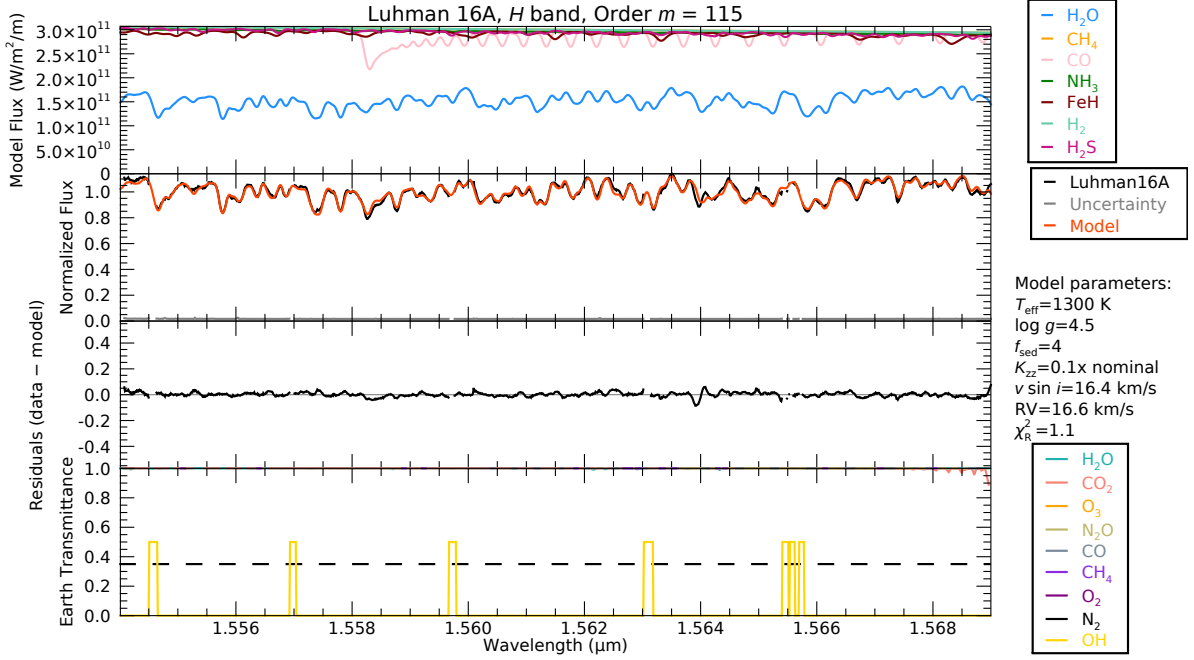


Figure B1. Continued.

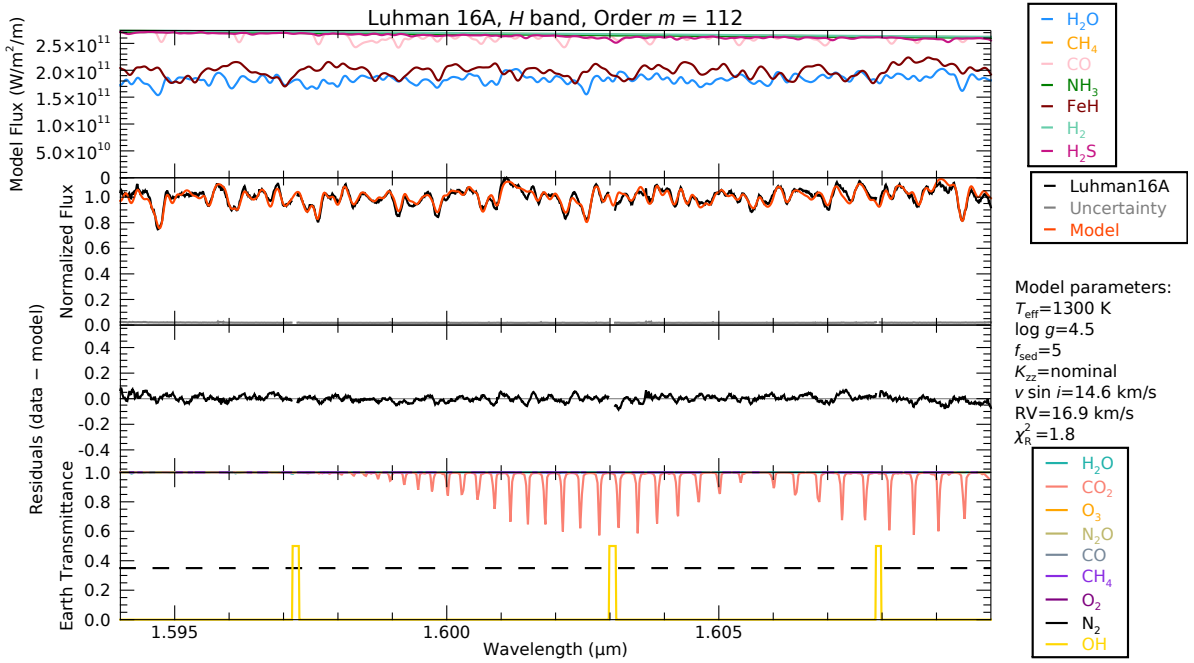
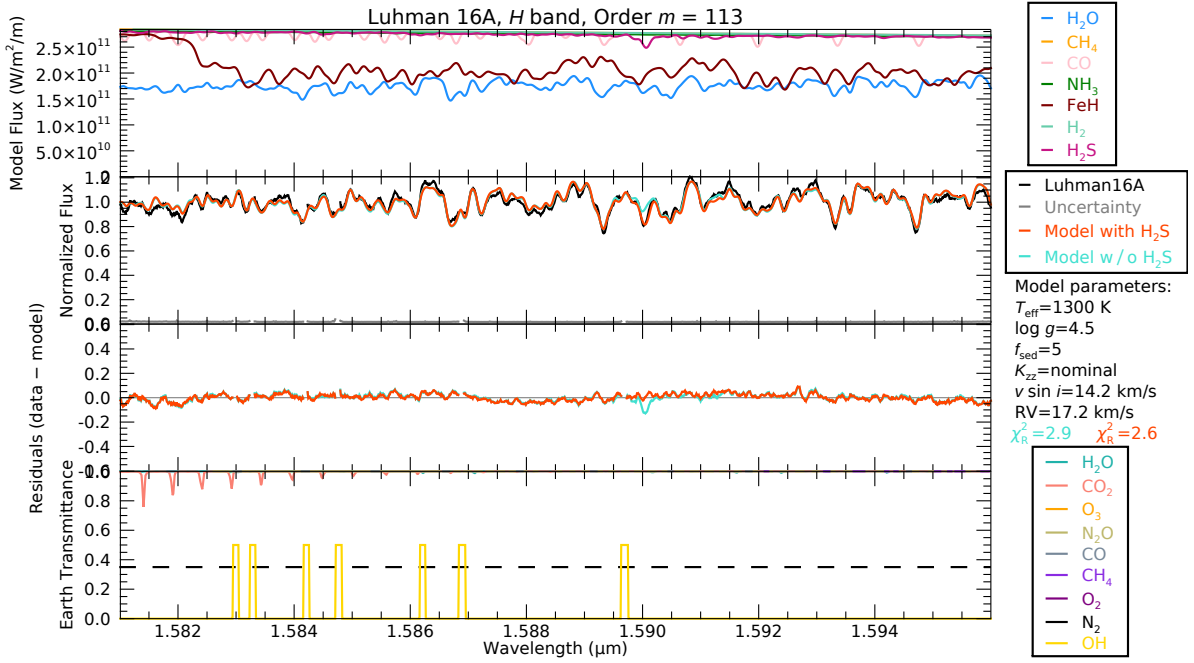


Figure B1. Continued.

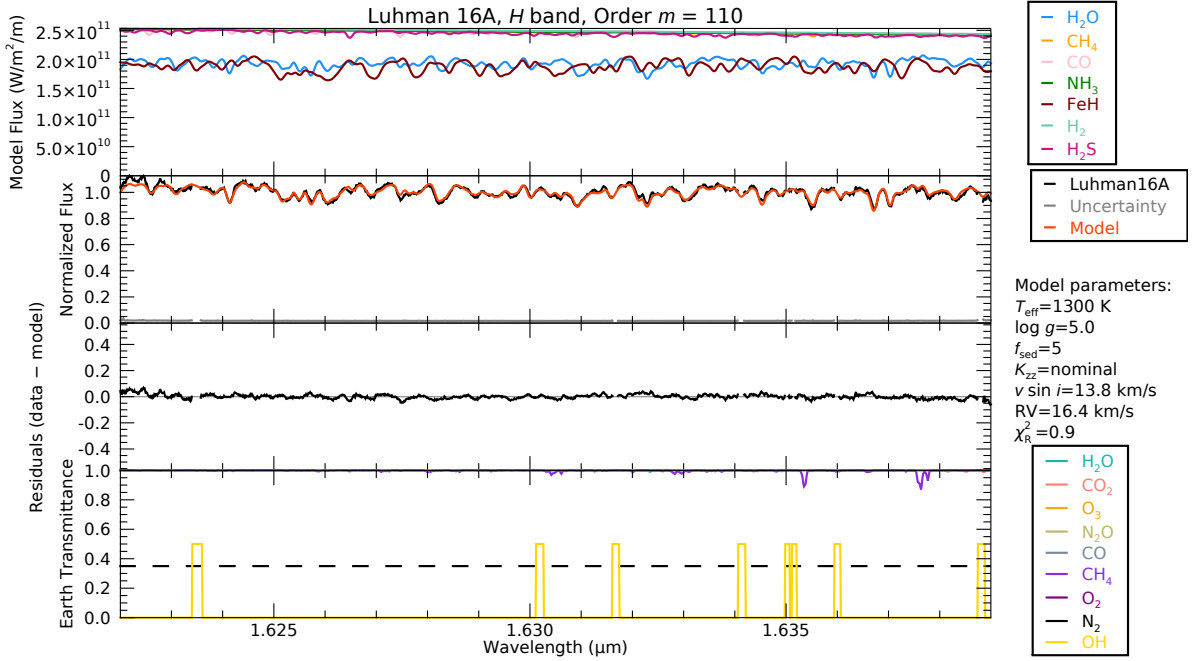
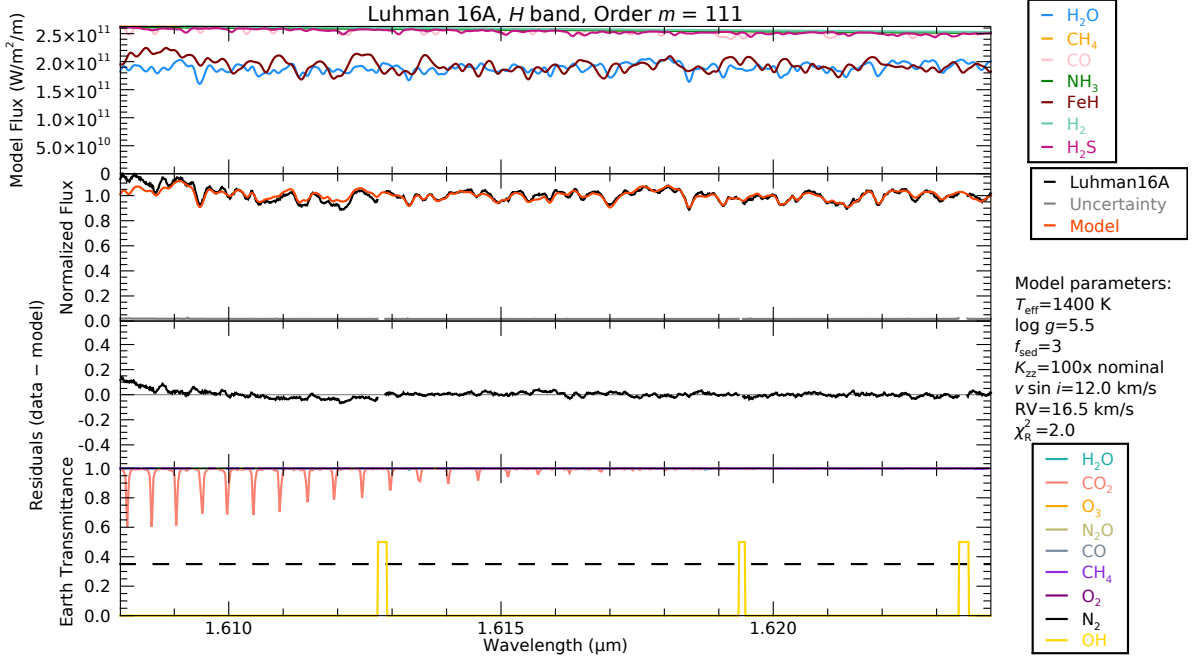


Figure B1. Continued.

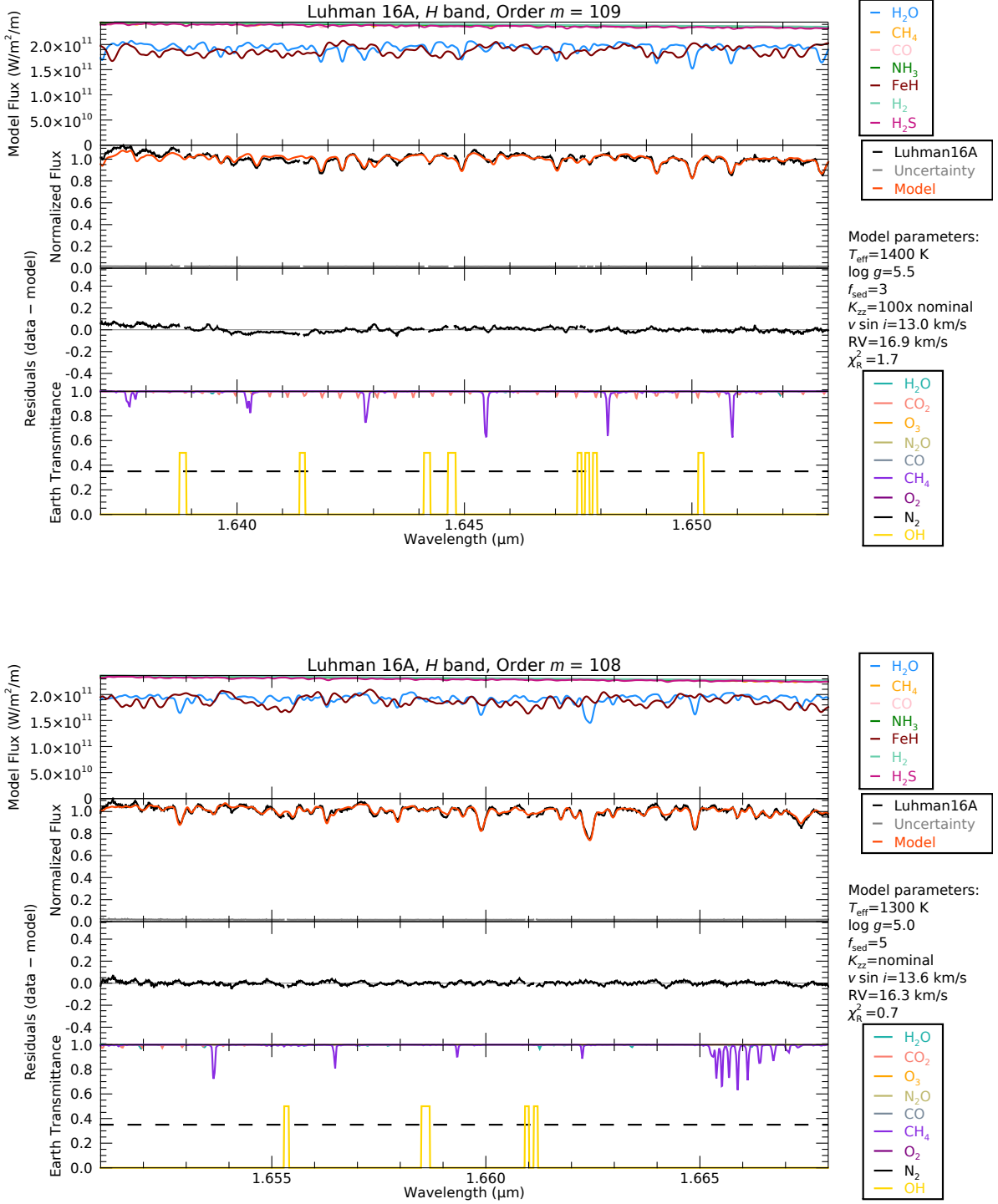


Figure B1. Continued.

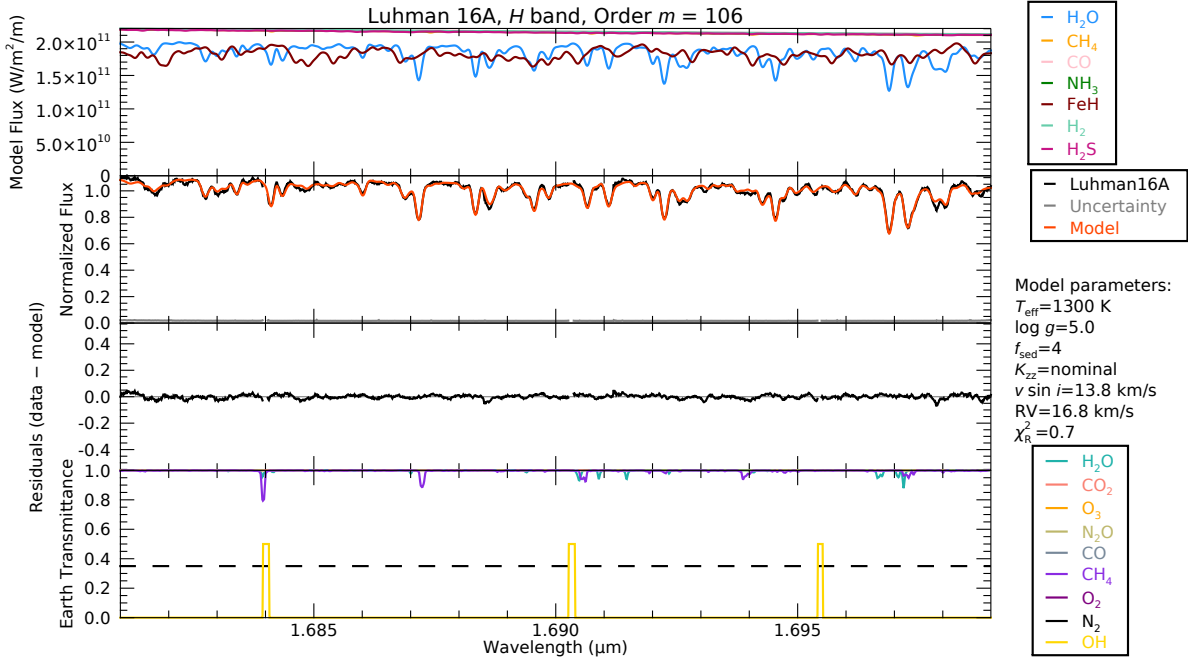
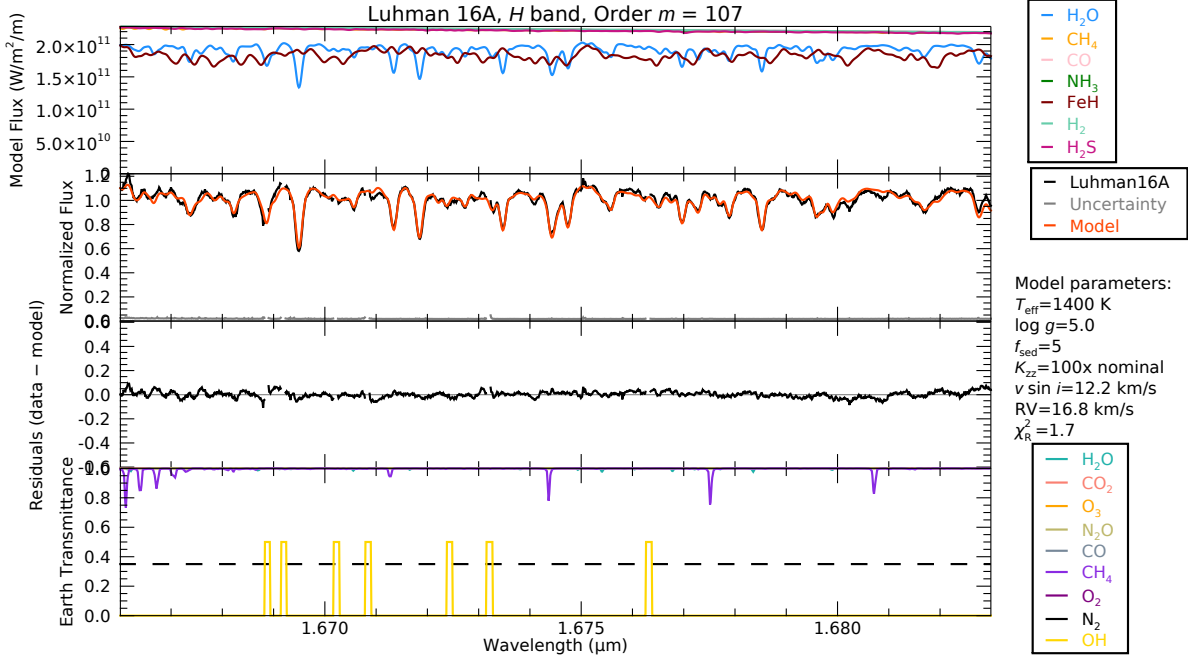


Figure B1. Continued.

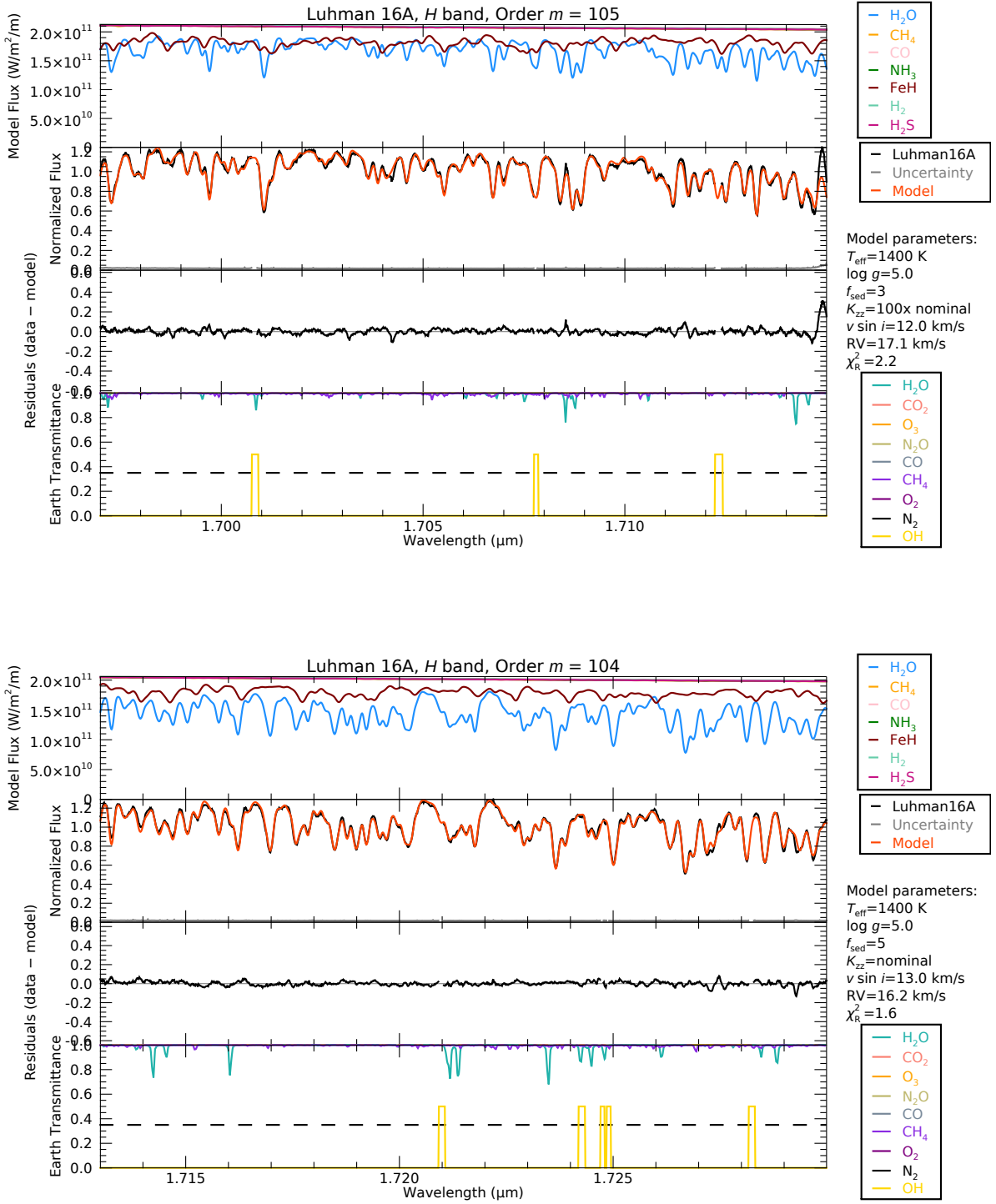


Figure B1. Continued.

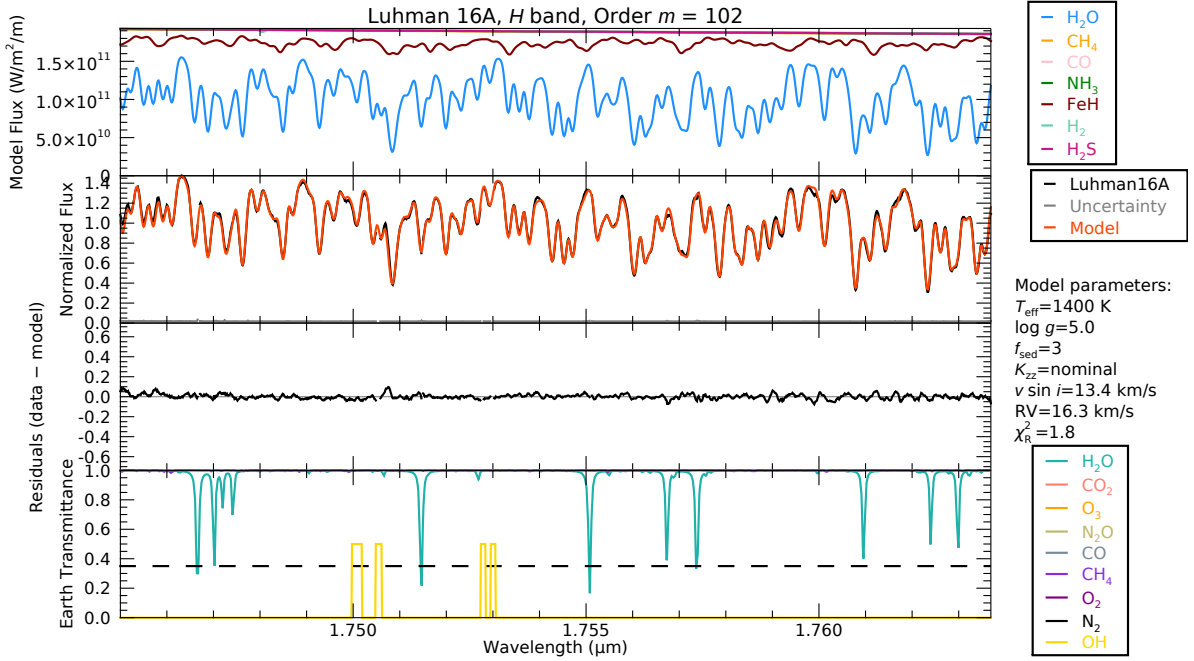
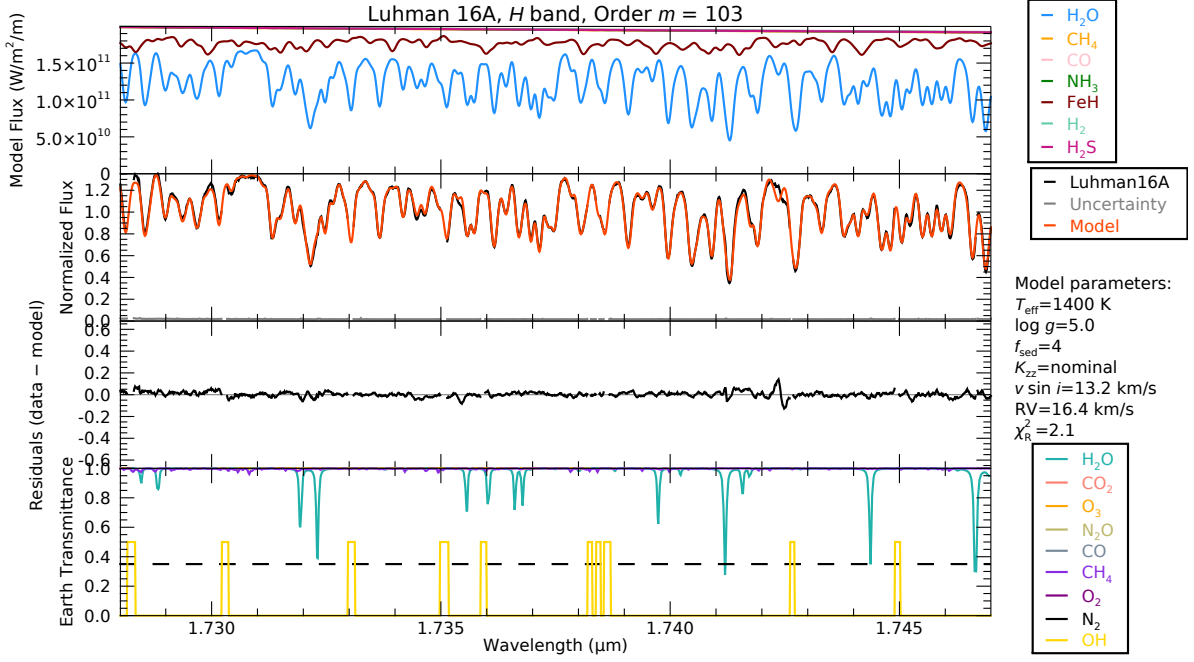


Figure B1. Continued.

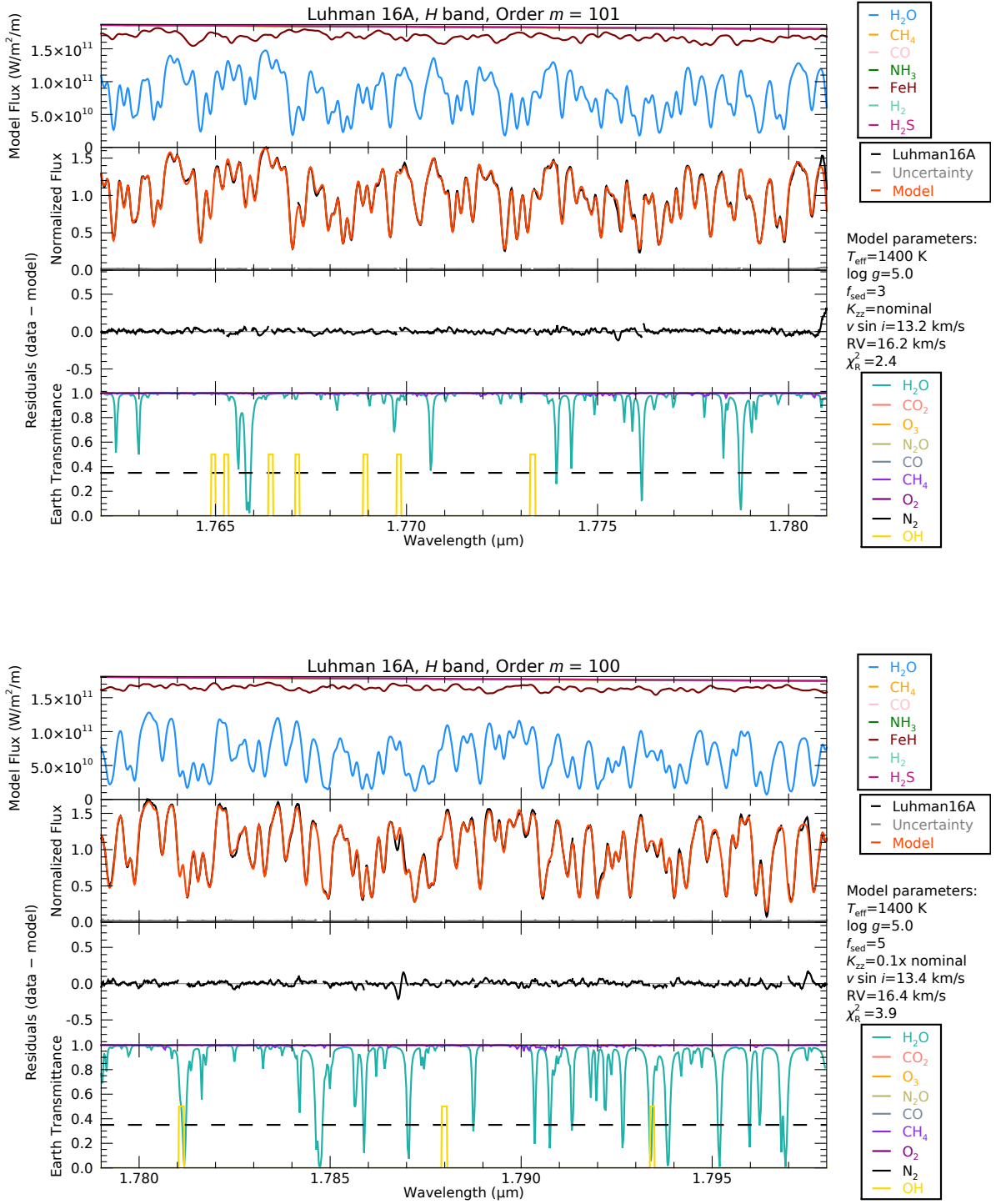


Figure B1. Continued.

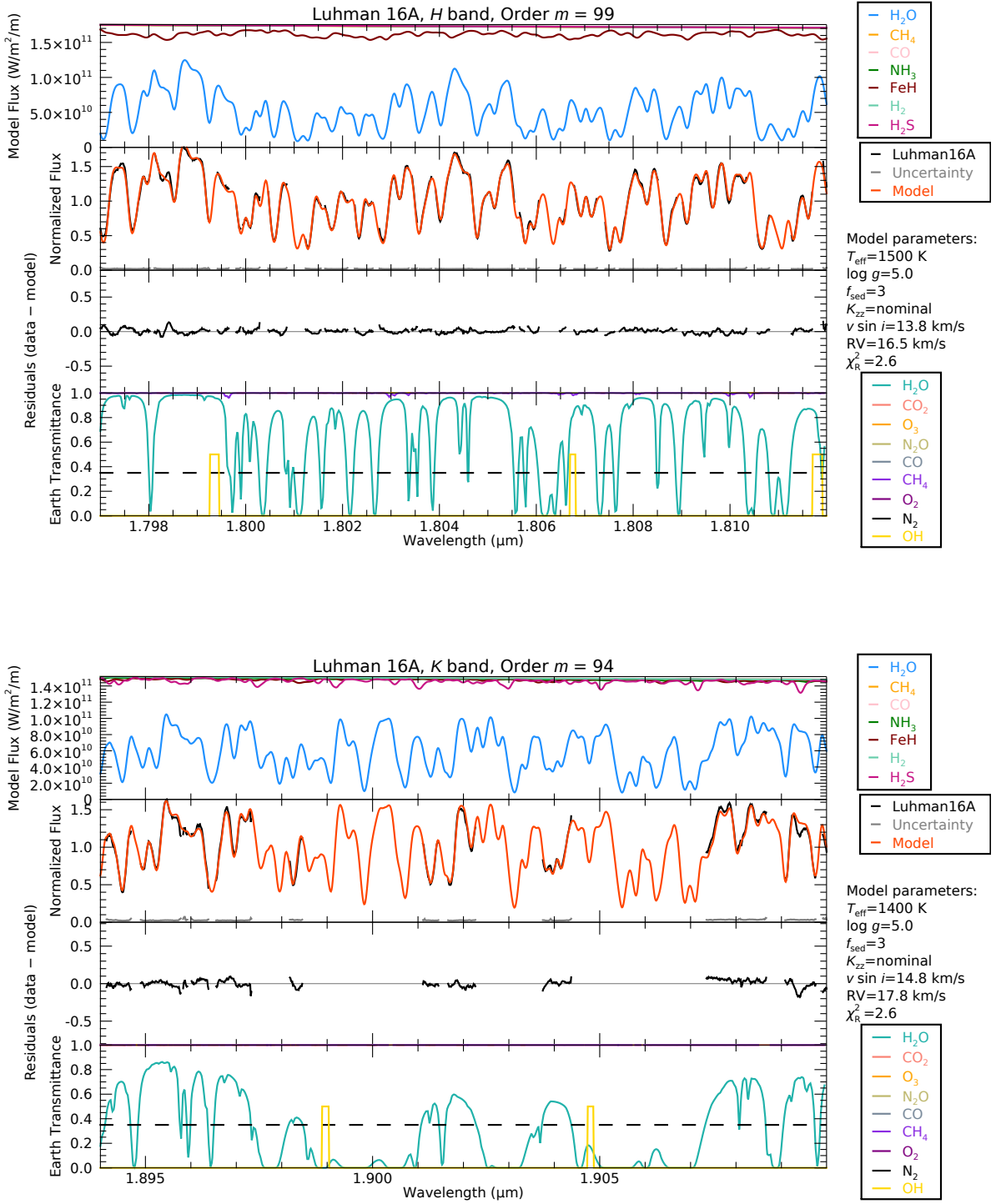


Figure B1. Continued.

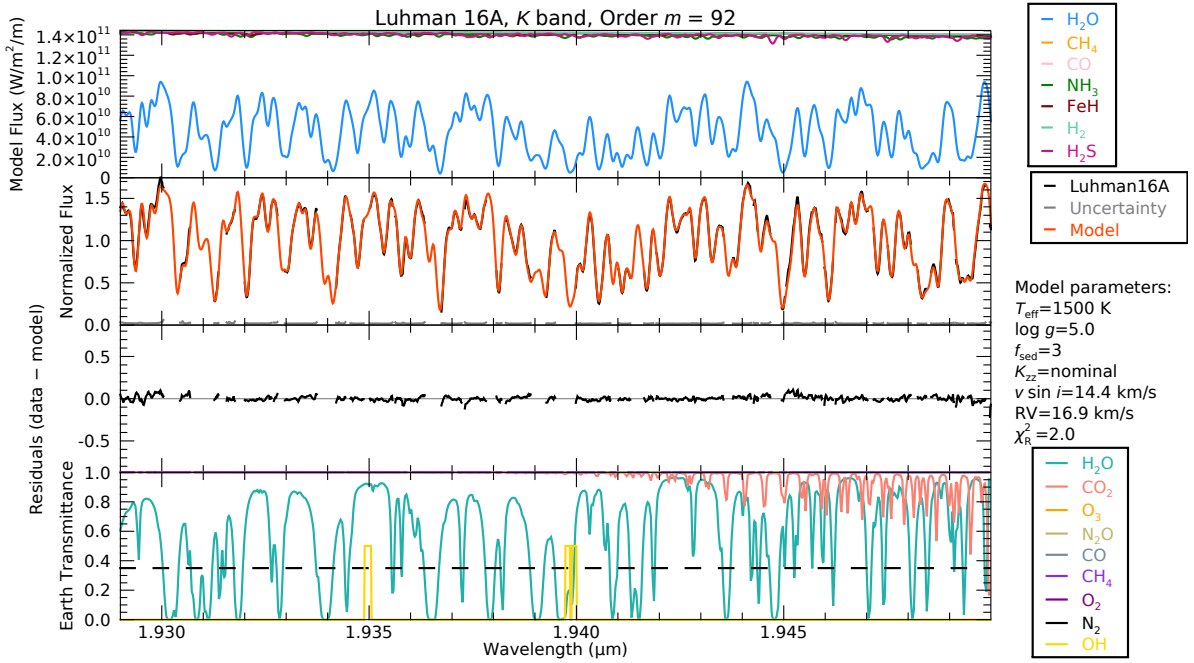
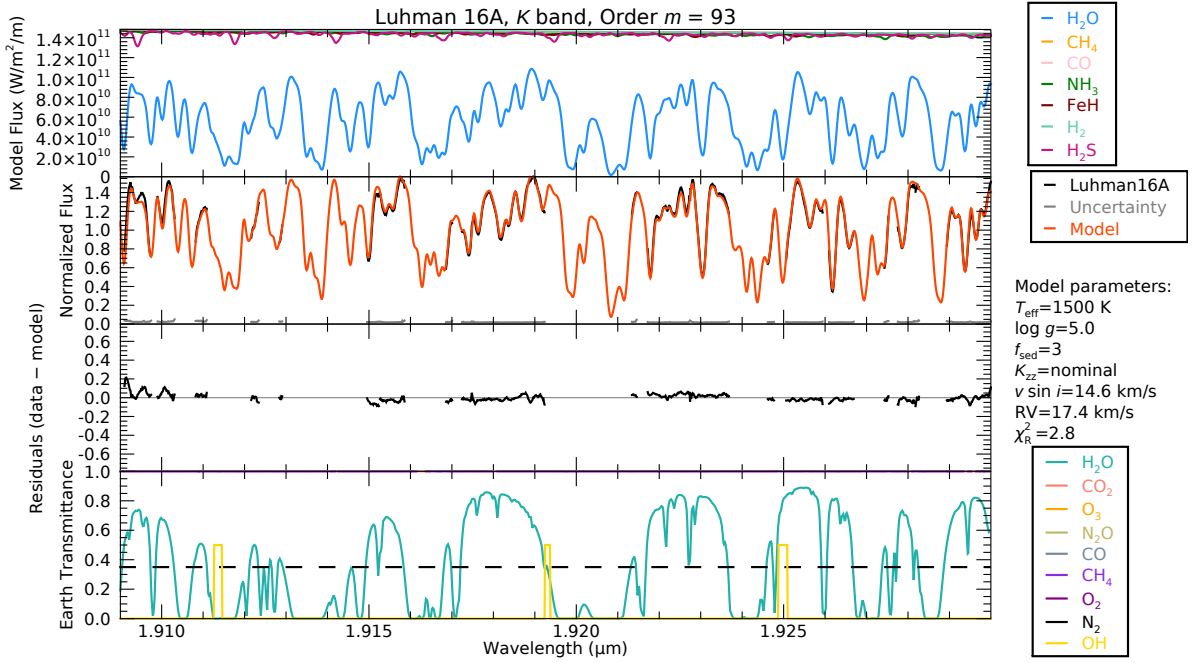


Figure B1. Continued.

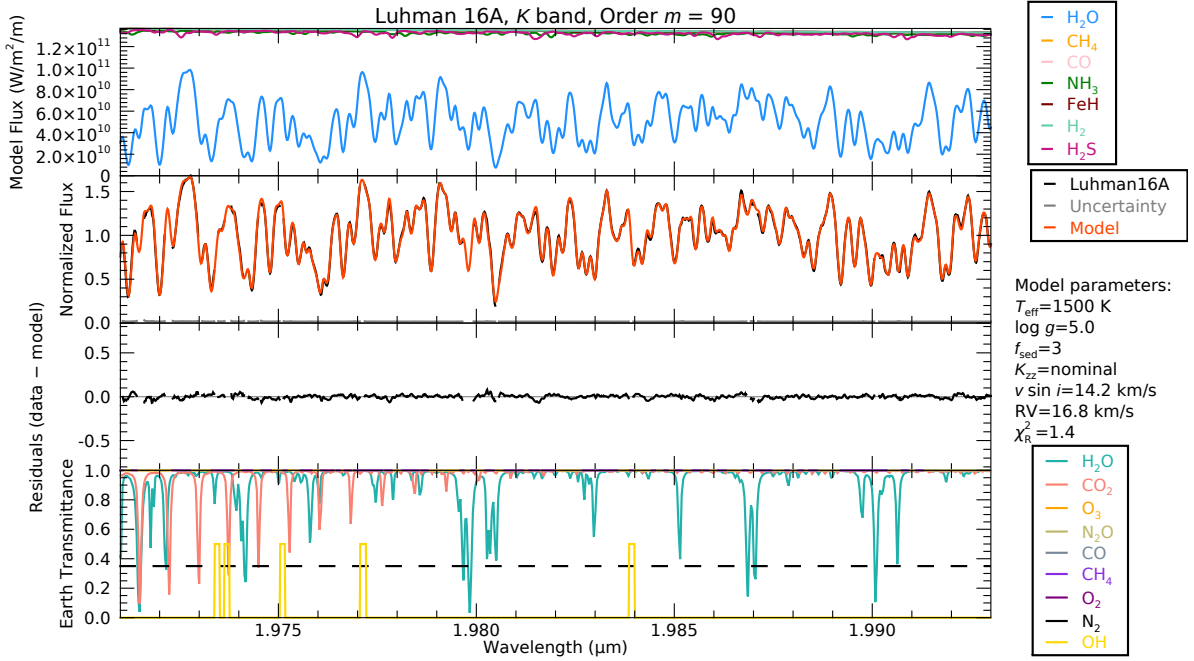
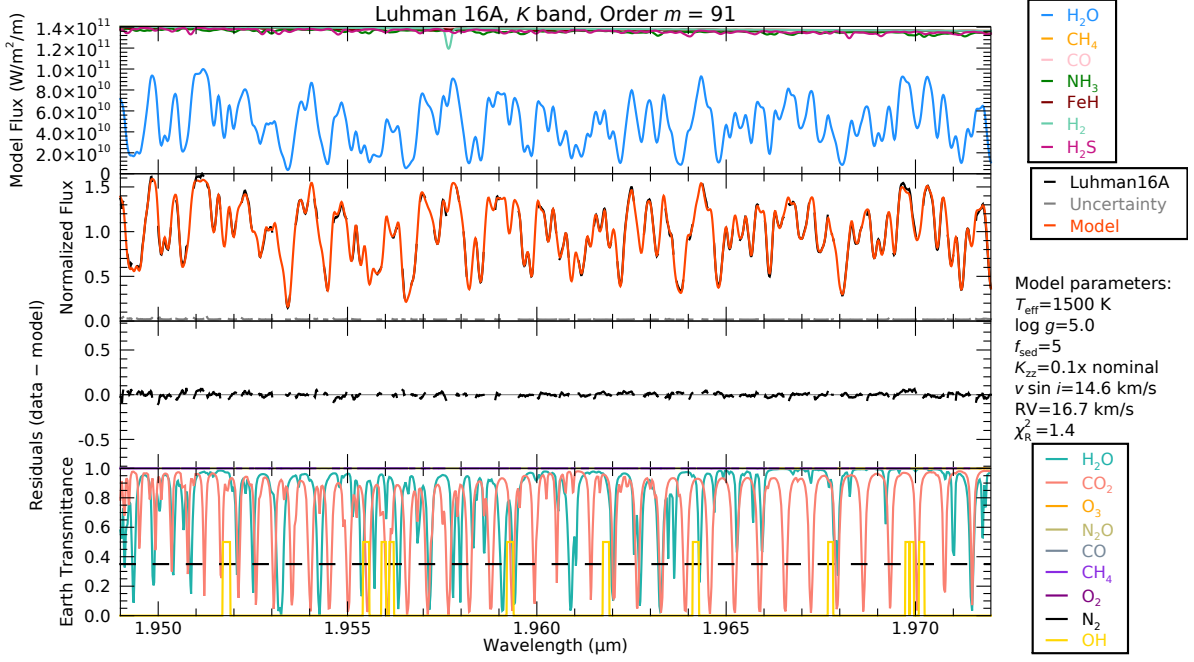


Figure B1. Continued.

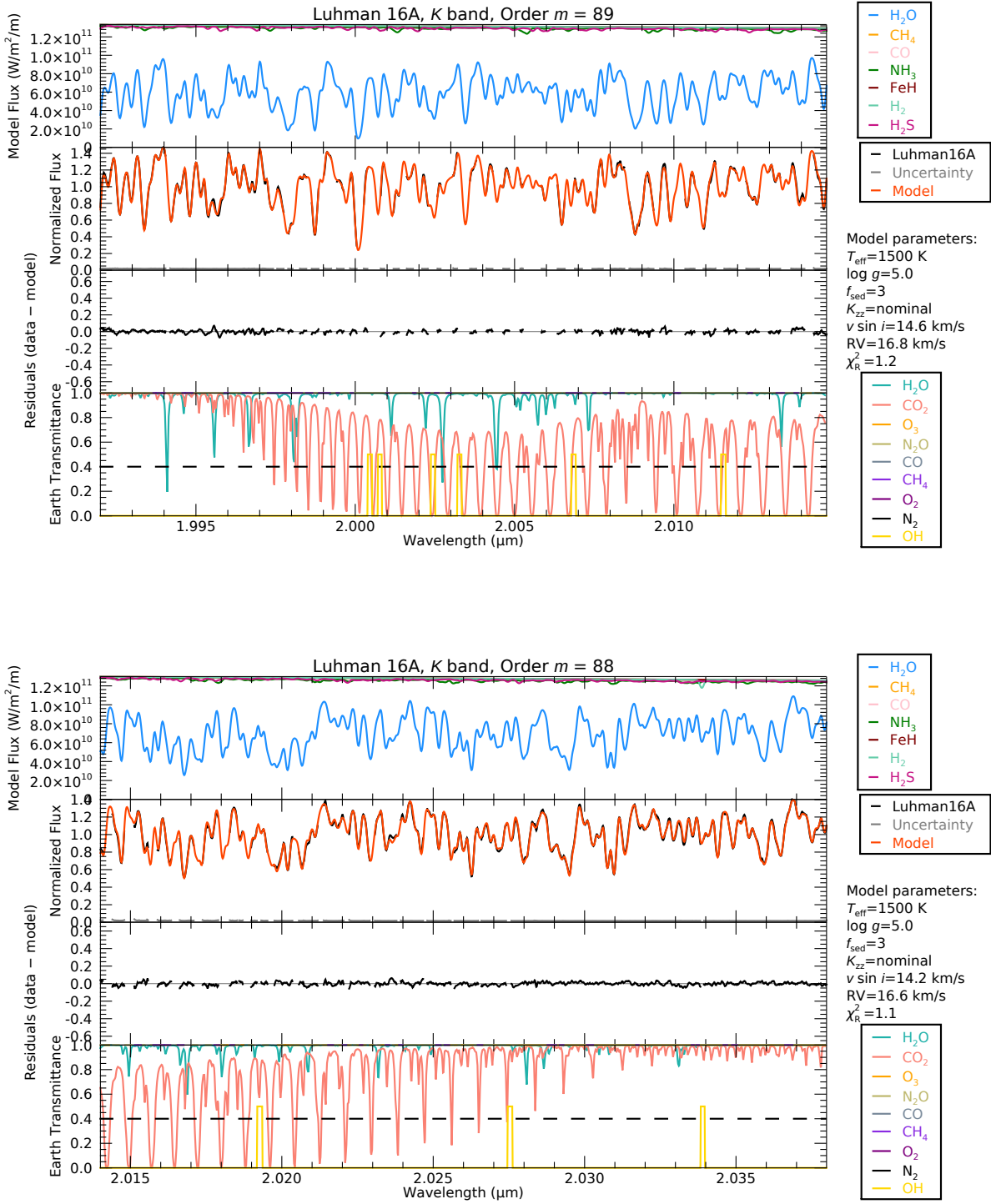


Figure B1. Continued.

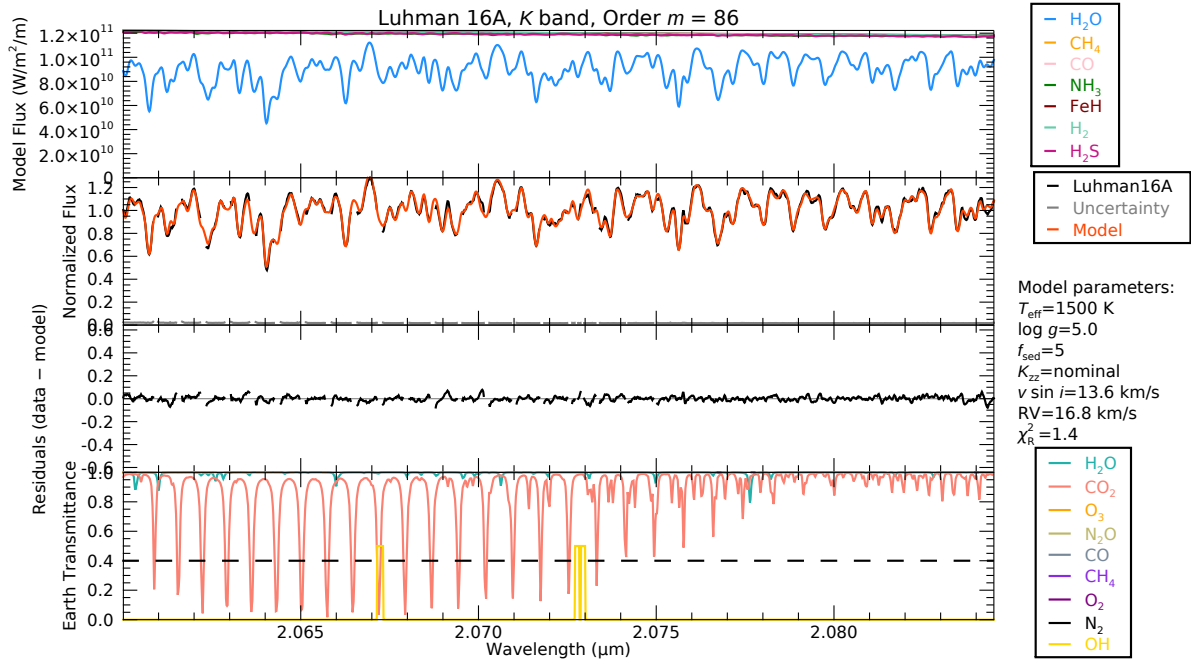
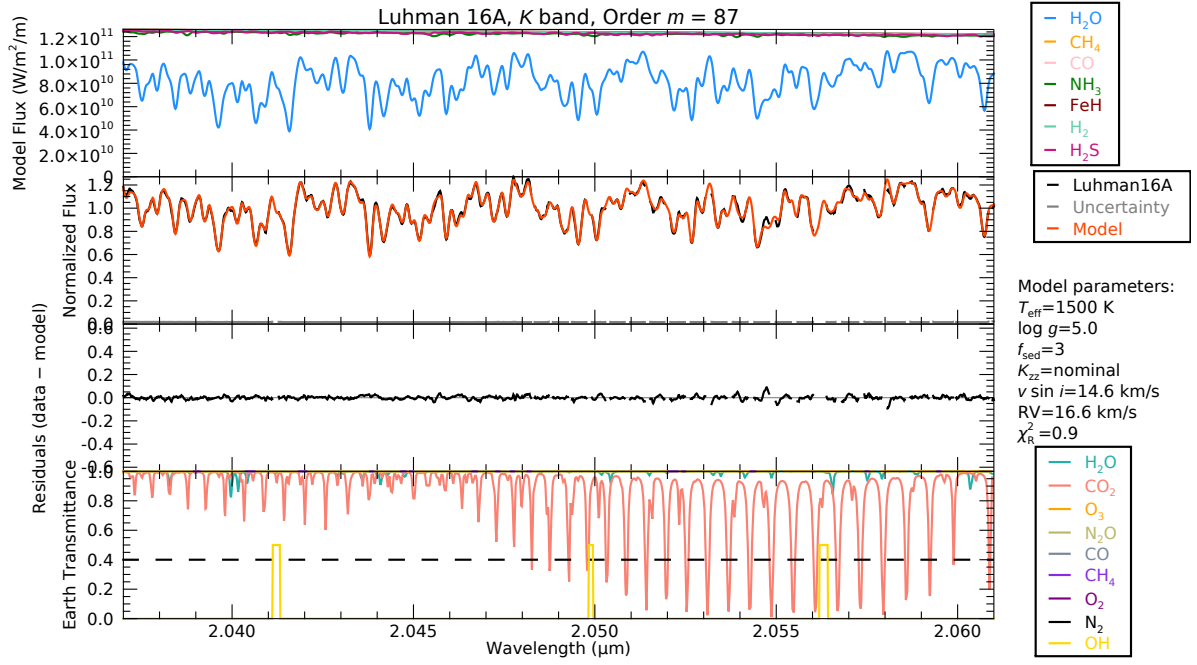


Figure B1. Continued.

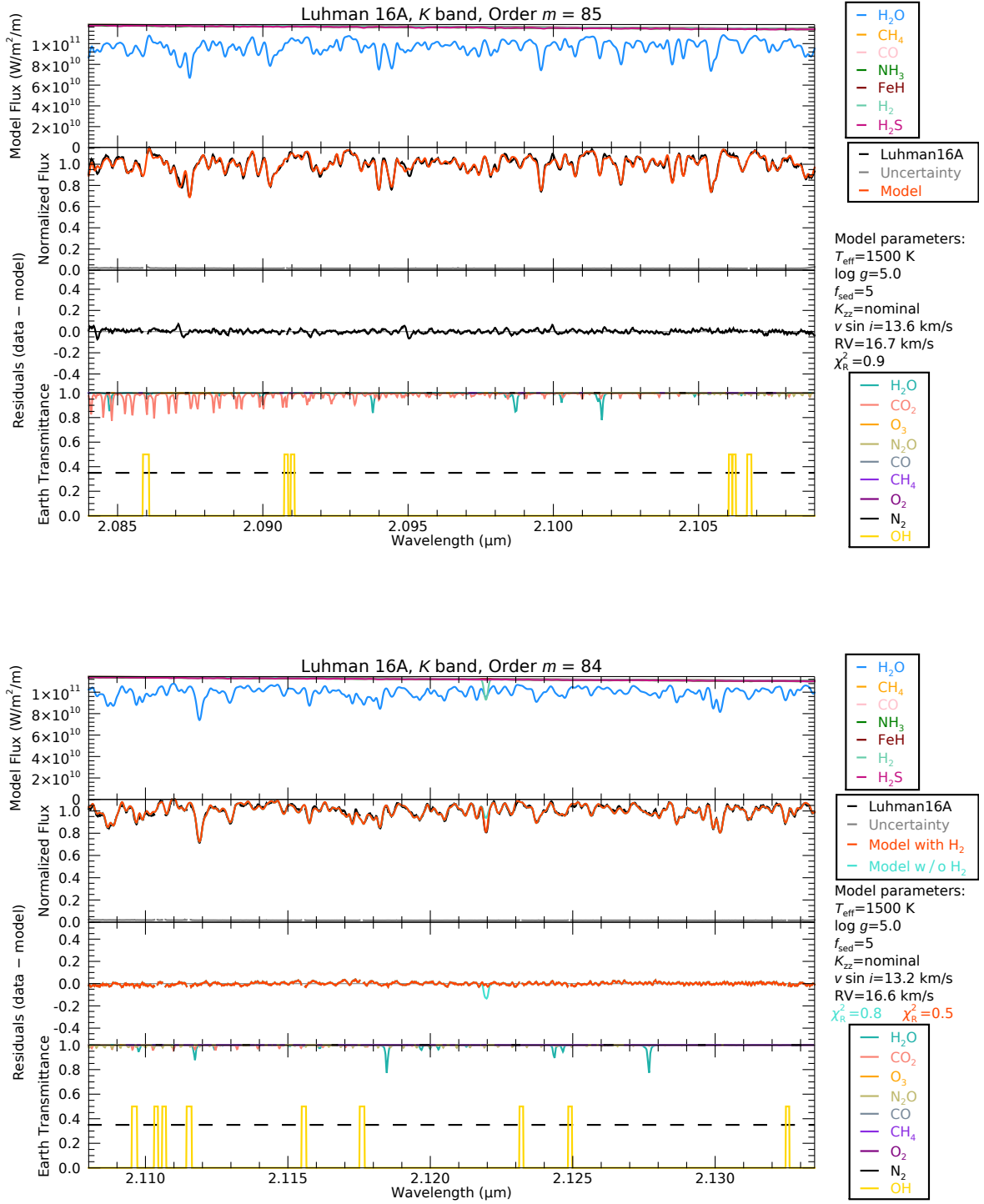


Figure B1. Continued.

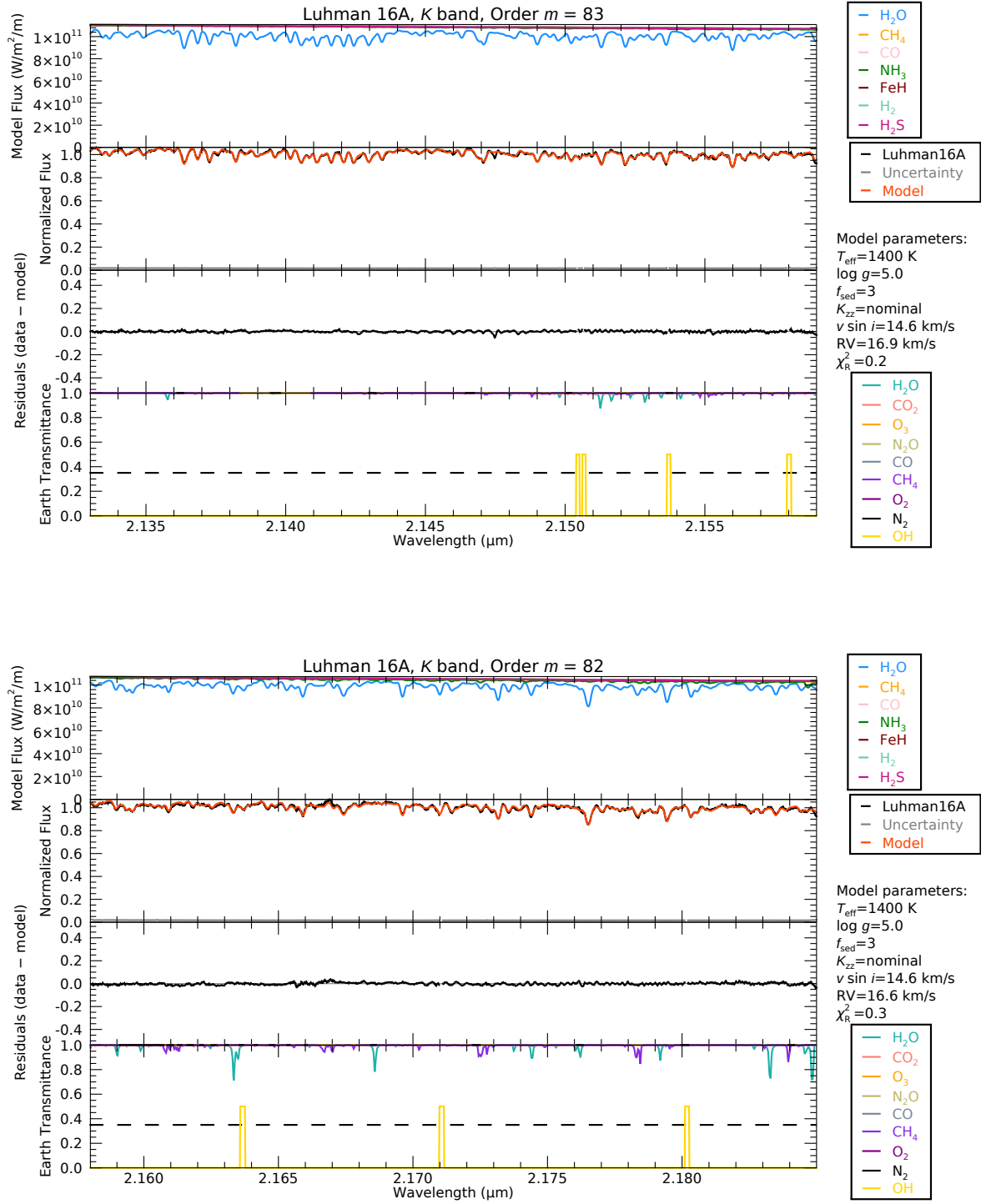


Figure B1. Continued.

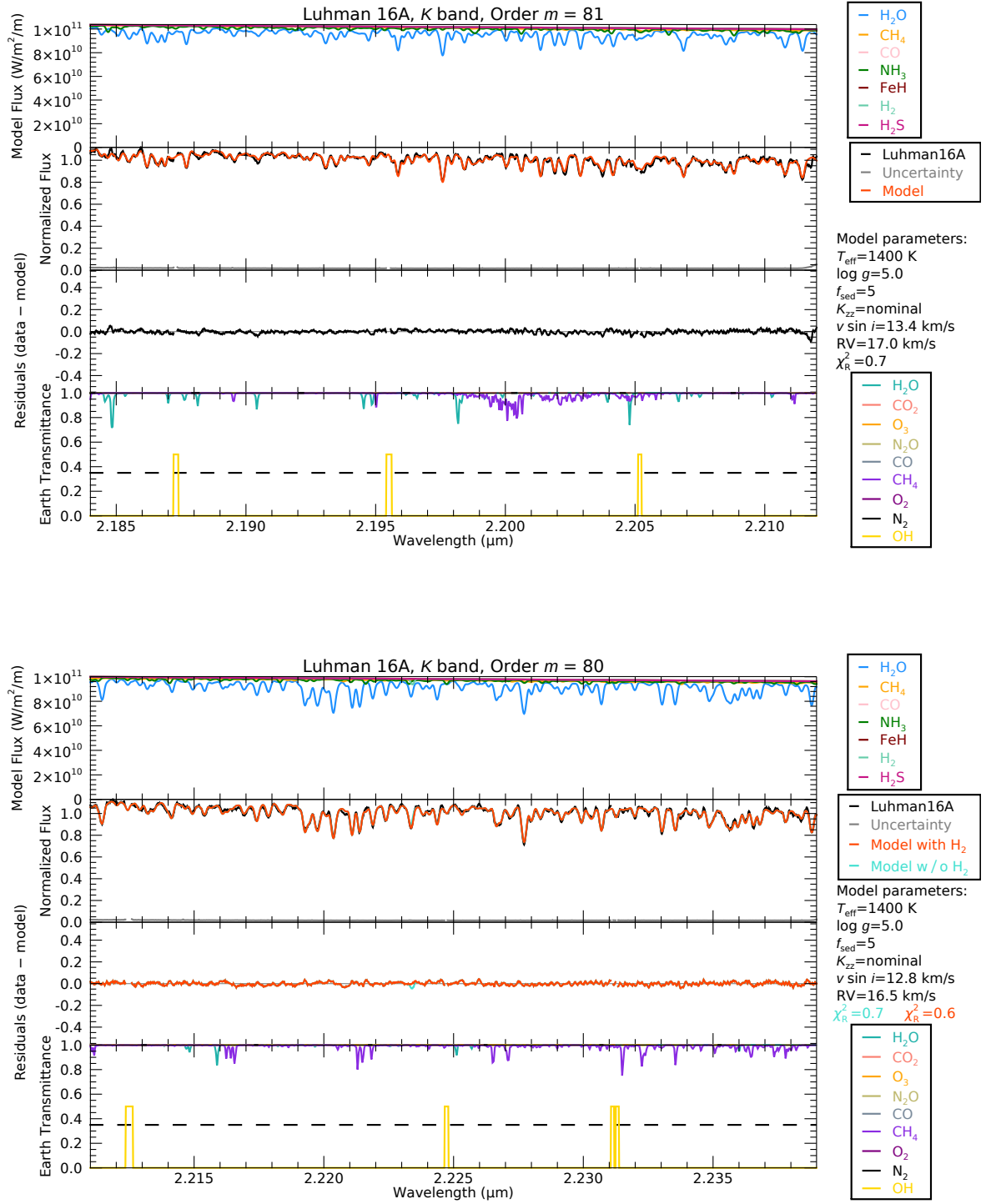


Figure B1. Continued.

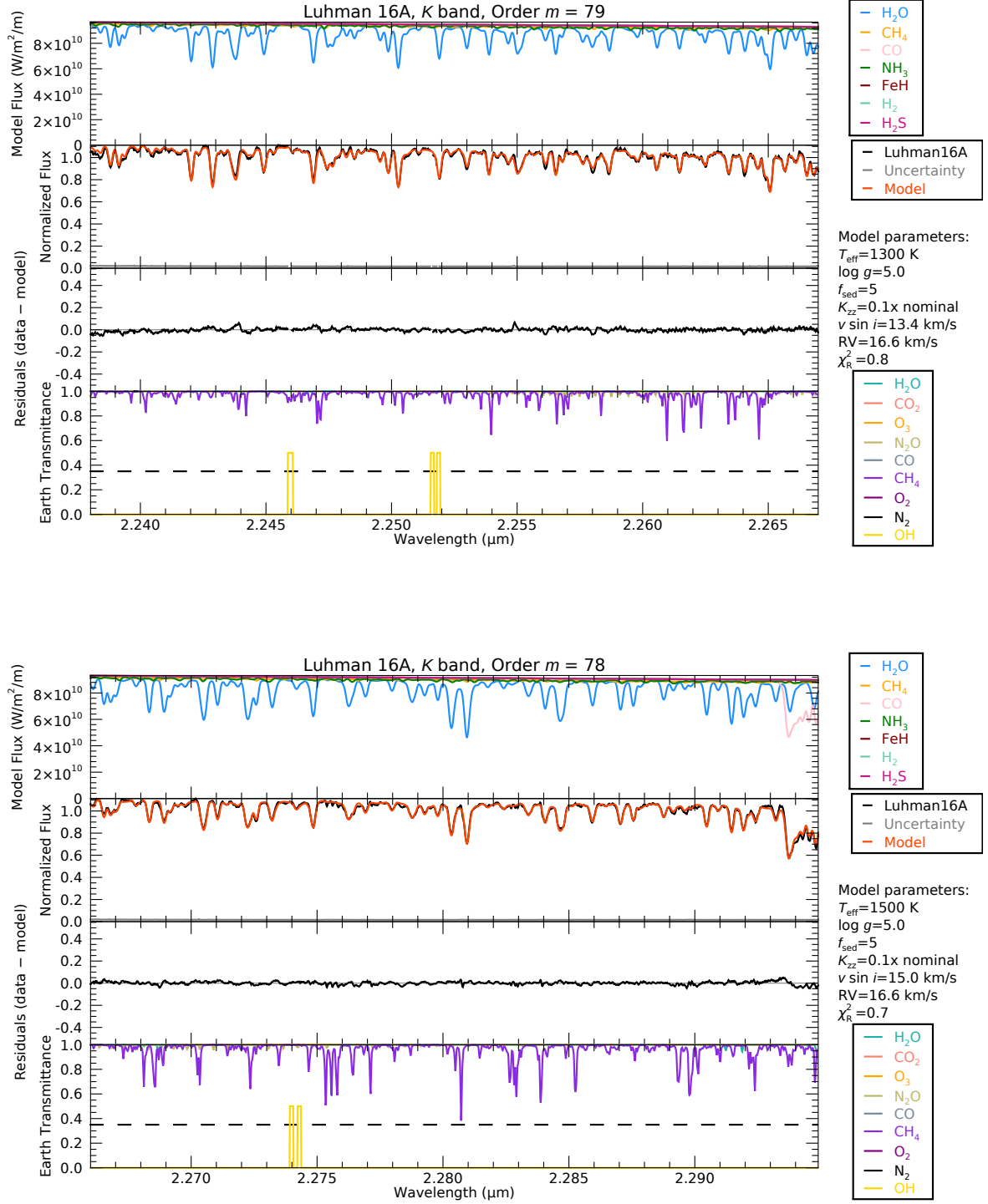


Figure B1. Continued.

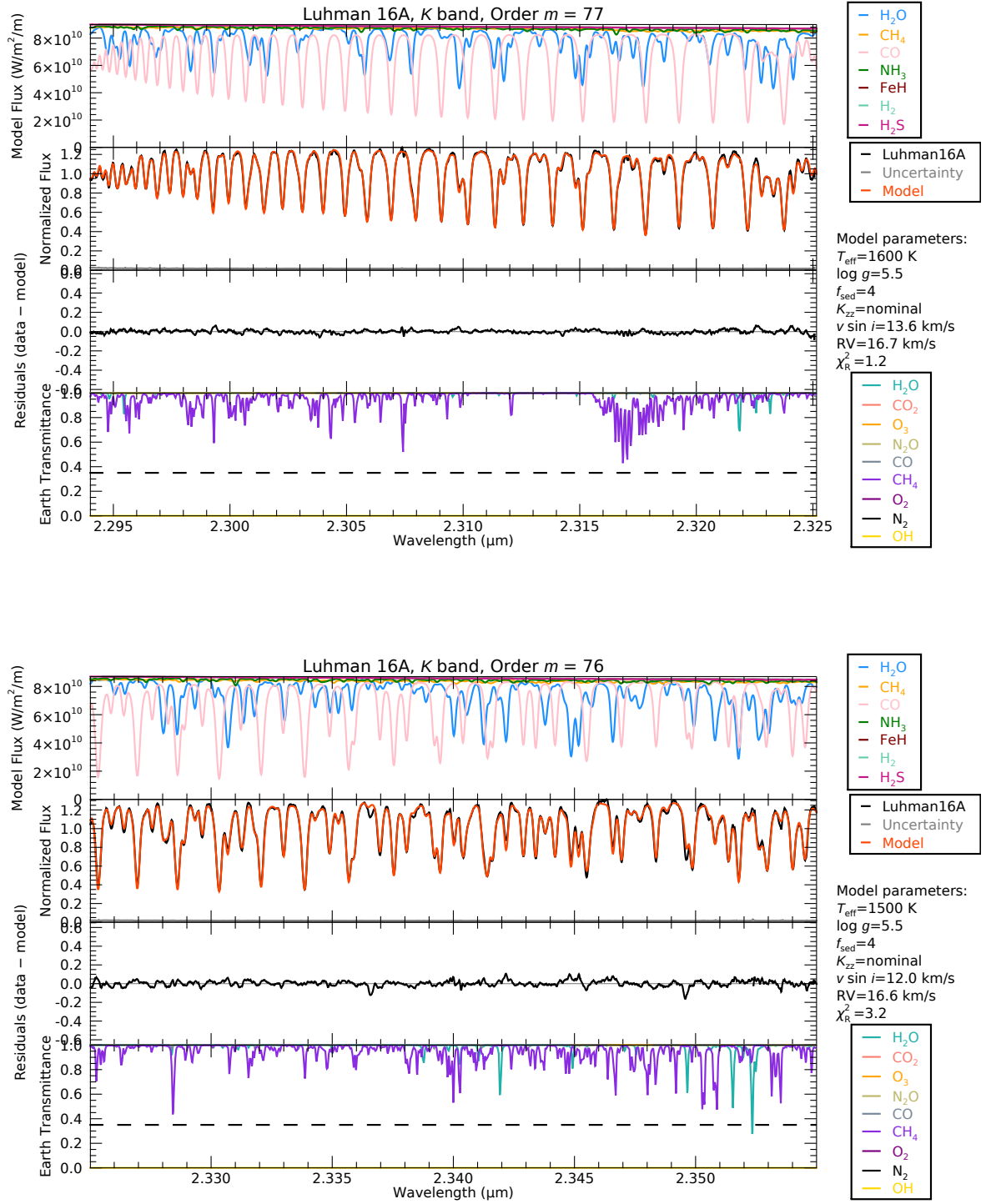


Figure B1. Continued.

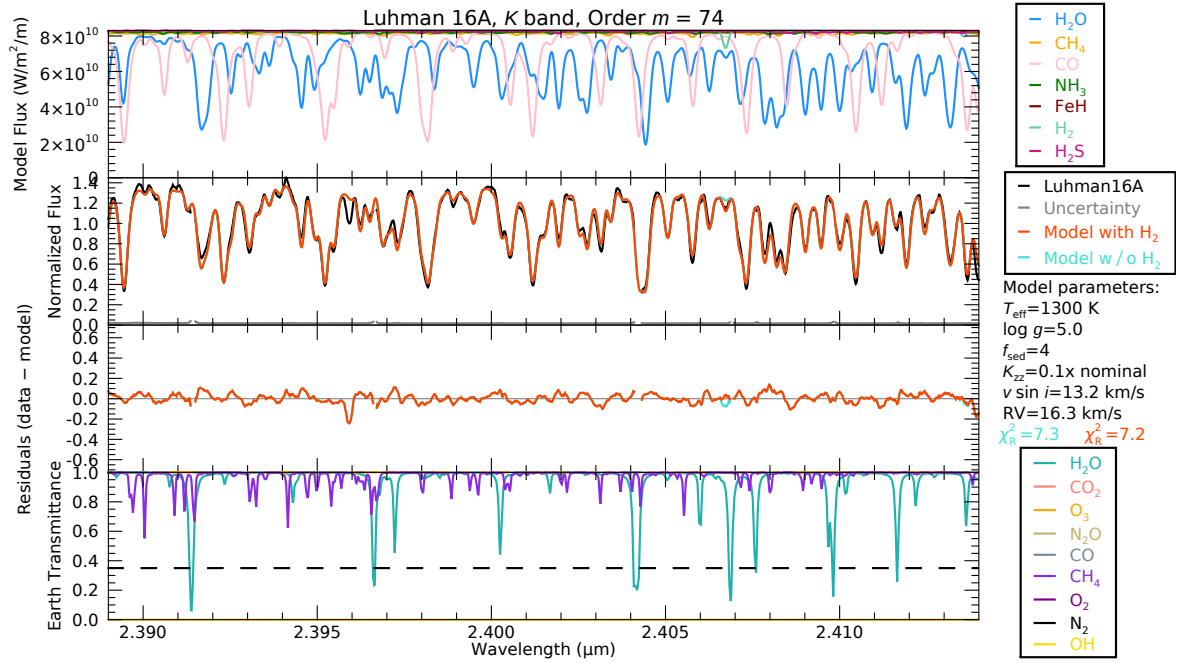
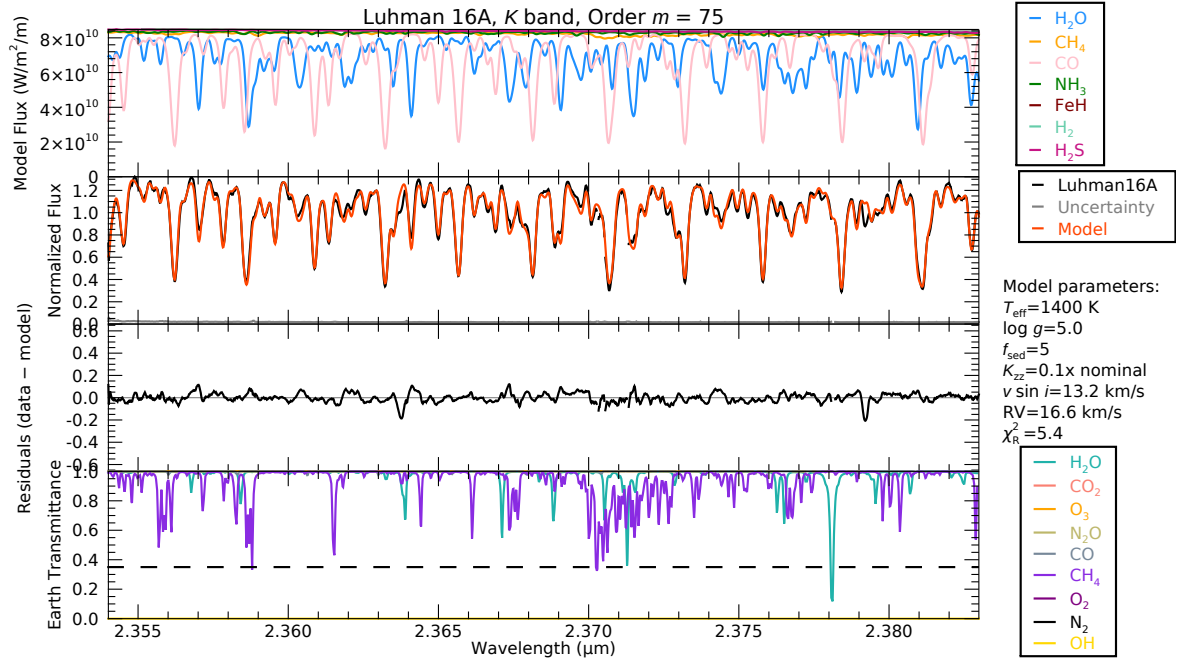


Figure B1. Continued.

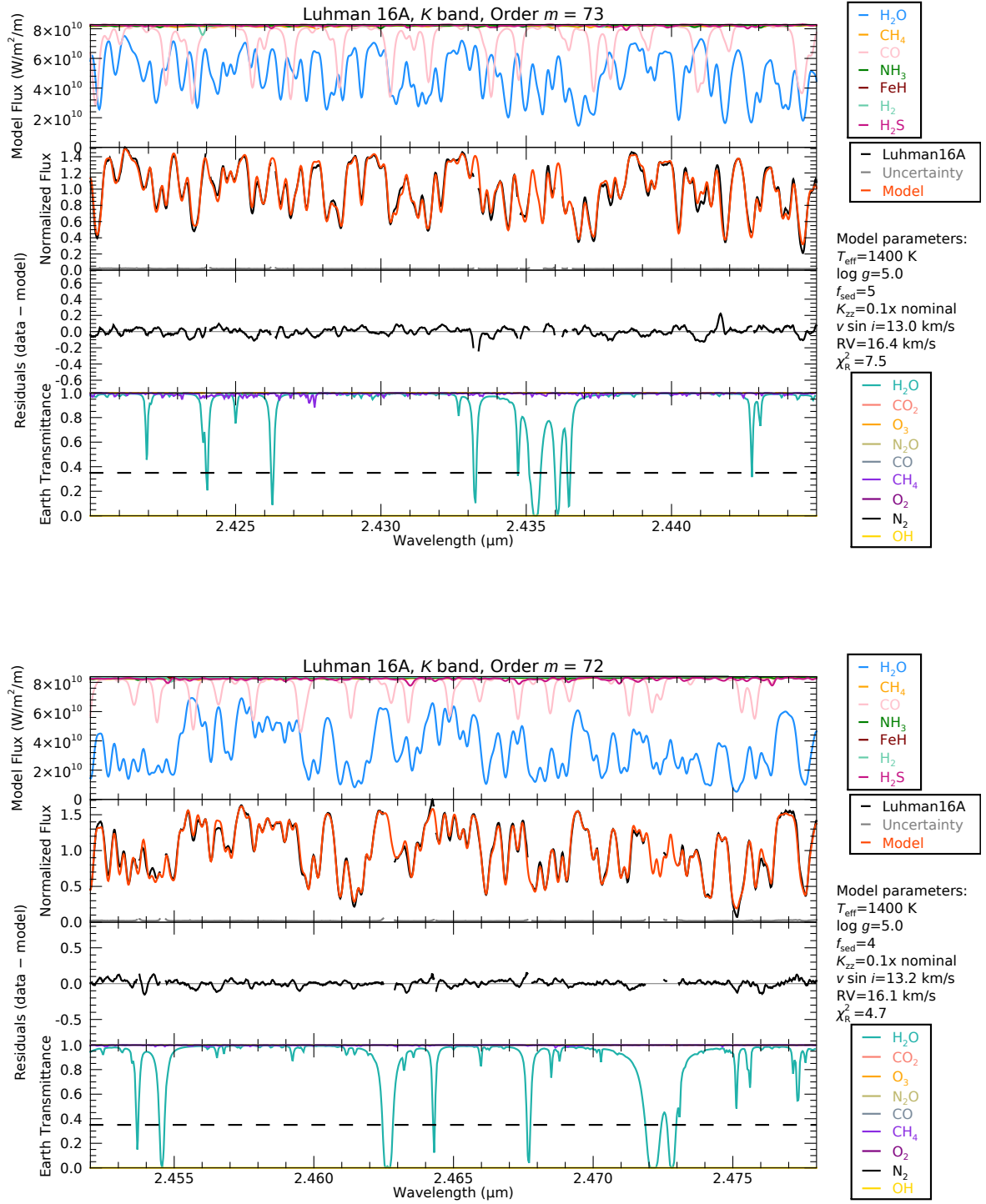


Figure B1. Continued.

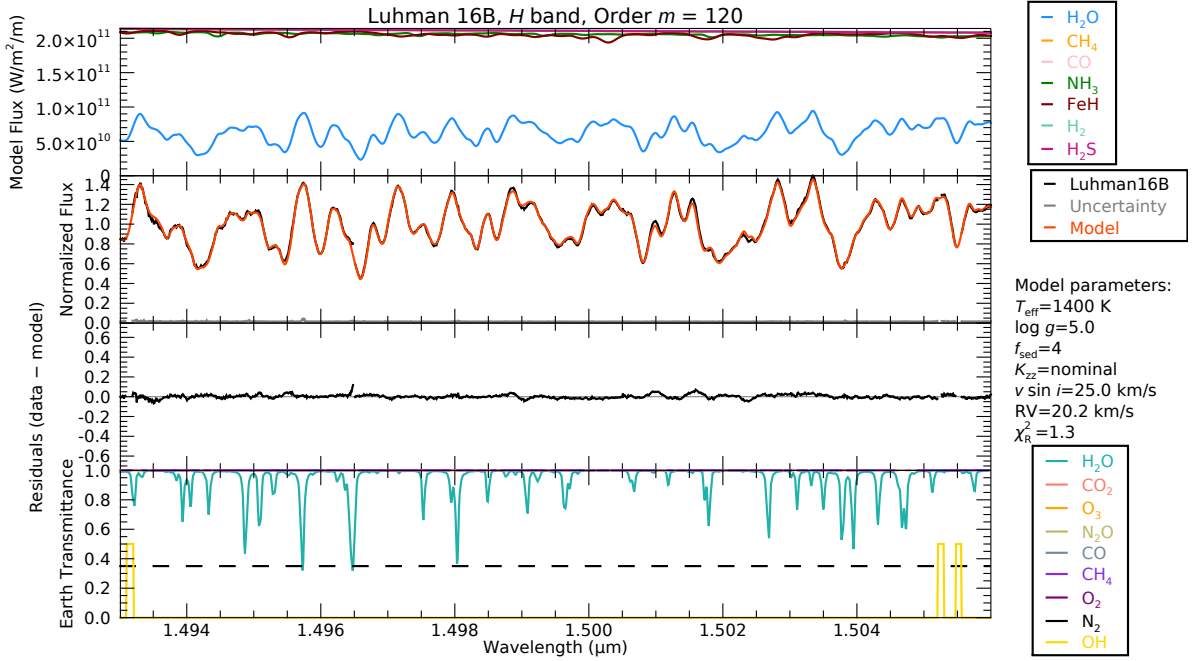
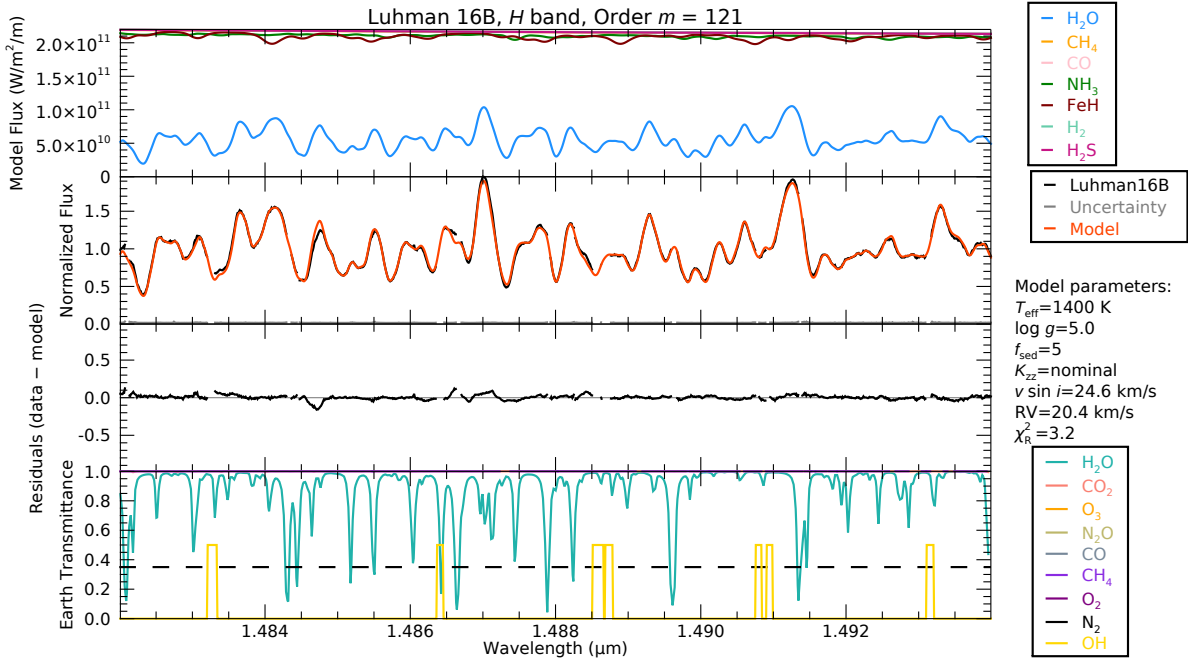


Figure B2. The spectral atlas of Luhman 16B in the same format as B1.

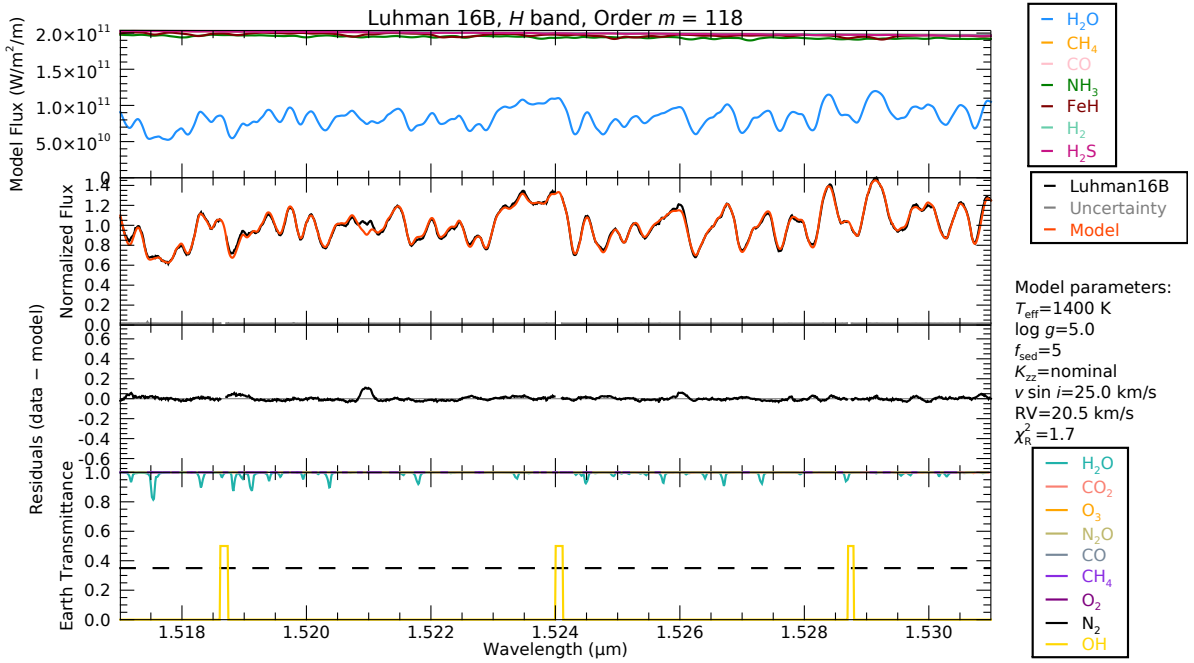
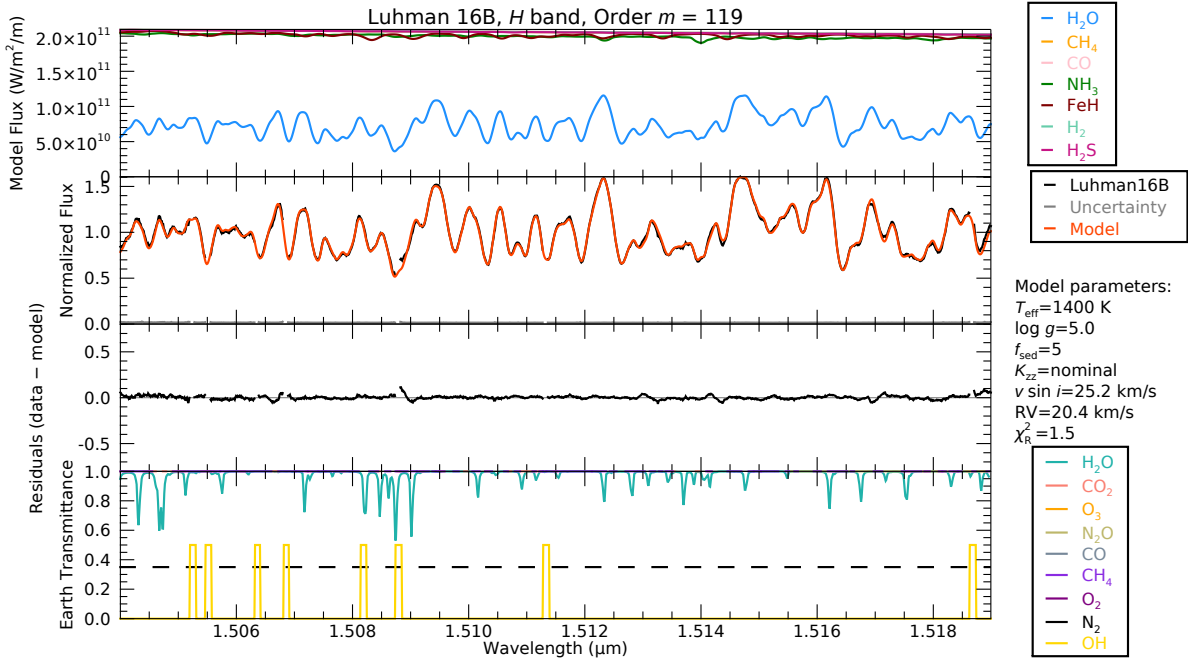


Figure B2. Continued.

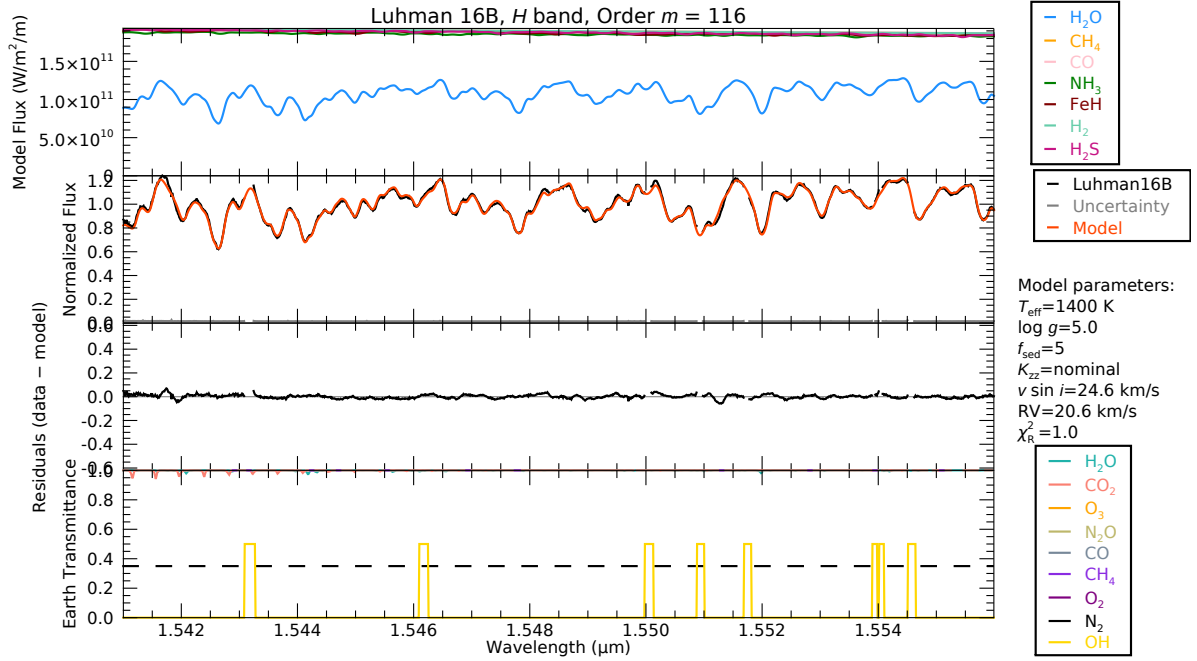
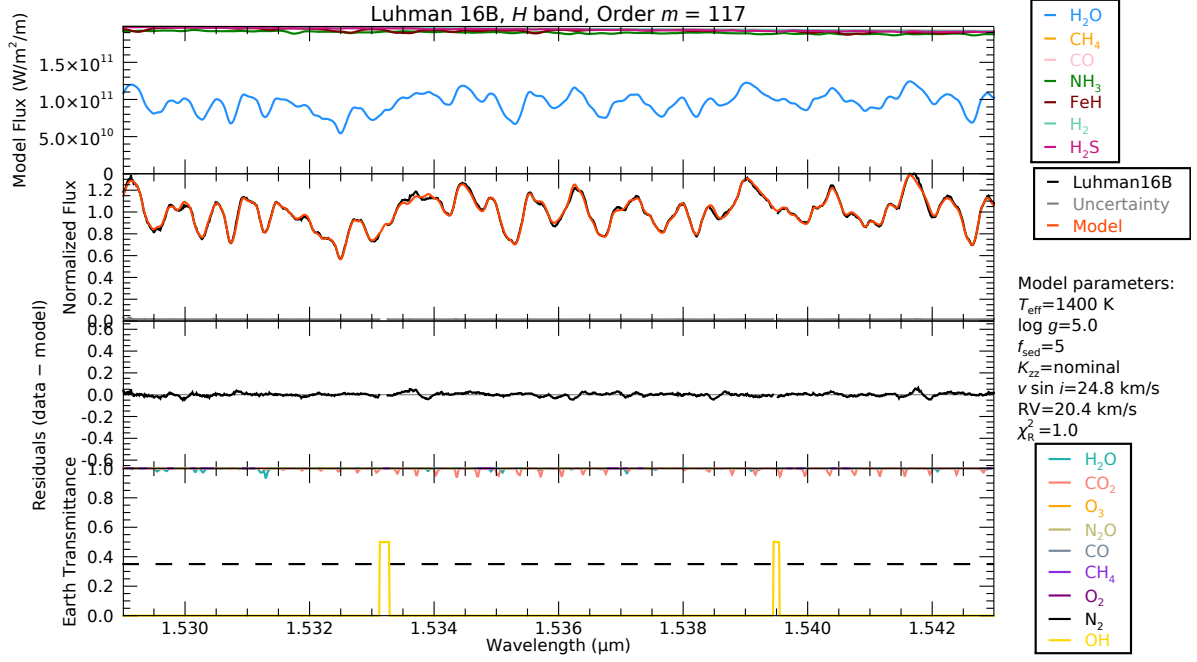


Figure B2. Continued.

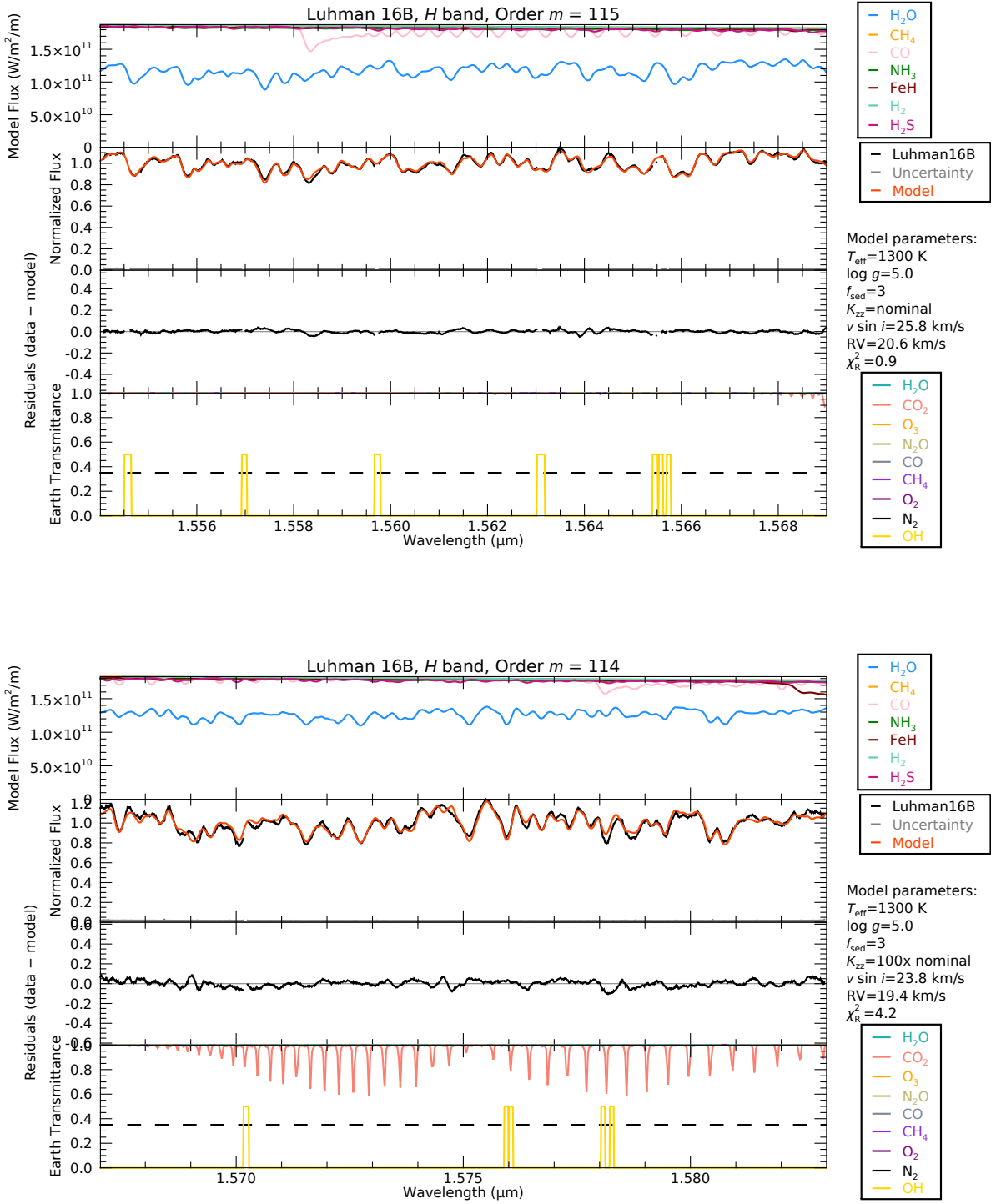


Figure B2. Continued.

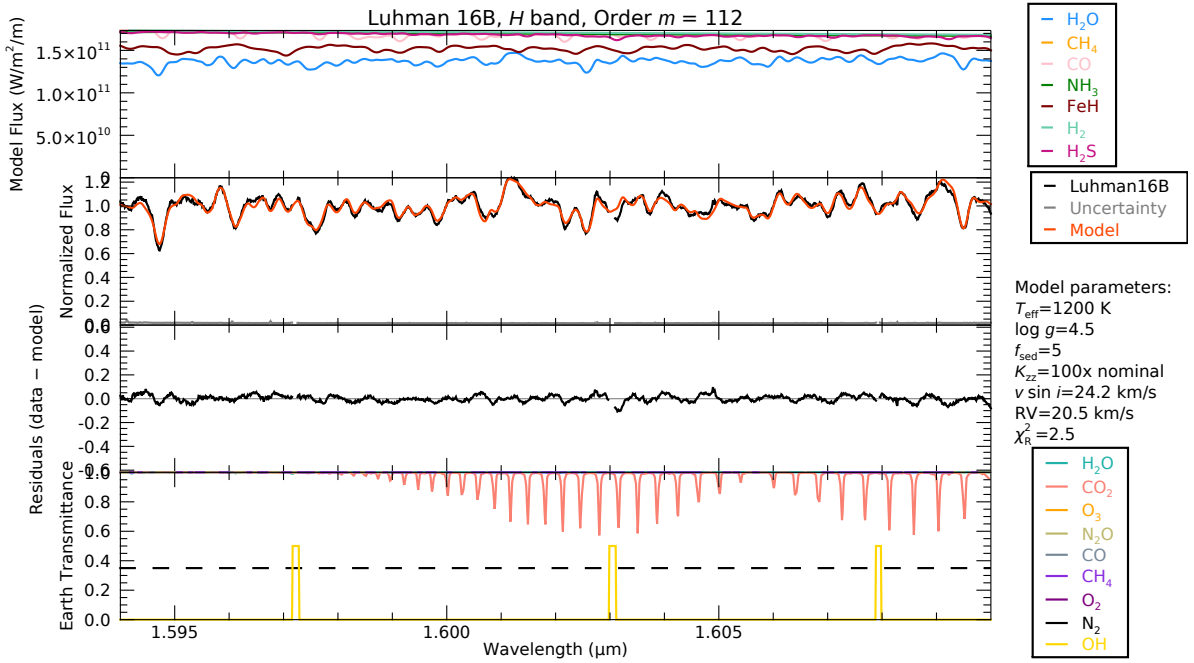
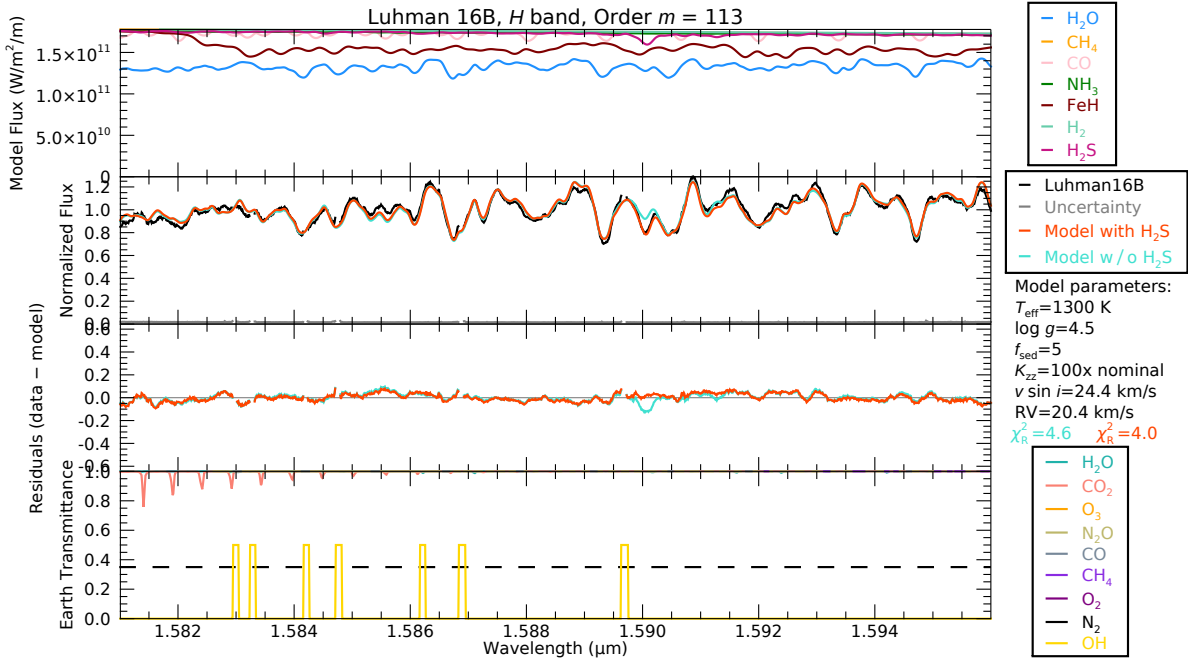


Figure B2. Continued.

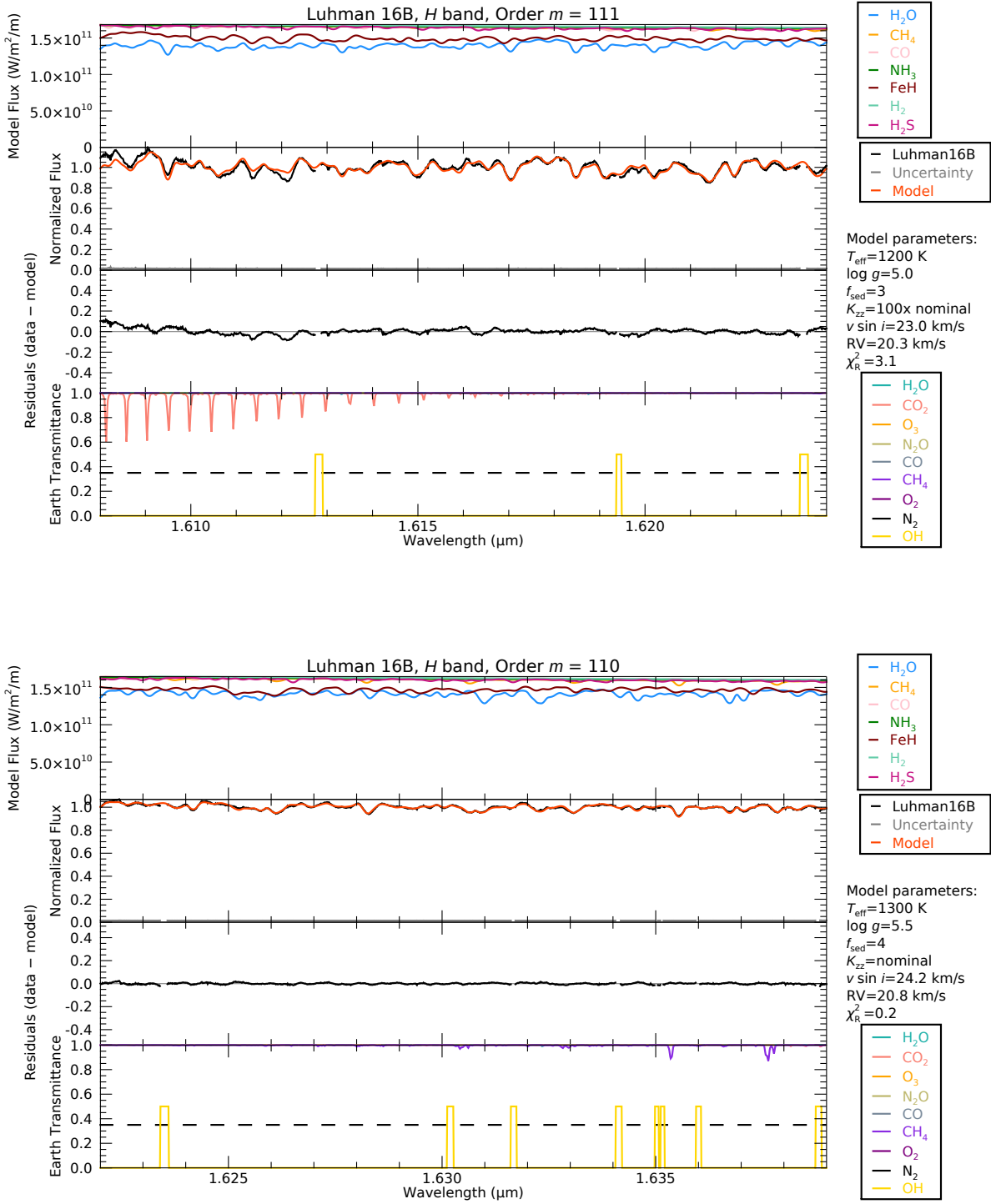


Figure B2. Continued.

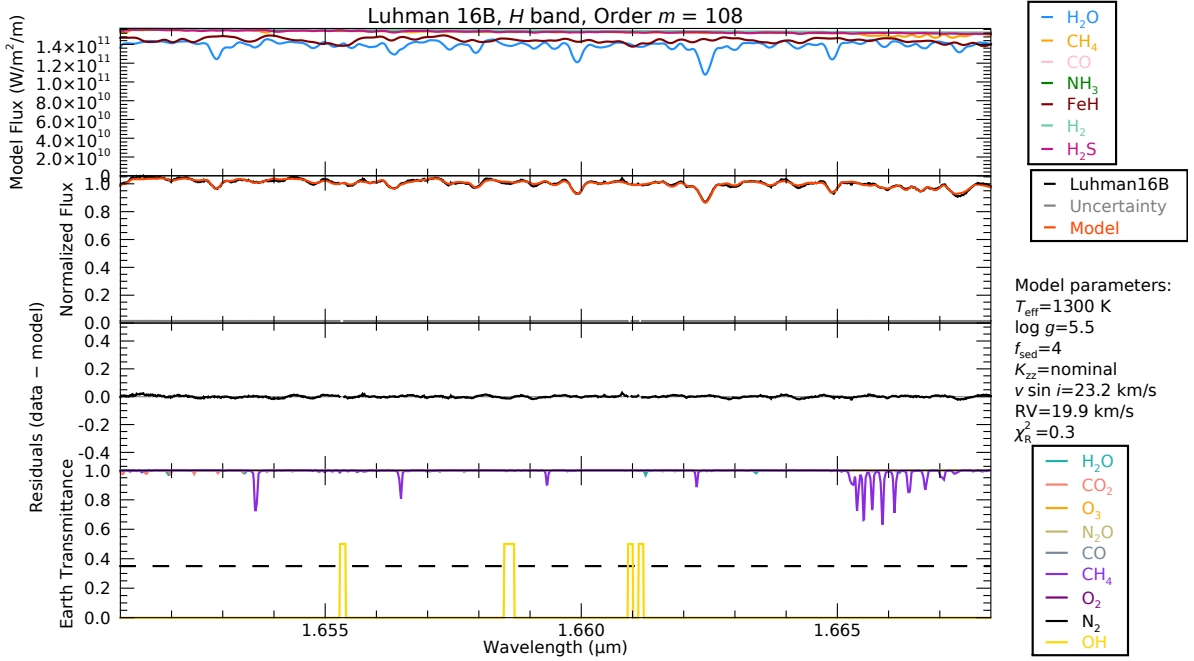
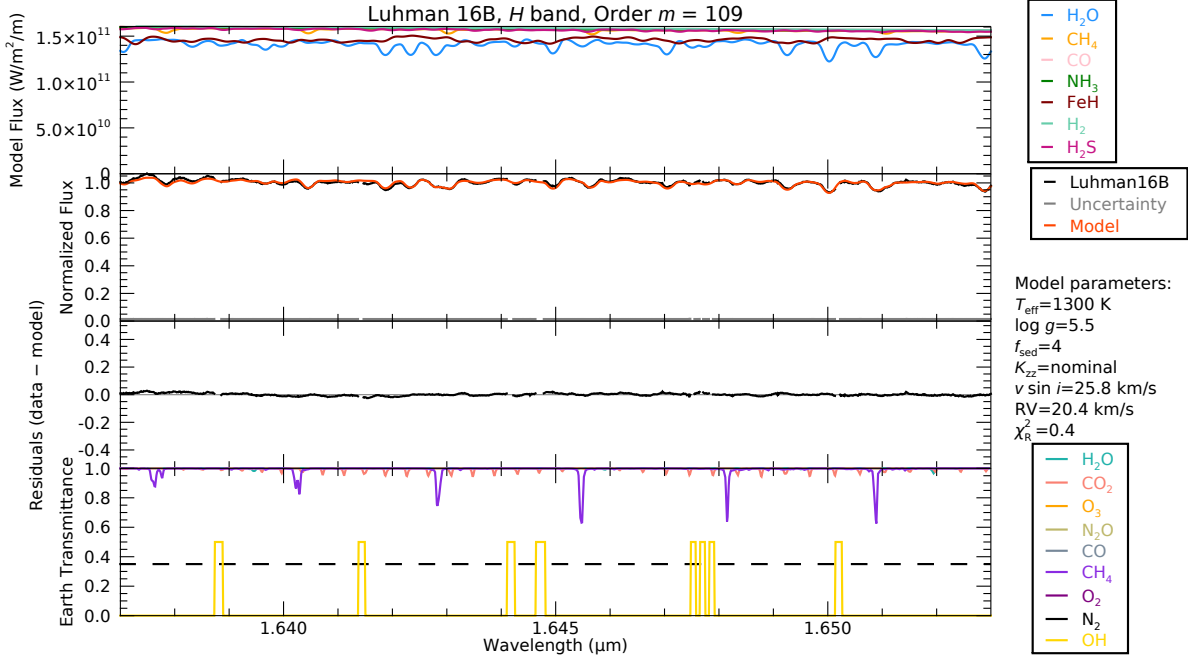


Figure B2. Continued.

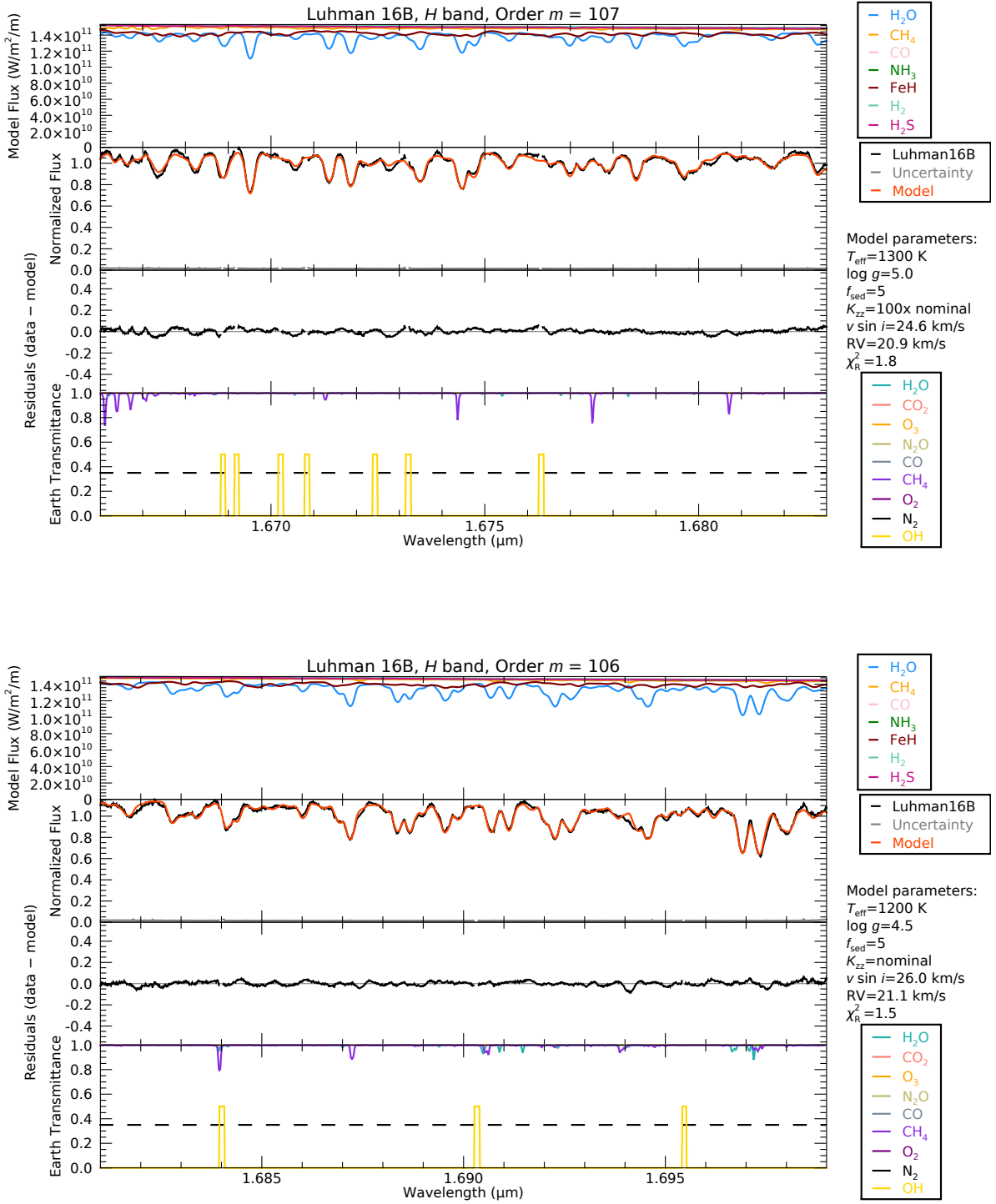


Figure B2. Continued.

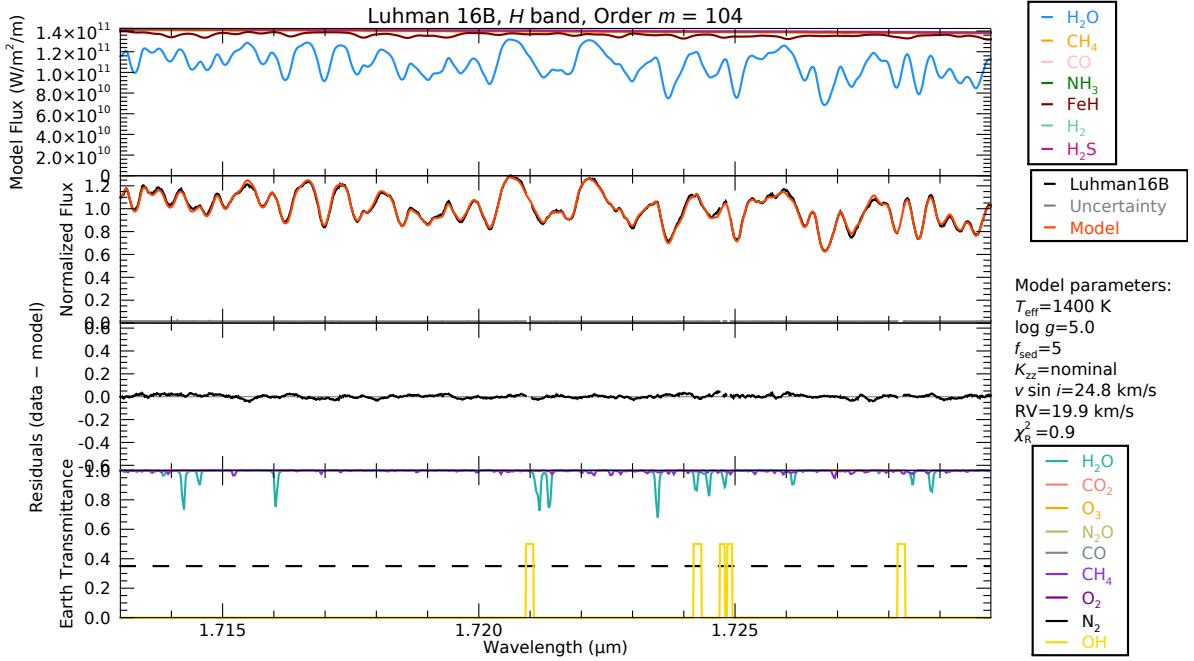
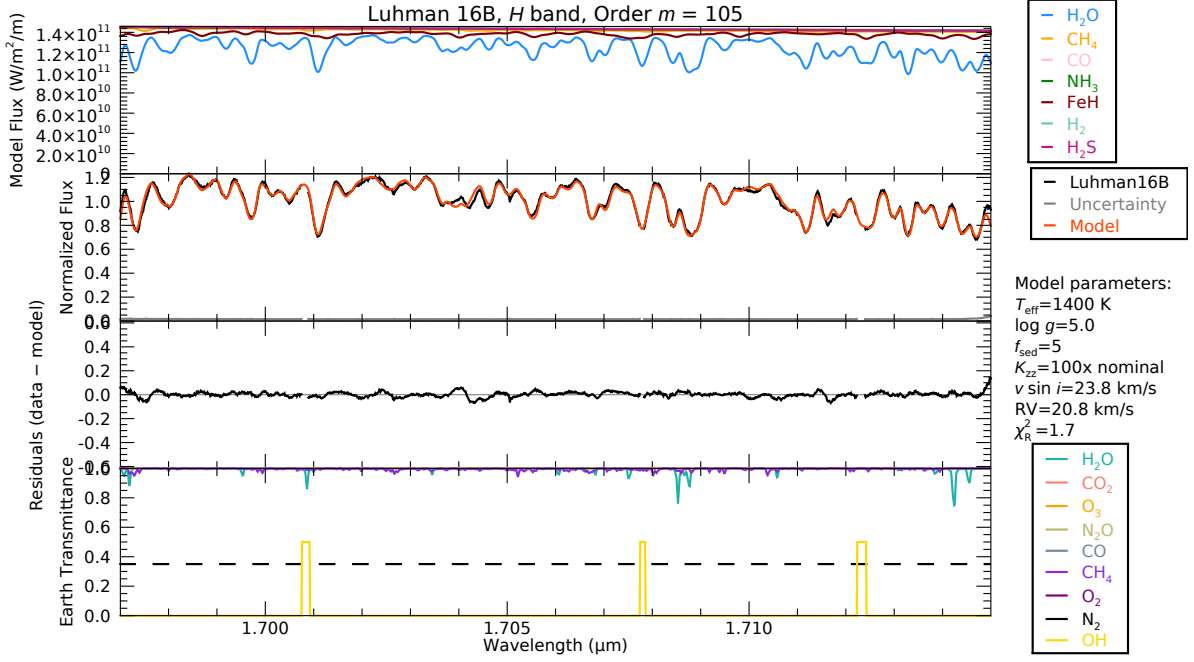


Figure B2. Continued.

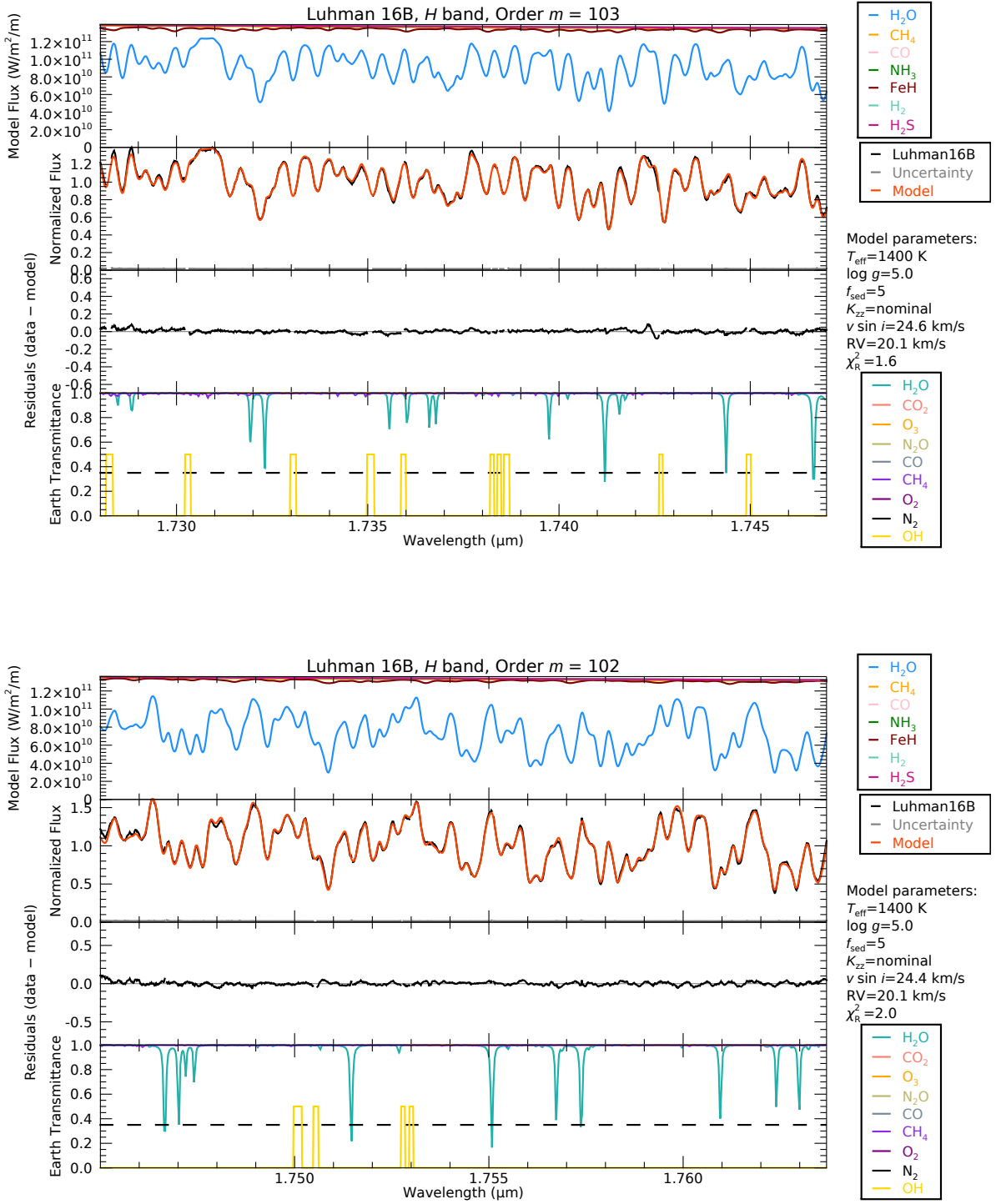


Figure B2. Continued.

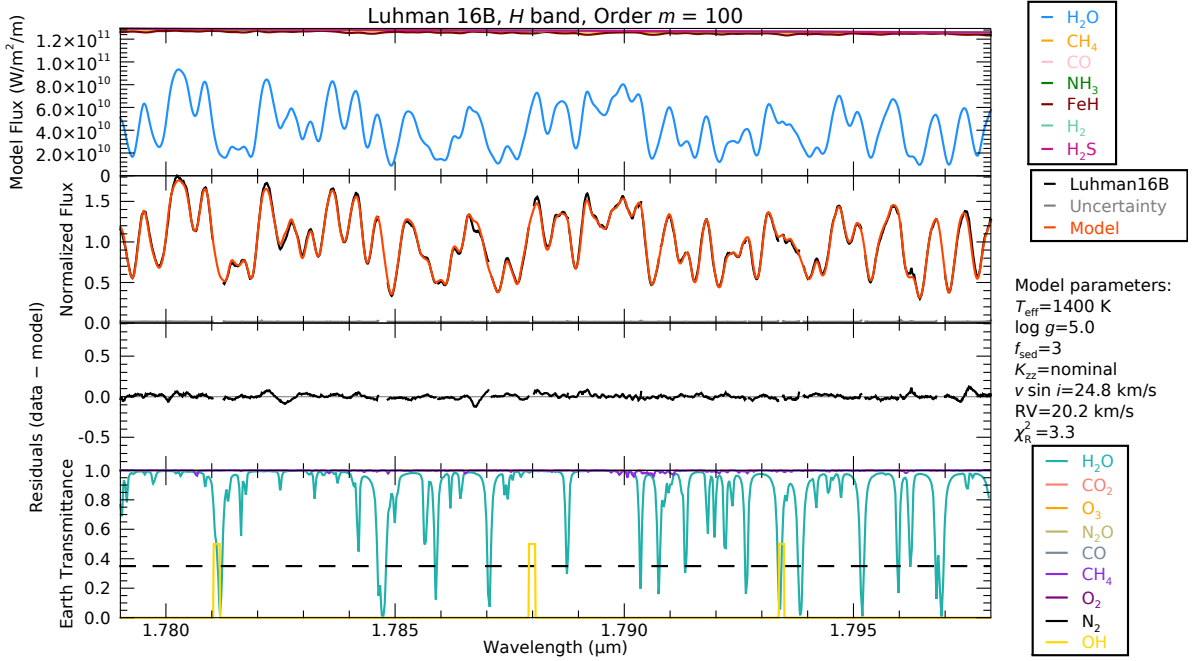
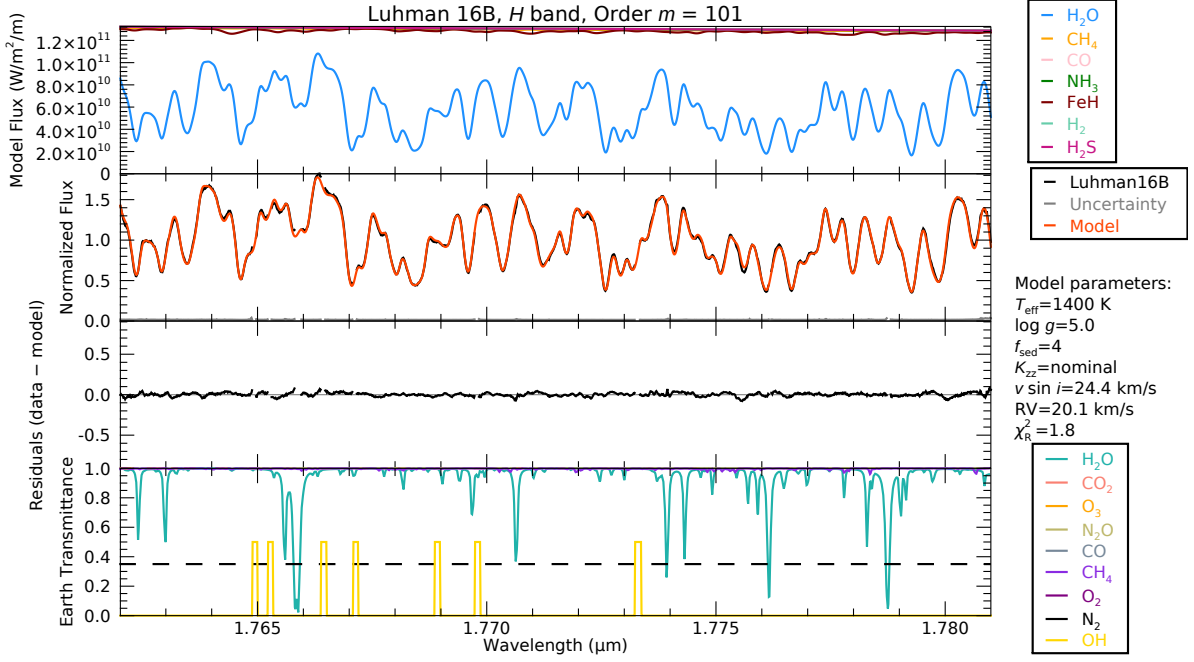


Figure B2. Continued.

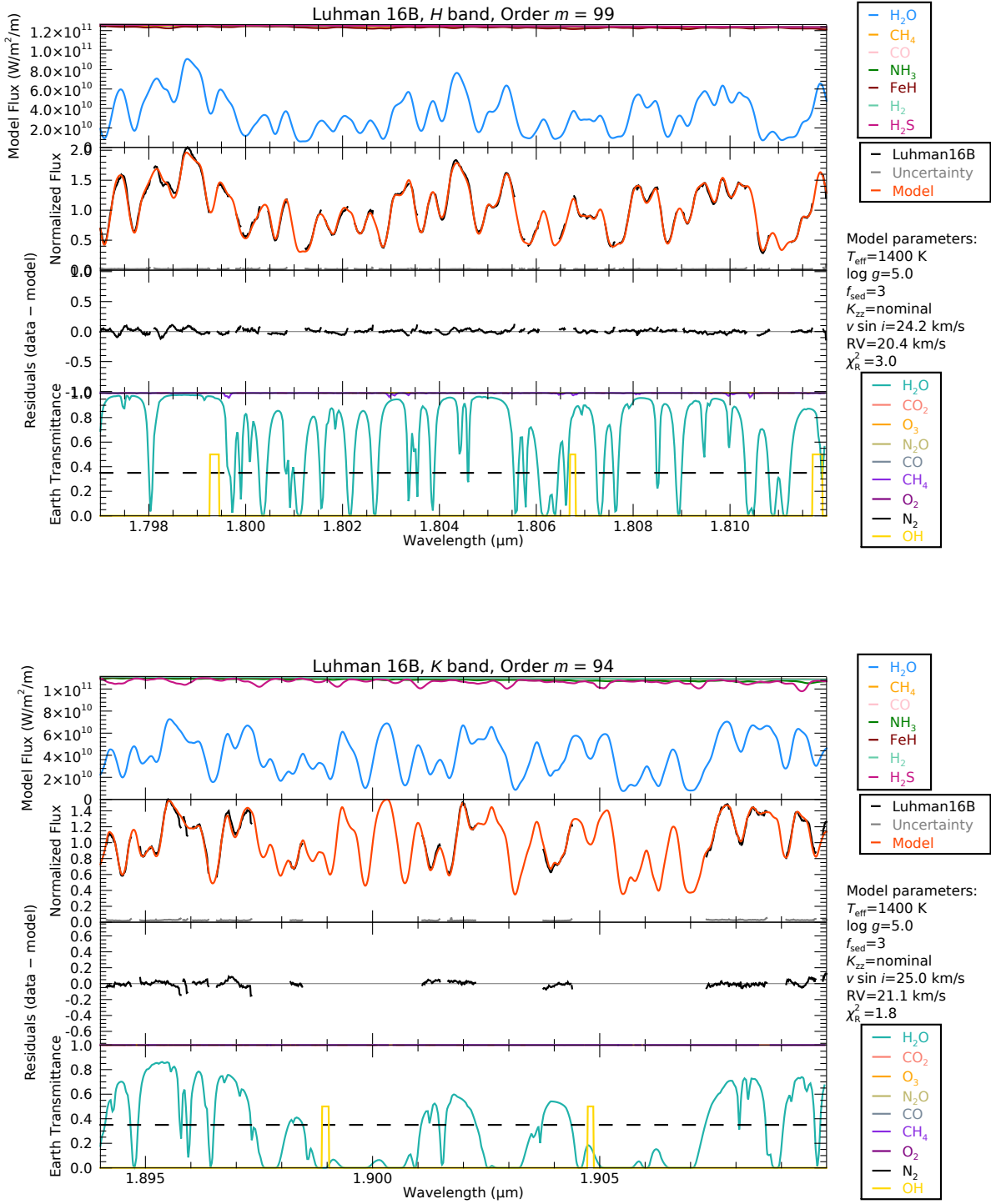


Figure B2. Continued.

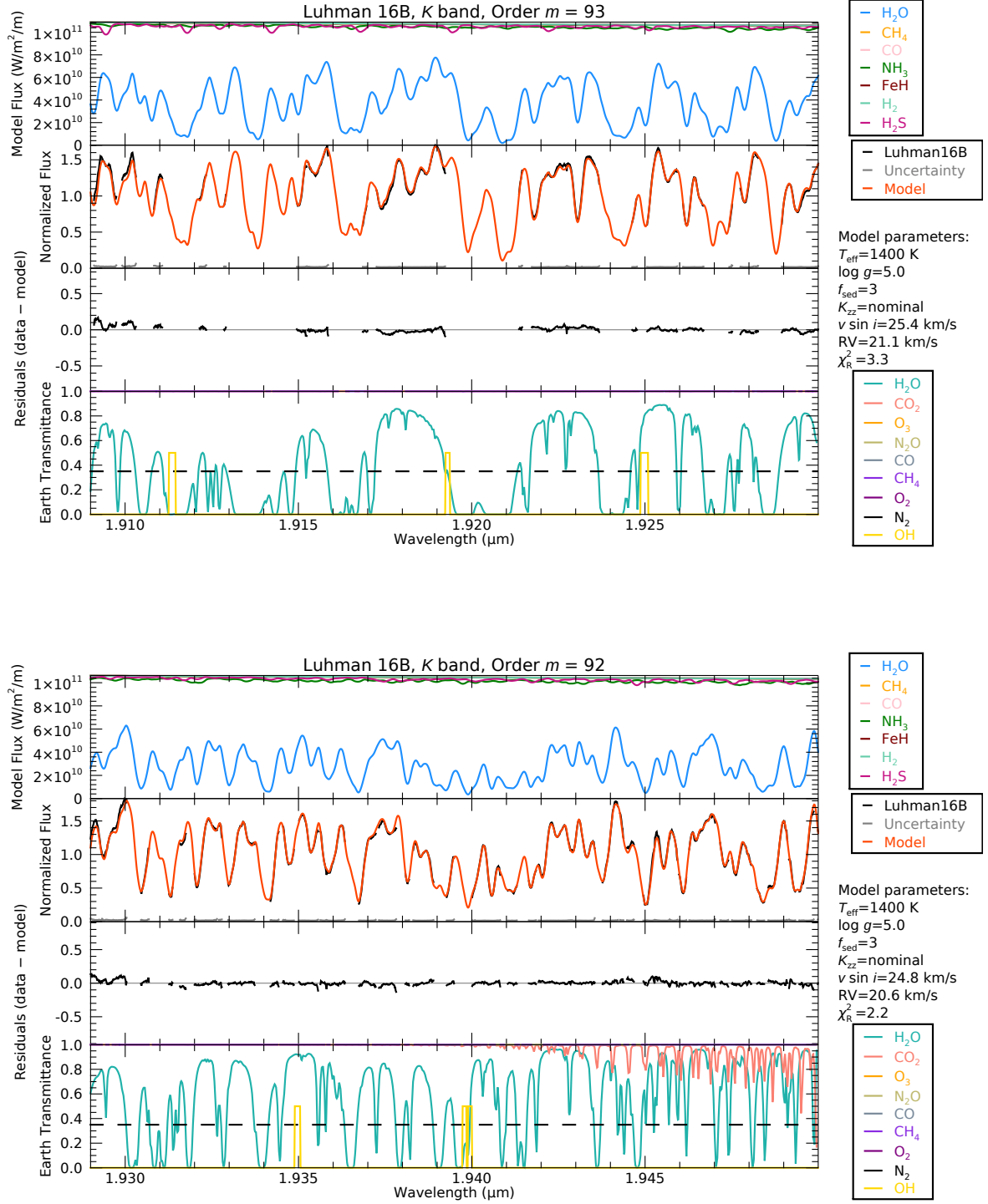


Figure B2. Continued.

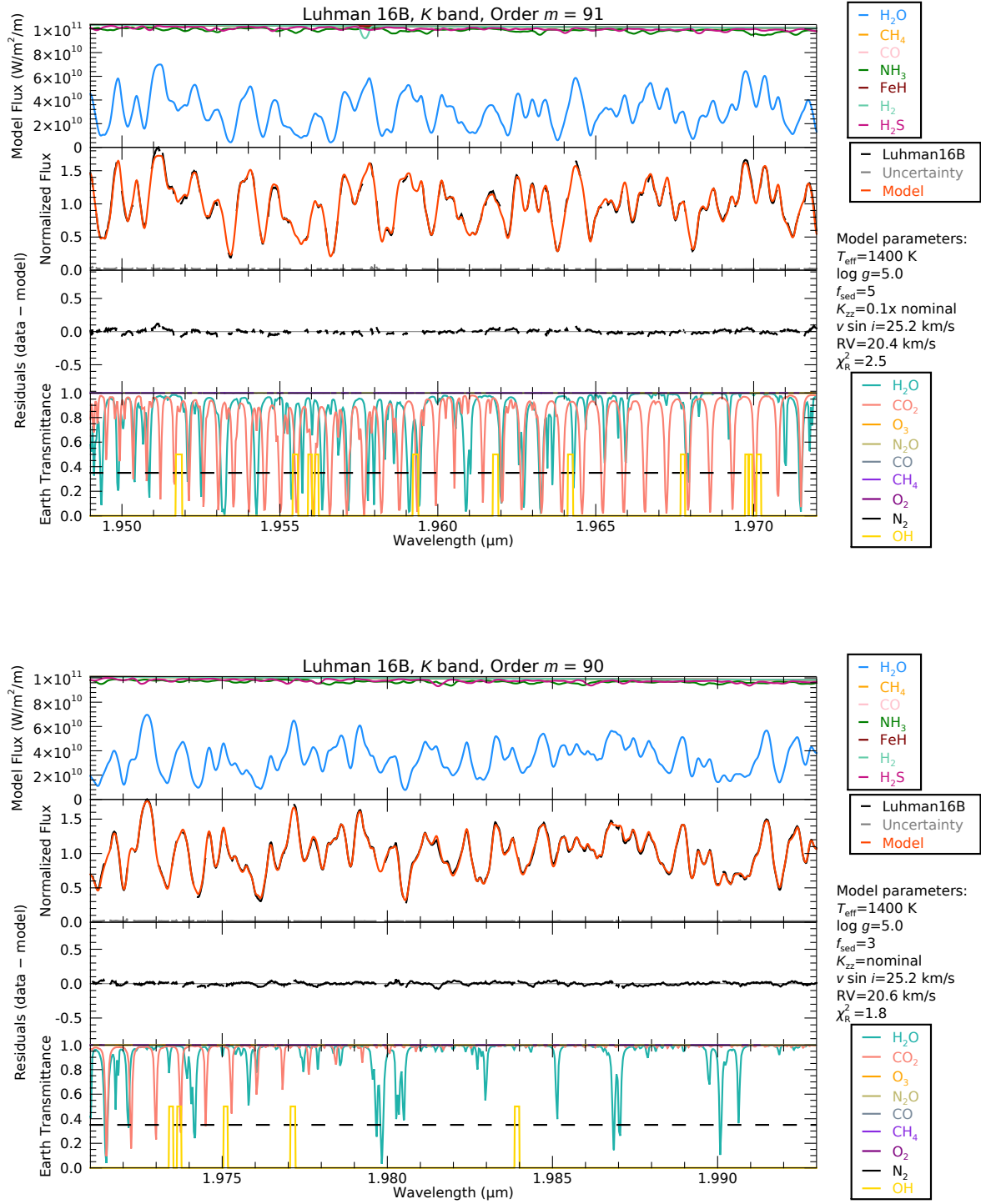


Figure B2. Continued.

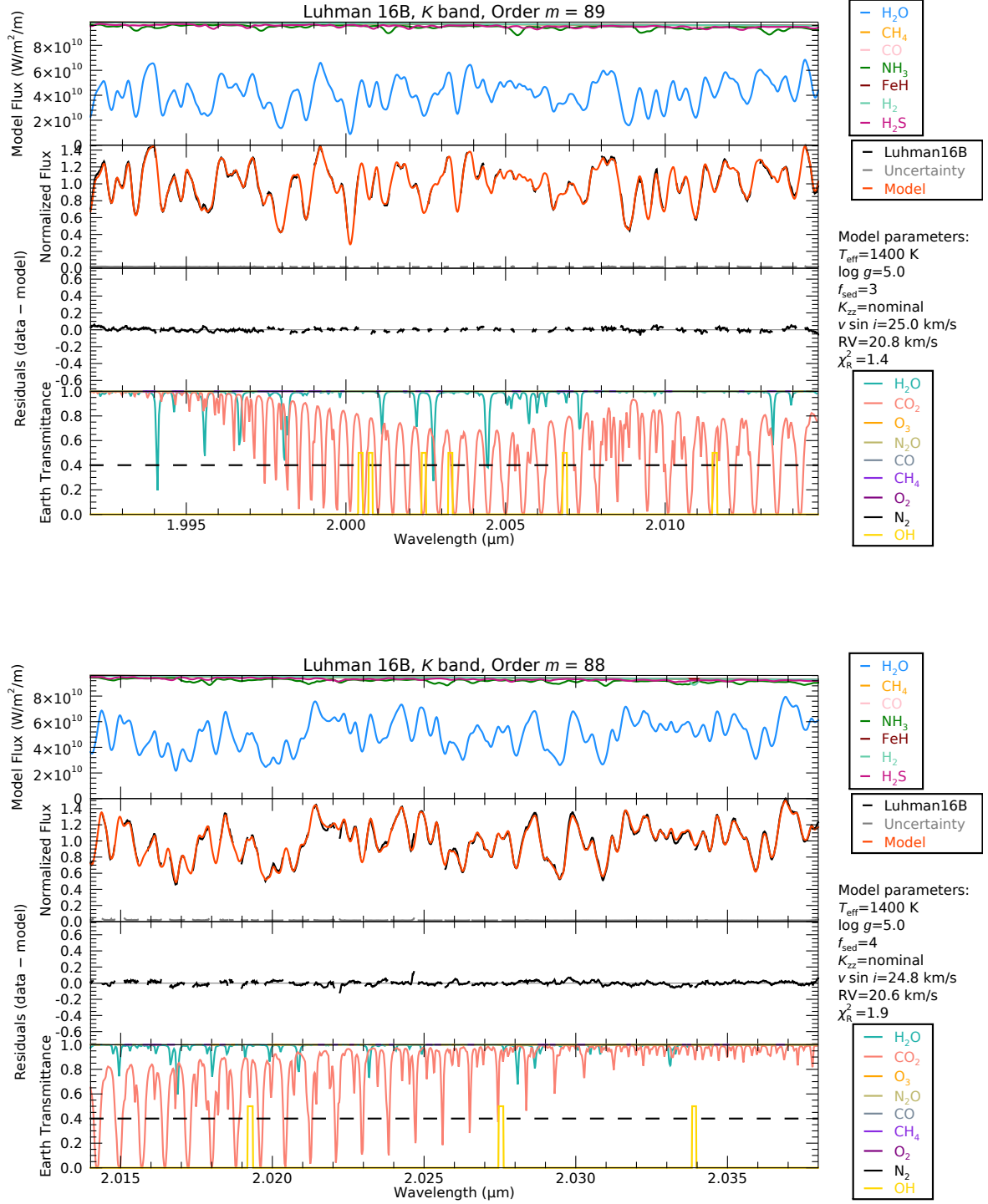


Figure B2. Continued.

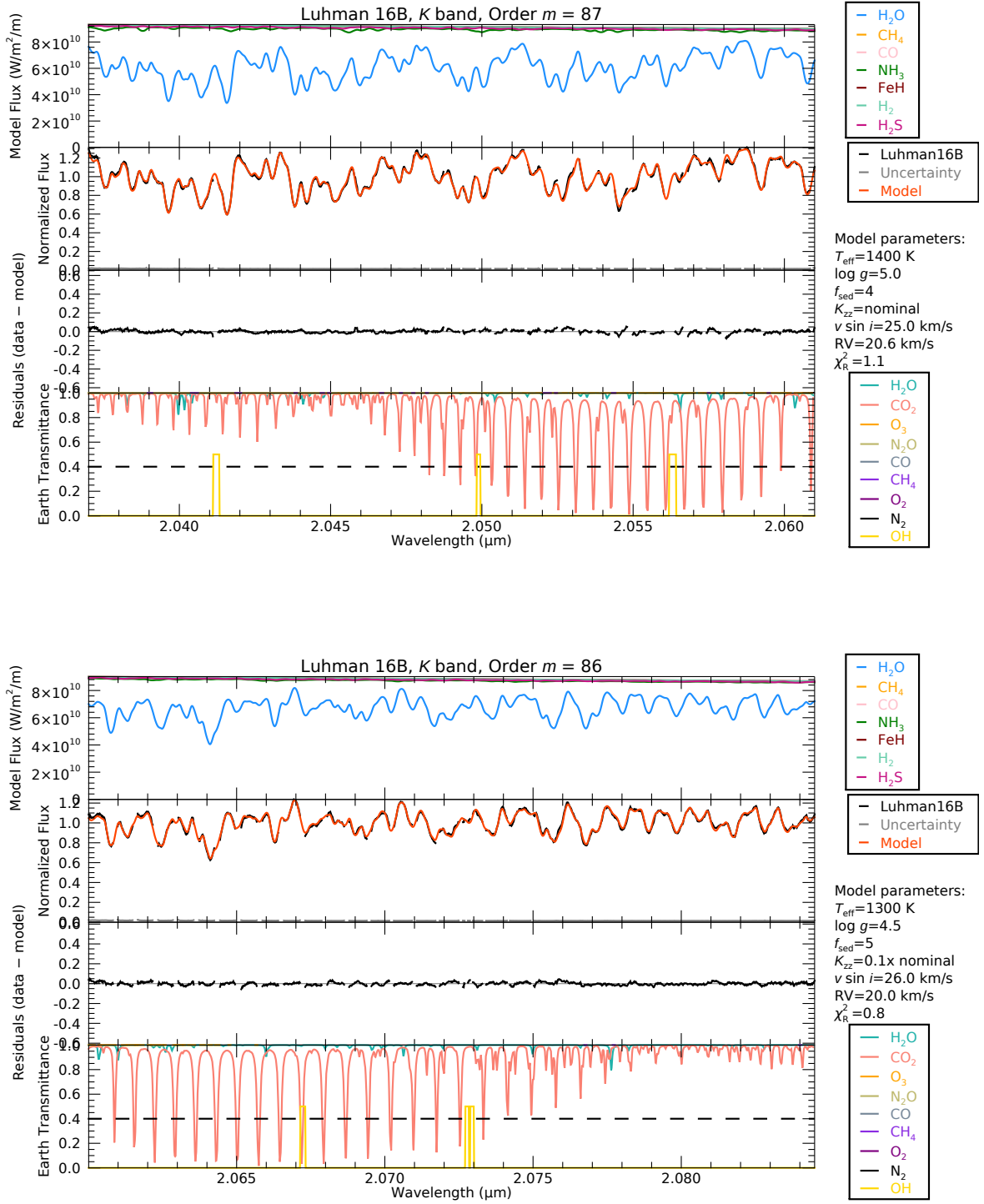


Figure B2. Continued.

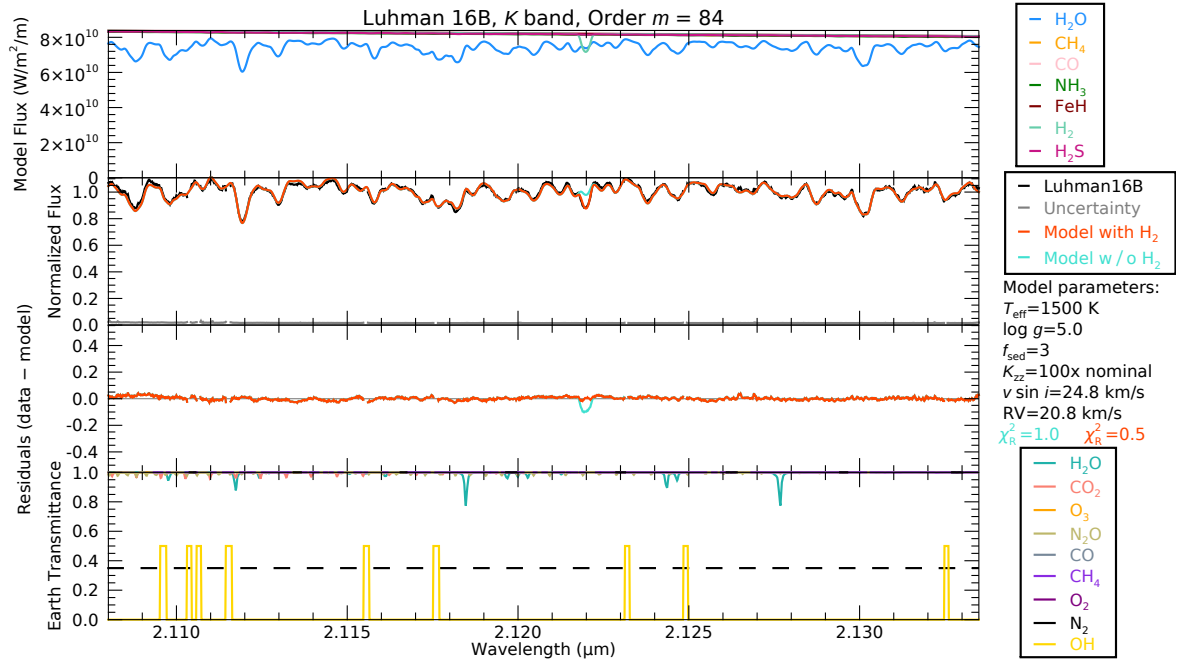
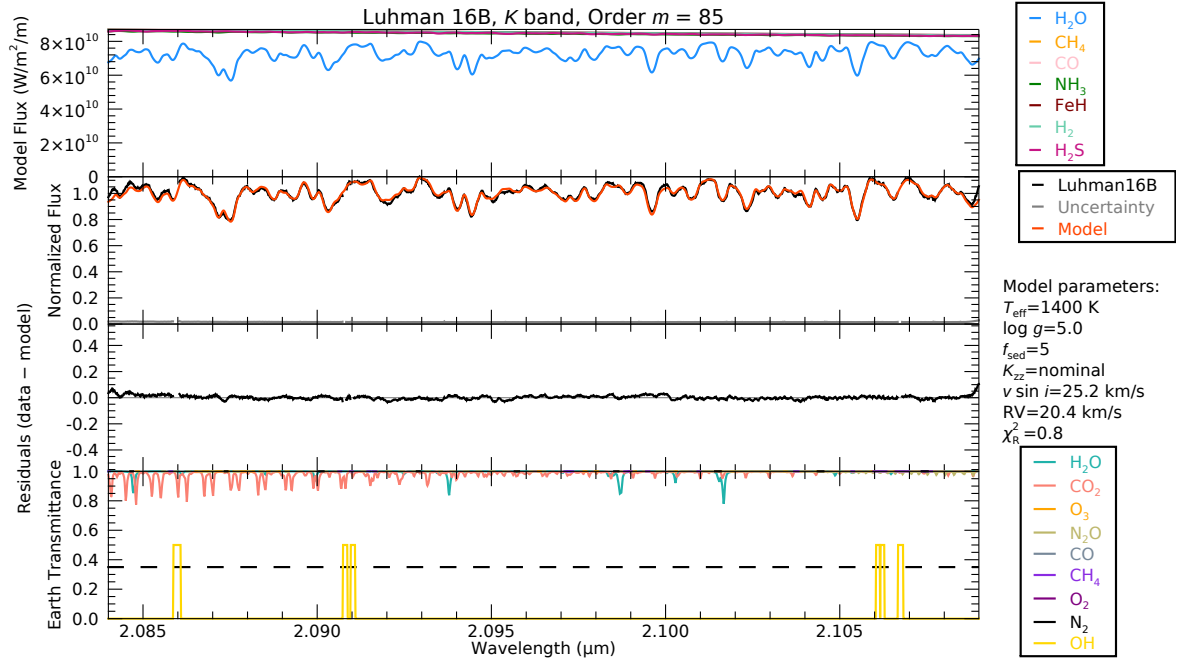


Figure B2. Continued.

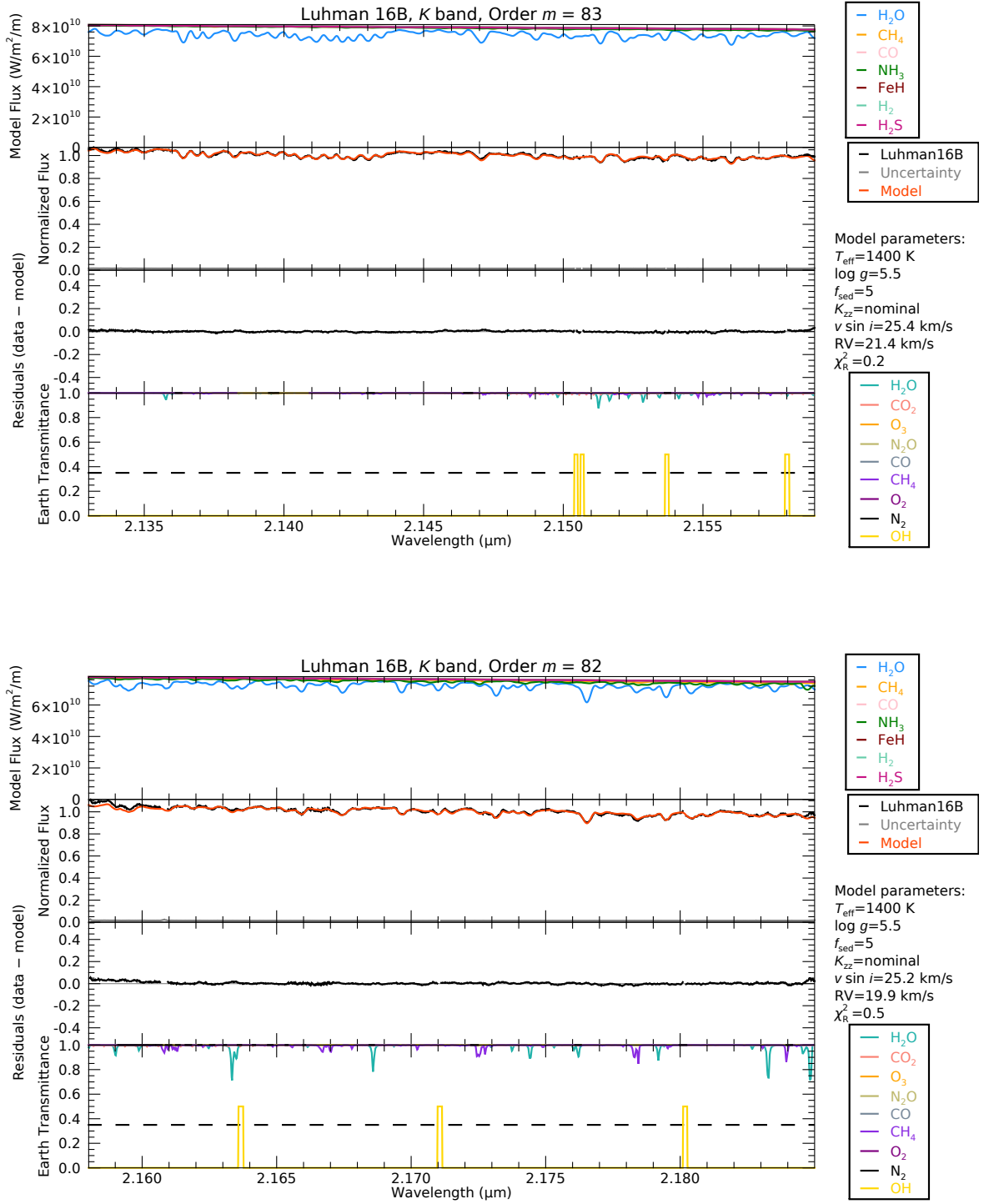


Figure B2. Continued.

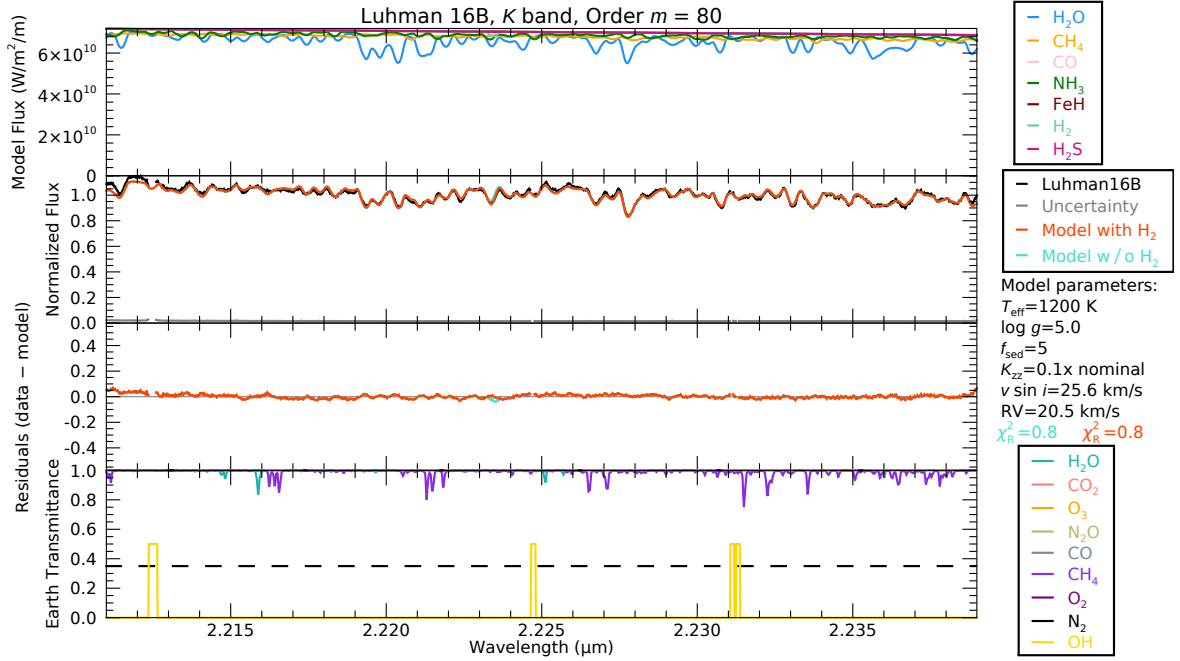
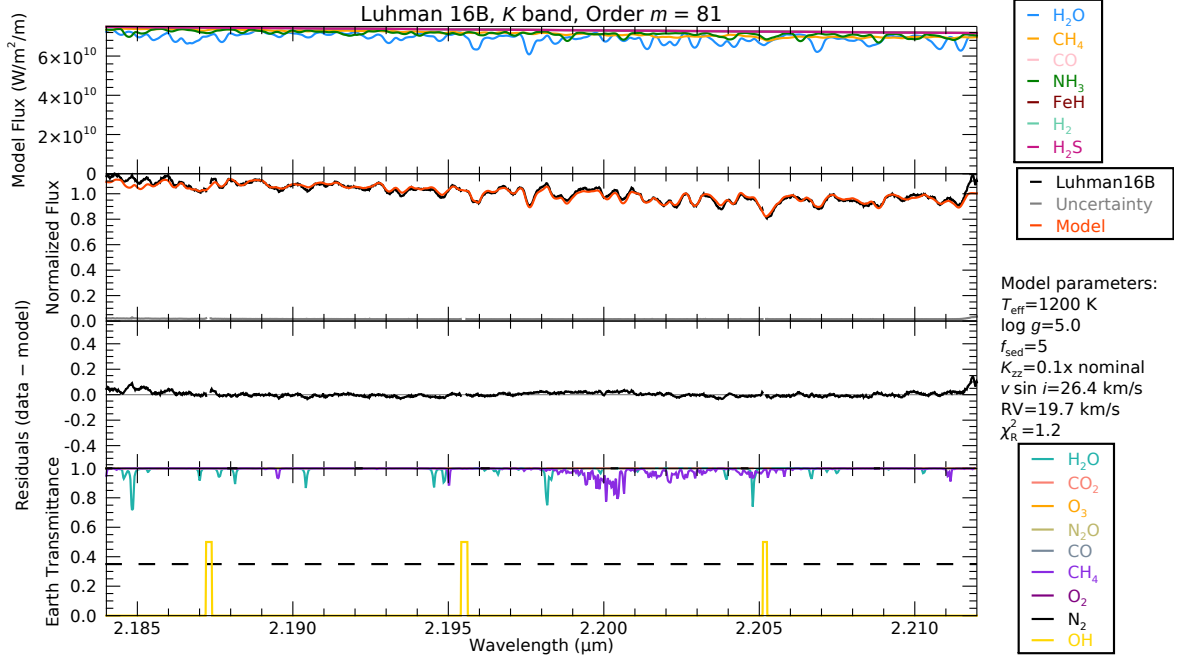


Figure B2. Continued.

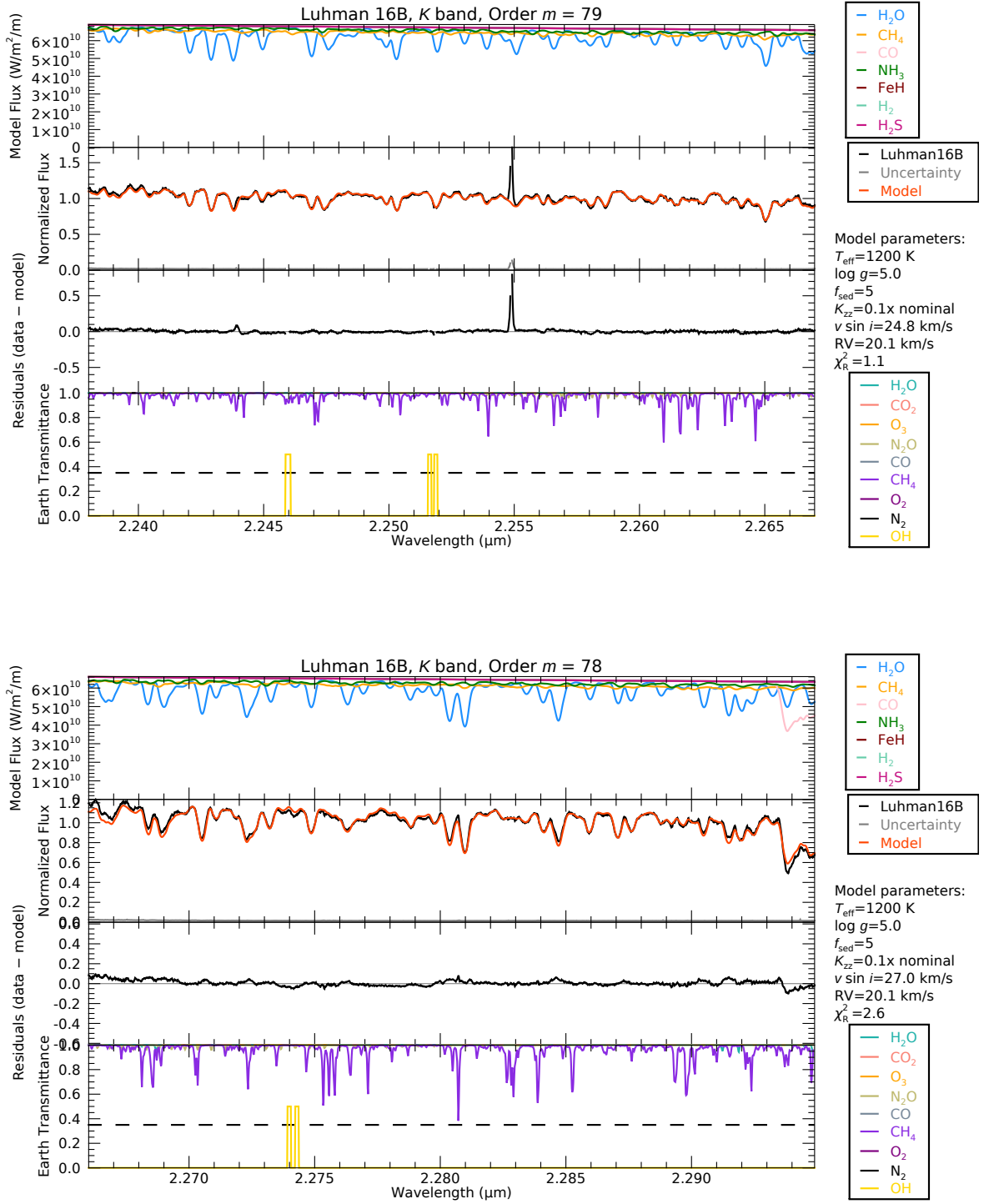


Figure B2. Continued.

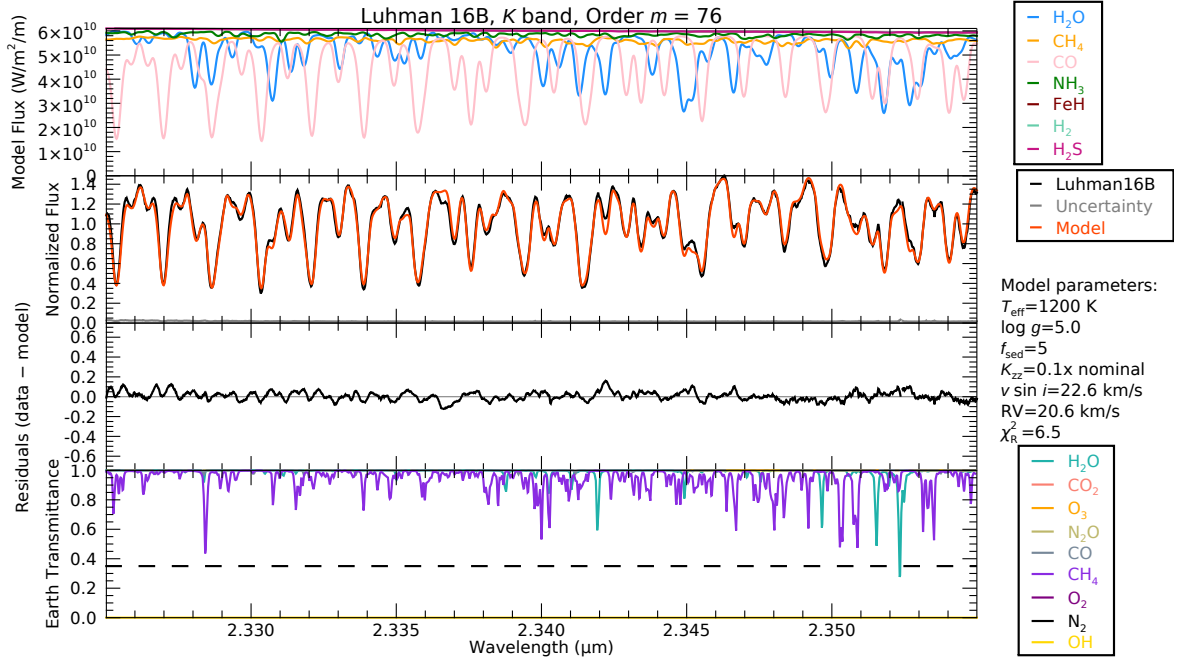
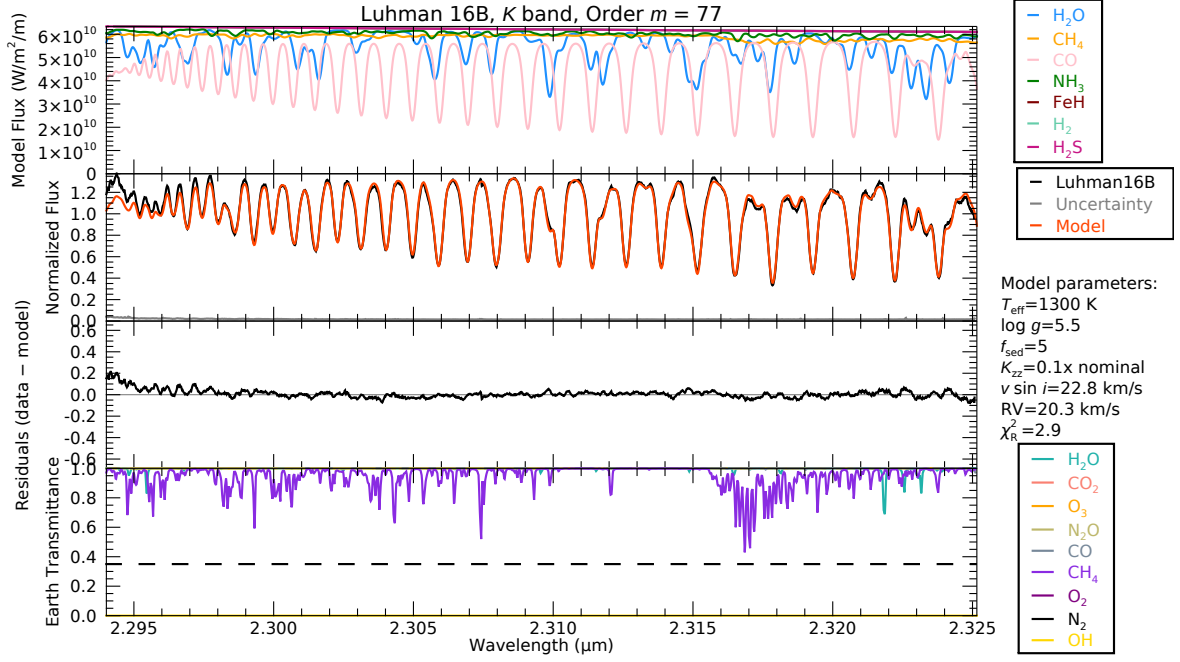


Figure B2. Continued.

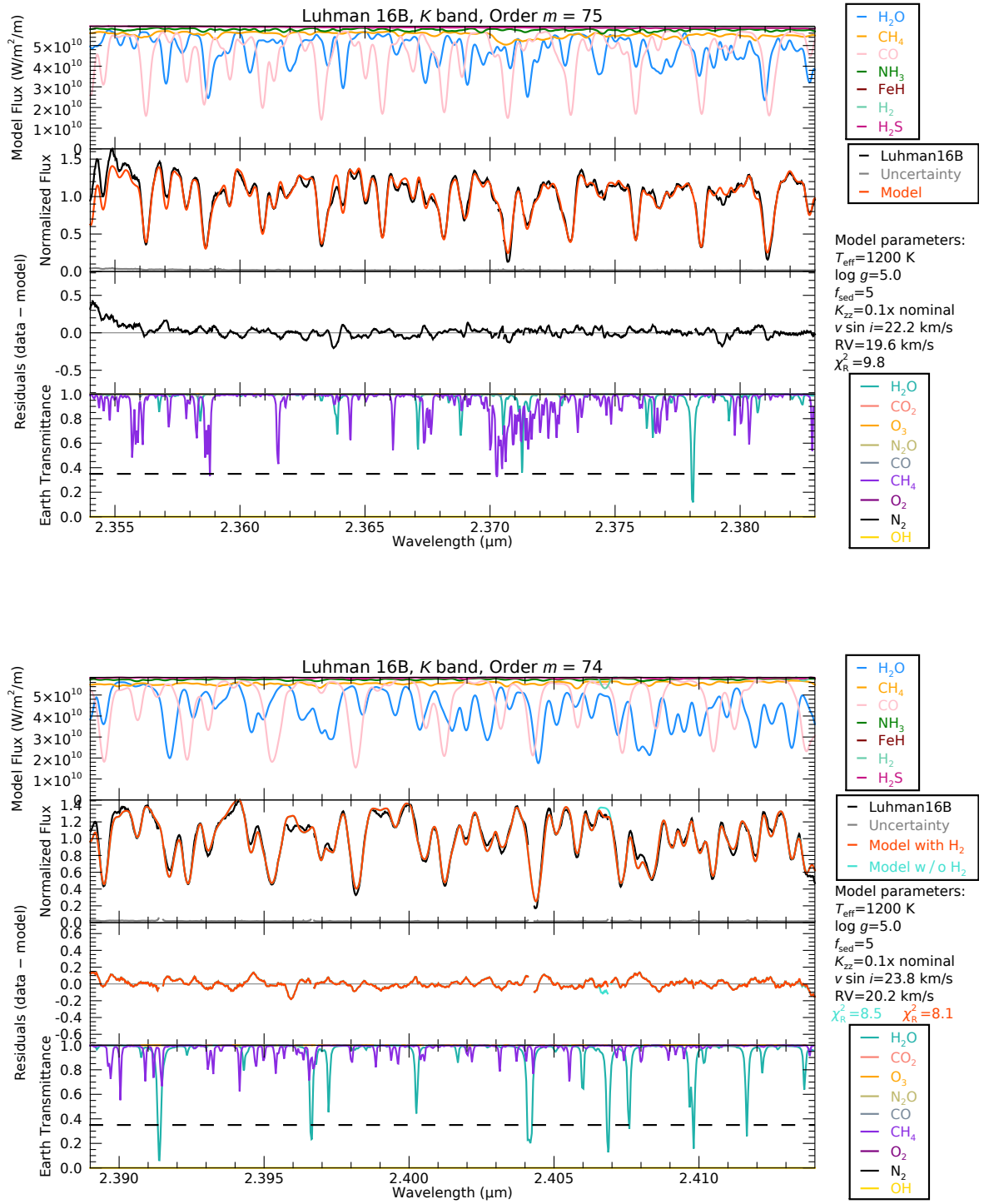


Figure B2. Continued.

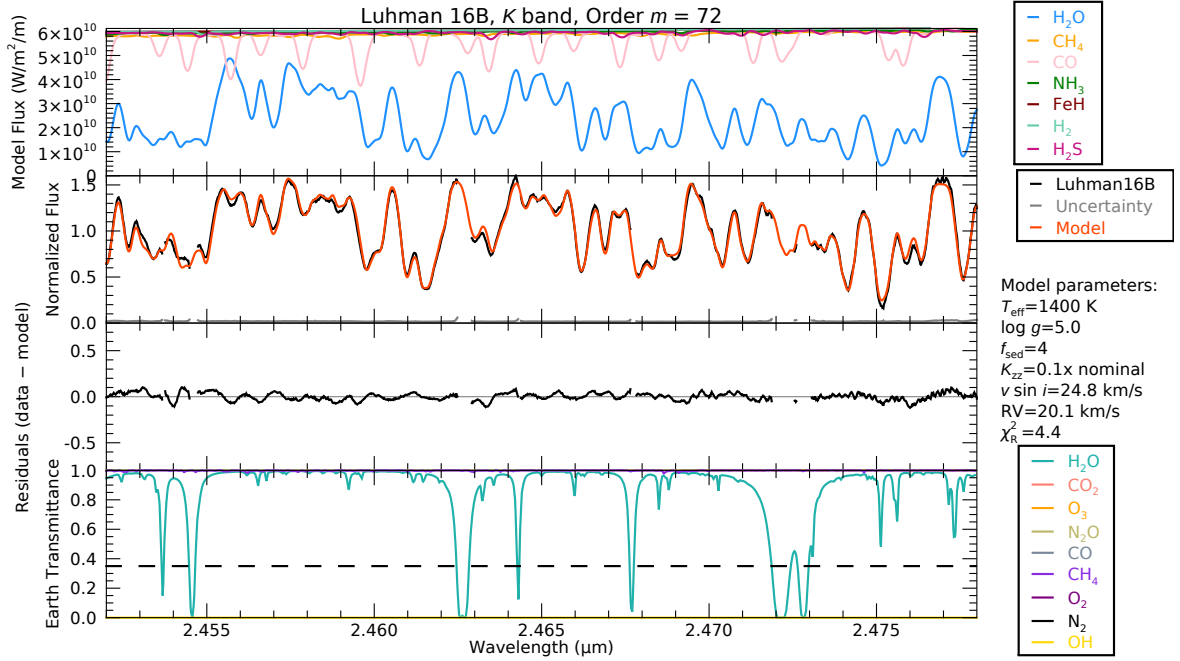
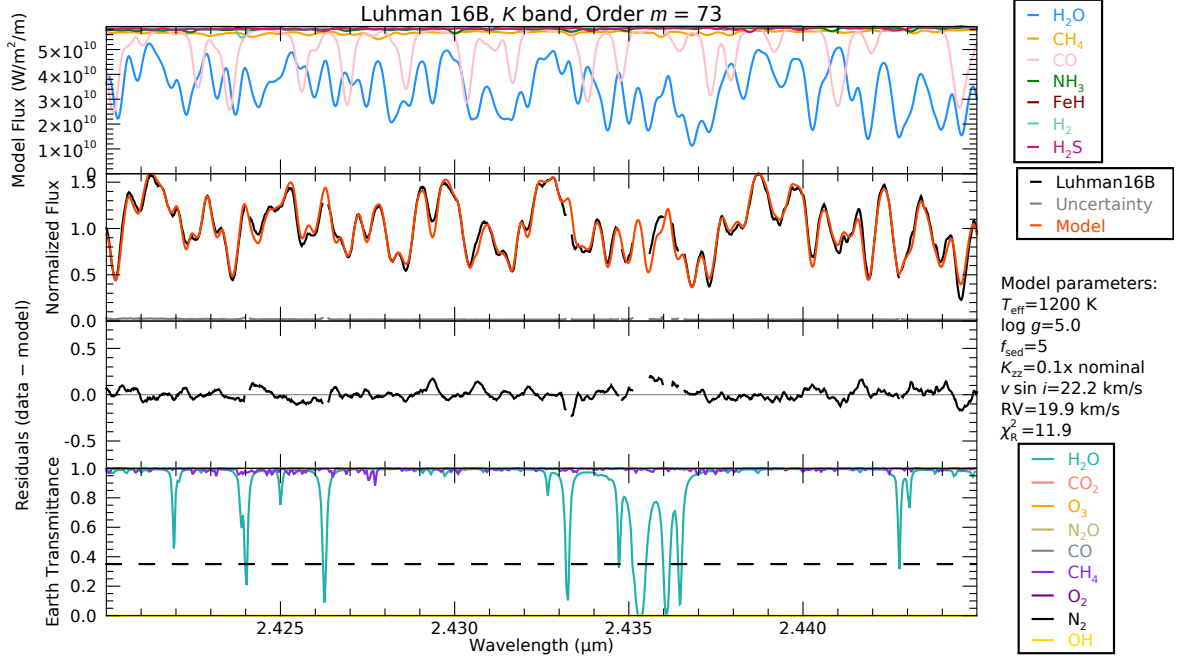


Figure B2. Continued.